



**Dipl.-Ing. Johannes Fröch, BSc**

**Mechanical Properties of Free-Standing 3D  
Nanostructures Fabricated via Focused Electron  
Beam Induced Deposition**

**MASTER'S THESIS**

to achieve the university degree of  
Diplom-Ingenieur  
Master's degree programme: Advanced Materials Science

submitted to

**Graz University of Technology**

Supervisor

Ass.Prof. Priv.-Doz. Dipl.-Ing. Dr. techn. Harald Plank

Institute of Electron Microscopy and Nanoanalysis

Graz, February 2017

## **AFFIDAVIT**

I declare that I have authored this thesis independently, that I have not used other than the declared sources/resources, and that I have explicitly indicated all material which has been quoted either literally or by content from the sources used. The text document uploaded to TUGRAZonline is identical to the present master's thesis.

---

Date

---

Signature

## Abstract

In recent years Focused Electron Beam Induced Deposition (FEBID) has attained increasing attention from different scientific disciplines, as it has left its status of a “scientists playground” and evolved into a reliable additive manufacturing tool for functional nanofabrication. In FEBID, a focused electron beam is utilized to locally dissociate surface adsorbed precursor molecules, leading to permanently remaining, functional deposits according to the electron beam movement. As a unique strength, FEBID not only allows fabrication of planar or bulky high-resolution deposits but also enables fabrication of free standing, true 3D nanostructures with an accuracy and a predictability unmatched by any other technique. Together with its flexibility concerning the applied materials, 3D FEBID can be understood as a generic technology for the fabrication of morphological, electrical, magnetical, or mechanical nanostructures for a diverse range of applications. In a collaboration with the company GETec Microscopy, the current focus lies on the application of 3D structures as thermal nanoprobos. In more detail, we anticipate the fabrication of a freestanding Pt(-C) nano-bridge, placed on two electrodes on a pre-structured AFM cantilever. If such a structure gets in contact with a heated sample surface, the electric resistance changes which can be read out via voltage measurements. The main advantage lies in the small dimensions of the 3D architecture which should allow for fast response times (small volume) together with high lateral resolution as the tip radius can go down to about 5 nm, an improvement factor of about 5 compared to currently available thermal probes. However, such measurements strongly rely on the contact force of the tip, which could lead to compression, deformation or destruction of the small nano-architectures. Therefore, an initial step has to be done in order to understand the relationships between design and spatial stiffness which then can be used for optimization towards most stable architectures for final application as thermal nanoprobos. Following this motivation this thesis uses a combined approach between Finite Element Simulations, Scanning Electron Microscopy and *in-situ* Force Spectroscopy Measurements for a comprehensive insight in the mechanical properties of 3D nano-architectures. The thesis not only revealed the ideal geometries concerning its design and overall dimensions but also led to the identification of two unexpected effects, lateral twisting, and a non-linear behavior during axial compression. Related simulations could reveal its origin leading to the definition of design rules to prevent these unwanted effects. All results together finally led to first real applications of optimized 3D architectures as AFM tips shown in the last part of this study. By that, this thesis not only spans the bow from fundamental behavior towards the first proof-of-principle but also lays the foundation for further studies towards the main goal of FEBID based, 3D nanoprobos for thermal characterization at the nanoscale with yet unknown possibilities.

## Kurzfassung

Aufgrund ihrer Entwicklung in den letzten Jahren hat die Fokussierte Elektronenstrahlabscheidung (FEBID) zunehmend an Aufmerksamkeit von verschiedensten wissenschaftlichen Disziplinen erhalten, wobei sich diese Technik vom Status einer „wissenschaftlichen Spielwiese“ hin zu einem verlässlichen additiven Herstellungsverfahren innerhalb des Gebietes der funktionellen Nanofabrikation etabliert hat. Bei FEBID wird ein fokussierter Elektronenstrahl dazu verwendet um lokal Präkursormoleküle, welche auf der Oberfläche adsorbiert sind so aufzuspalten, dass abhängig von der Bewegung des Elektronenstrahls ein funktionales Deponat permanent auf der Oberfläche entsteht. Als besondere Stärke dieser Technik erlaubt FEBID nicht nur die Fabrikation von ebenen oder massiven hochdefinierten Abscheidungen sondern ermöglicht es auch freistehende 3D Nanostrukturen mit einer Genauigkeit und Vorhersagbarkeit zu bauen, die mit keiner anderen Technik erreicht wird. Zusammen mit der Flexibilität aufgrund einer breiten Auswahl an Präkursormaterialien kann 3D FEBID als eine generische Technik zur Fabrikation von morphologischen, elektrischen, magnetischen oder mechanischen Nanostrukturen für diverse Anwendungsmöglichkeiten gesehen werden. In Kollaboration mit der Firma GETec Microscopy, liegt der Fokus momentan auf die Anwendung von 3D Strukturen als thermische Nanosonden. Im Detail, ist die Fabrikation von freistehenden Pt(-C) Nano-Brücke geplant, welche auf zwei Elektroden eines vorstrukturierten AFM Kantilevers platziert wird. Im Falle eines Kontakts mit einer geheizten Probenoberfläche ändert sich der elektrische Widerstand entlang dieser Struktur, was wiederum mittels einer Spannungsmessung ausgelesen werden kann. Der größte Vorteil liegt hier bei den reduzierten Dimensionen der 3D Architektur welche sehr schnelle Einstellzeiten erlauben sollten (kleines Volumen) kombiniert mit einem hohen Auflösungsvermögen der Nanosonde, aufgrund deren Radius an der Spitze mit bis zu 5 nm, das entspricht einer Verbesserung zu herkömmlich verwendeten Methoden um einen Faktor 5. Jedoch treten bei solchen Messungen hohe Anpressdrücke an der Spitze auf, was zu Kompression, Deformation oder Zerstörung der Nanoarchitekturen führt. Deshalb muss vorab der Zusammenhang zwischen Design und Steifigkeit geklärt und verstanden werden wodurch im nächsten Schritt die Optimierung hin zu den steifsten Strukturen gefunden werden kann bis schließlich hin zur Anwendung solcher Strukturen als thermische Nanosonden. In diesem Sinne wird in dieser Diplomarbeit ein kombinierter Ansatz aus Finite Elemente Simulationen, Rasterelektronenmikroskopie zusammen mit *in-situ* Kraftspektroskopie verwendet um einen umfassenden Einblick in die mechanischen Eigenschaften von 3D Nanoarchitekturen zu erhalten. Dabei wurden nicht nur die idealen Geometrien in Hinblick auf Design und Dimensionen gefunden, sondern auch zwei unerwartete Effekte enthüllt, nämlich eine laterale Schraubbewegung und eine nicht-linearität bei axialer Kompression. Mittels vergleichbaren Simulationen konnten die genauen Grundursachen verifiziert und in weiterer Folge diverse Designregeln definiert werden, die ebendiese ungewollten Effekte verhindern. Schließlich konnten die gesammelten Erkenntnisse dahingehend verwendet werden indem eine optimierte 3D Struktur auf einem Kantilever gebaut wurde. Dadurch spannt diese Diplomarbeit nicht nur den Bogen von einem fundamentalen Verständnis hin zu einem ersten Proof-of-Principle, sondern legt auch das Fundament für weiterführende Untersuchungen mit dem Ziel FEBID basierte 3D Nanosonden für die thermische Charakterisierung in der Nanoskala zu realisieren, welche ungeahnte Möglichkeiten darbieten.

## Acknowledgements

At first, I would like to thank Prof. Ferdinand Hofer, head of the institute, for giving me the chance to do my master thesis at the Institute for Electron Microscopy and Nanoanalysis and the support I got from him.

My deepest gratitude goes to my supervisor Ass.Prof. Harald Plank. His enthusiasm and the motivation I got from him kept me going and inspired me to dig deeper in certain effects and investigations than necessary. As well I am thankful for all the things I have learned during the last few years from him in scientific and interpersonal ways, which I will hopefully never forget. Therefore, I am happy that I got the chance to work in his group and to have the freedom to explore my own ideas, while still being directed by such a great mind.

As well, my appreciation goes to his whole work group, S<sup>3</sup>, Sebastian Rauch, Robert Winkler, Jürgen Sattelkow, Ulrich Haselmann, and Ulrich Radeschnig. All of them supported and helped me during my time at the institute and therefore I am more than just grateful to them.

In particular, I want to thank Robert Winkler for his discussions regarding 3D fabrication of free-standing structures and the input and advice I got from him. Furthermore, I want to point out Jürgen Sattelkows contribution to this work, who carried out the AFM measurements at the end of this thesis to proof the imaging capability.

I was happy to do my work in a nice and comfortable environment with my office colleagues, whom I wish all the best in the future and hope their dreams come true. This accounts as well for all FELMI staff members who always were helpful and gave me advice when I needed it.

My gratitude goes to all my friends who stood beside me and I want to thank every one of them for all the good memories I made and for the bad times I could rely on them during the last few years in Graz and I hope to stay in contact with all of them. I will miss all of them.

Finally, I thank my family, the persons who had the biggest influence on me and who have known me the longest - my parents, Luise and Wolfgang, my brother Christopher, and my sisters Anna and Lisa. I am so happy to have them and I am more than grateful that they are always there for me. Without all their love and support I would never have come this far, therefore my biggest and deepest gratitude goes to them.

## Table of Contents

1	Introduction.....	1
2	Scanning Probe Microscopy .....	2
2.1	Atomic Force Microscopy.....	2
2.2	Thermal Scanning Microscopy .....	7
2.3	Force Spectroscopy .....	8
2.4	Instrumentation .....	9
3	The Dual Beam Microscope.....	10
3.1	The Scanning Electron Microscope .....	12
3.2	The Focused Ion Beam .....	14
3.3	Particle – Matter Interaction.....	14
3.4	Patterning and Image Formation .....	17
3.5	Focused Electron Beam Induced Processing.....	18
3.5.1	Basics .....	18
3.5.2	The Adsorption Rate Model.....	19
3.5.3	3 Dimensional Nanofabrication .....	21
3.5.4	Post-Deposition Treatment .....	22
3.5.5	Physical Properties of Deposits .....	23
3.6	Instrumentation .....	23
4	Simulations.....	24
4.1	Finite Element Method .....	25
4.1.1	Mesh .....	25
4.1.2	Equations and Solver .....	26
4.1.3	Accuracy and Convergence.....	27
5	Analysis of Mechanical Properties .....	27
5.1	The Underlying Model.....	28
5.1.1	Analytical Solution of a Single Pillar.....	28
5.1.2	Pre-investigations .....	29
5.1.3	Simulations – Single Pillar .....	31
5.1.4	Bipod and Tripod .....	32
5.1.5	Tetrapod .....	38
5.1.6	Overall Behavior .....	41
5.2	Deposition of Tetrapods.....	43

---

5.3	Preparation and Characterization of the Cantilever .....	46
5.4	Qualitative Measurements.....	47
5.5	1 <sup>st</sup> Adaptation of the Model .....	50
5.6	Quantitative Measurements .....	52
5.7	2 <sup>nd</sup> Adaption of the Model .....	56
5.8	Imaging Capability of Nano-Probes.....	60
6	Heat Transfer Simulation.....	62
6.1	Analytical Solution.....	63
6.2	Simulations.....	64
7	Observations on Shape Change Effects.....	65
8	Summary and Upcoming Challenges.....	70

## List of Abbreviations

Amorphous Carbon	.....	aC	Heat conductivity	.....	k
Aspect Ratio	.....	AR	Height	.....	H
Atomic Force Microscope	.....	AFM	Measured Voltage in Wheatstone Bridge	.....	$V_w$
Axial	.....	a	Molecule Limited Regime	.....	MLR
Backscattered Electron	.....	BSE	Partial Differential Equation	.....	PDE
Computer Aided Design	.....	CAD	Platinum	.....	Pt
Density	.....	$\rho$	Point Pitch	.....	PoP
Diagonal	.....	d	Poisson's Ratio	.....	$\nu$
Diameter	.....	D	Primary Electrons	.....	PE
Displacement	.....	u	Primary Ions	.....	PI
Dual Beam Microscope	.....	DBM	Radial	.....	r
Dwell Time	.....	DT	Refresh Time	.....	RT
Effective	.....	eff	Scanning Electron Microscope	.....	SEM
Electron Limited Regime	.....	ELR	Scanning Probe Microscopy	.....	SPM
Finite Element Method	.....	FEM	Scanning Thermal Microscopy	.....	SThM
Focused Electron Beam Induced Deposition	.....	FEBID	Secondary Electron	.....	SE
Focused Electron Beam Induced Processing	.....	FEBIP	Self-Sensing Cantilever	.....	SSC
Focused Ion Beam	.....	FIB	Stiffness	.....	k
Force	.....	F	Take-Off	.....	TO
Forward scattered electron	.....	FSE	Total	.....	tot
Gas Injection System	.....	GIS	Young's modulus	.....	E
Heat capacity at constant pressure	.....	$C_p$			

# 1 Introduction

Although we are accustomed to the everyday usage of high-tech applications directly (smartphones, computer, ...) and indirectly (automotive, solar energy, ...) the tremendous effort of development behind these devices is barely visible to the naked eye. Besides the inexhaustible resources of motivation and creativity, the available characterization methods during the design process play a crucial role. However, it is exactly the realization of a certain design and the precise characterization techniques that run up against physical and chemical boundaries with increasing miniaturization. For instance, the information about the temperature distribution, the thermal capacitance and the thermal conductance in the nanometer range is essential for energy materials as it can heavily influence their functionality and operating regimes<sup>1,2</sup>. But very often these parameters are not accessible on the desired scale and one has to rely on simulations to understand the behavior of such devices.

Based on this challenge the group of Ass.Prof. Harald Plank is developing in cooperation with SCL-Sensor.Tech.Fabrication<sup>3</sup> and GETec Microscopy<sup>4</sup> within the framework of the SENTINEL project a concept for thermal high-resolution nanoprobes. The idea is based on a work done by Rangelow et al.<sup>5</sup>, who showed that by Focused Electron Beam Induced Deposition a nanoprobe can be deposited on a cantilever and this way be utilized as a temperature sensitive element. However, one major problem to be solved concerns the mechanical stability of such nanostructures, as the very tip of them will come in contact with the investigated surface, hence experiencing a certain displacement and induced mechanical stress. Therefore, to maintain the shape of the investigated nanostructures, to receive reliable measurements and to avoid uncontrollable measurement artifacts a thorough investigation and determination of the mechanical properties is of fundamental importance.

## 2 Scanning Probe Microscopy

Scanning Probe Microscopy (**SPM**) comprises microscope techniques that are based on different kinds of interaction between a fine tip and a surface or single molecule in order to obtain morphological information of the surface and / or to investigate certain properties, e.g. conductive, magnetic, chemical, mechanical and many others. The first type of microscope developed according to this general principle was the Scanning Tunneling Microscope<sup>6</sup> (**STM**) utilizing the tunneling current between the tip and a biased surface to obtain information about the surface topography, the work function or the local density of states. Due to a current flow between tip and surface, the latter has to be conductive in order to obtain reliable signals. This problem was bypassed with the introduction of the atomic force microscope<sup>7</sup>, by utilizing the forces between tip and surface as an indicator.

### 2.1 Atomic Force Microscopy

The basic principle of the Atomic Force Microscope (**AFM**) is similar to a stylus profilometer<sup>8</sup>, in which a fine stylus with a sharp apex is contacted with the surface and then dragged along a line. The vertical movement of the stylus is recorded and gives information about surface roughness. While the stylus profilometer measures just a single line (1D), the AFM is rastering several hundred lines (2D). Adding the height information during rastering of the surface one obtains qualitative and quantitative 3D information of the sample surface. This is a major advantage compared to STM and stylus profilometry. Height information below 1 nanometer can be obtained, an accuracy that is not feasible with any other available microscopy technique<sup>9</sup> for nonconductive surfaces. Furthermore, various measurement modes allow highly resolved information, such as magnetic properties, material / chemical distribution, electrical conductivity, mechanical properties and many more<sup>9</sup>. Measurement can be done in different environments (liquid, gas or vacuum), making time-resolved *in-situ* studies possible.

The basic setup of an AFM is shown in Figure 1, consisting of a sample stage (a), scan head (b), cantilever (c) and tip (d), a detection system for the cantilever deflection (e) and a readout and control unit.

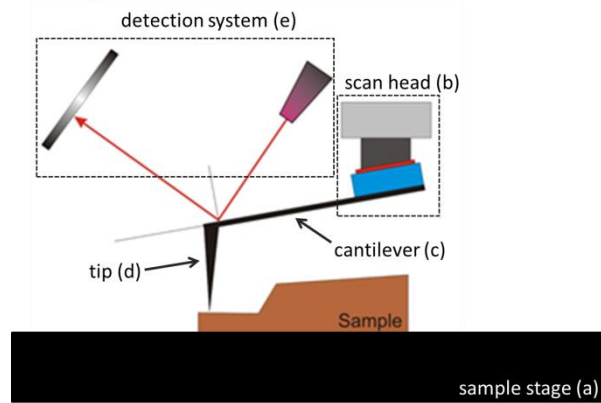


**Figure 1:** basic setup of an AFM consisting of a sample stage (a), a scan head (b), a cantilever (c) with tip (d), a detection system for the cantilever deflection (e), which is in this case realized by a laser and the detection of the reflection with a position sensitive photodetector<sup>10 (modified)</sup>.

In general, either the sample stage or the scan head is moved in  $x, y$  and  $z$ -direction to scan the surface with the tip. In the above-shown figure the scan head is moved, which is the same case for the used systems. Coarse movement is controlled by mechanical means, fine movement down to the picometer range by piezoelectric actuators. Applying either positive or negative bias will lead to expansion or contraction of the piezoelectric material, as shown in Figure 2 (a). For movement in  $z$ -direction one pair of electrodes is sufficient, for movement in lateral direction 4 pairs of electrodes are necessary, whereupon electrode pairs on opposite sides are actuated vice versa (b). While one side will contract the other will expand, leading to a net main axis displacement in a particular direction.

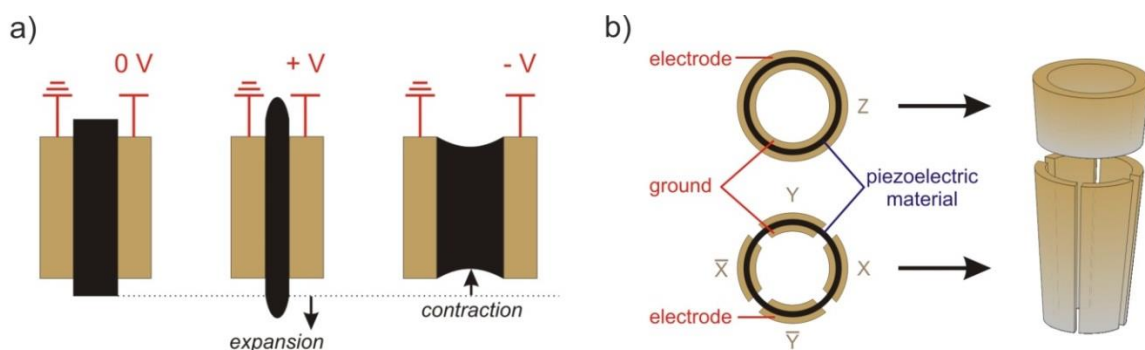


**Figure 2:** (a) functional principle of piezoelectric material (black) activated expansion and contraction due to positive or negative bias. Hence for a particular arrangement of actuators and electrodes movement in  $x, y$  and  $z$ -direction is possible (b)<sup>10</sup>.

Identification of the cantilever deflection due to the tip – surface interaction is done in most systems by measuring the change of a reflected laser spot on the cantilever via a position sensitive detector, as shown in Figure 1. In another approach the deflection sensing element is integrated into the

cantilever itself (a self-sensing cantilever (**SSC**), Figure 3 (a)), by means of a piezo resistive sensor, whose change in resistance  $R_{pr}$  due to deformation is measured by a Wheatstone bridge (b). In this circuit, it is possible either to adjust  $R_2$  in such a way that the output voltage  $V_w$  will be zero or to measure  $V_w$  as  $R_{pr}$  changes. Thus the voltage in the Wheatstone bridge  $V_w$  can be correlated to the applied force on the cantilever, which in turn can be linked to the mechanical properties of investigated structures, which is discussed in more detail in section 2.3.

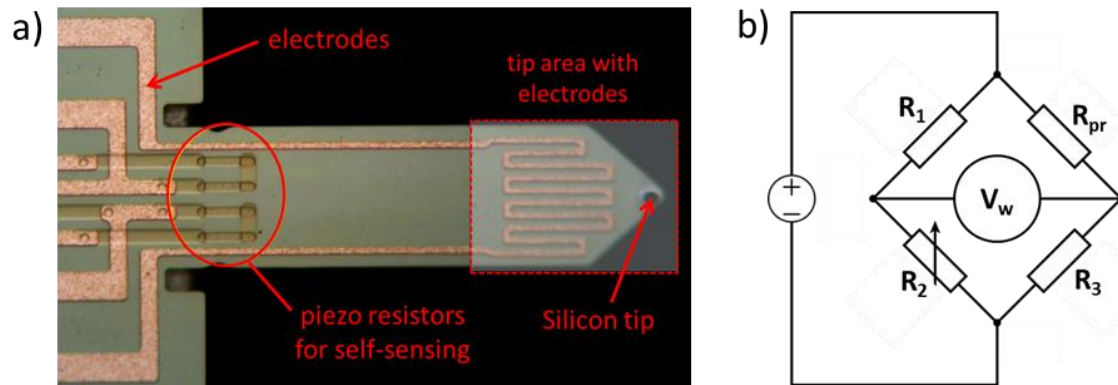


**Figure 3:** (a) a self-sensing cantilever with a silicon tip at its end, the tip area with electrodes will be later on modified, the piezo resistors for self-sensing, whose change in resistance  $R_{pr}$  is measured by a Wheatstone bridge as shown in (b). Due to a change of the resistance, a change in the output voltage  $V_w$  is measured. By adjusting a variable resistance  $R_2$ ,  $V_w$  can be set equal to zero<sup>11 (modified), 12 (modified)</sup>

The biggest improvement of SSCs is the reduced space needed, as the optical readout system consisting of a laser and a photodiode is completely replaced by piezo sensors which are placed on the cantilever itself. In addition to that, laser alignment of the cantilever relative to the source and the photodetector is not necessary. Furthermore, it was shown by Fantner et al. that such a readout system can achieve a better lateral resolution and is less prone to thermal noise compared to systems with optical readout<sup>13</sup>. Hence this technique represents a big leap forward to the miniaturization of AFMs, opening the potential of integration and combination with other microscopes, such as Dual Beam Microscopes.

As mentioned before the determination of the surface topology is done by measuring the deflection of the cantilever, which is caused by the interaction of the tip with the surface. For classic AFM three basic kinds of interaction between tip and surface come into play, i.e. electrostatic / magnetic, dominating for distances larger than 10 nm, Van der Waals / Dipole – Dipole, 10 nm to 0.5 nm,  $e^- - e^-$  repulsion (Pauli Exclusion Principle), smaller than 0.2 nm. The latter two are typically summed and denoted as the Leonard Jones Potential<sup>14</sup>, whose generic force curve, depicted as a black line in Figure 4 (a), showing two major regimes, i.e. repulsive (highlighted red) and attractive (highlighted green). Hence an approaching tip will first be attracted towards the sample surface, resulting in a negative deflection of the cantilever towards the surface (C) and a decrease of the voltage in the Wheatstone bridge. By lowering the cantilever further the repulsive regime becomes dominant and a

positive deflection upwards relative to its initial displacement is observed (D), leading to an increase of voltage in the Wheatstone bridge.

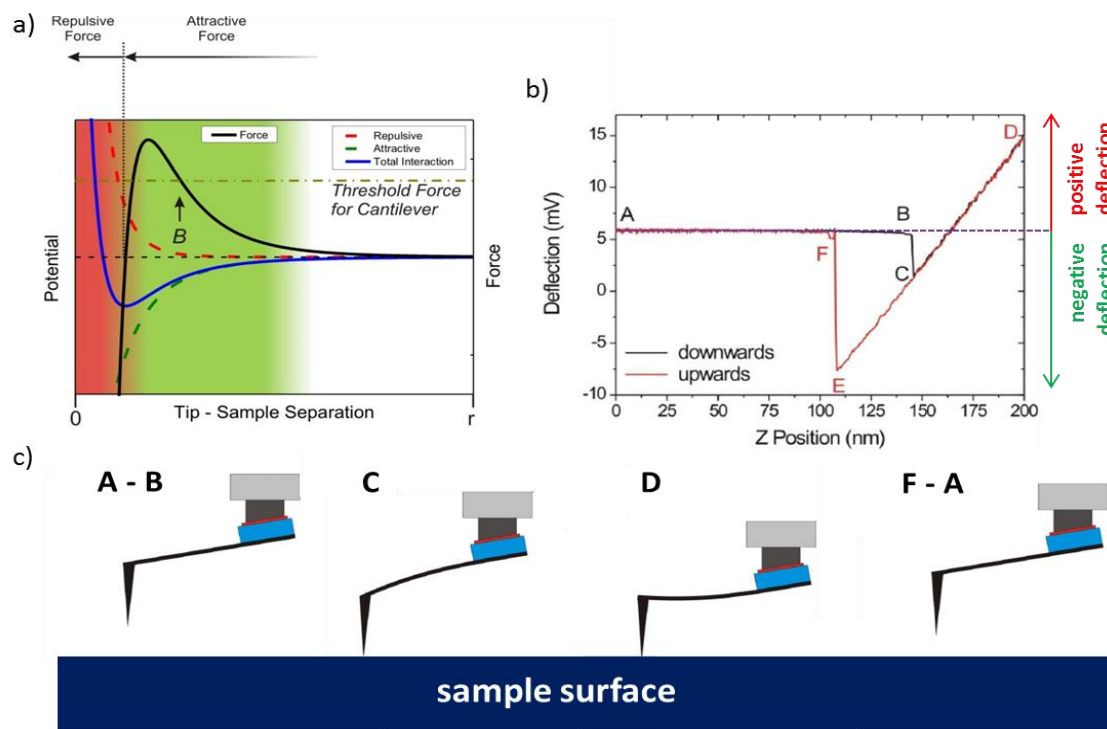


**Figure 4:** (a) repulsive (red dashed line) and attractive (green dashed line) potential result in a total interaction potential (blue solid line), thus a force (black solid line) acts on the cantilever tip. Therefore during approach the cantilever will at first not deflect (between point A to B in (b) and (c)), at the threshold force the cantilever will snap towards the surface (C), at one point upwards deflection of the cantilever will occur (D). As well one can see, that during retrace the cantilever is longer in contact with the surface, due to additional adhesion forces. At (E) it will again snap back and is instant without any deflection (F), then goes back to the starting position (A) and one cycle of the force ramp is finished<sup>19 (modified)</sup>.

There are several operation modes possible in order to depict the sample surface. Most important for the present thesis is the contact mode, in which the tip is dragged along the surface and for each pixel / measurement point the height of the scan head is adjusted in such a way that the force between tip and sample, indicated by  $V_w$ , is kept constant. Hence the cantilever exhibits the same prescribed deflection in each point, as depicted in Figure 5, although for the shown system detection of deflection is realized by an optical readout system. Furthermore, since the tip is in constant contact with the surface, several disadvantages emerge, amongst others the destruction of the material by indentation and scratching, delamination of surface layers as well wear off of the tip itself has to be considered, hence the mechanical properties about the tip itself are of utmost importance.

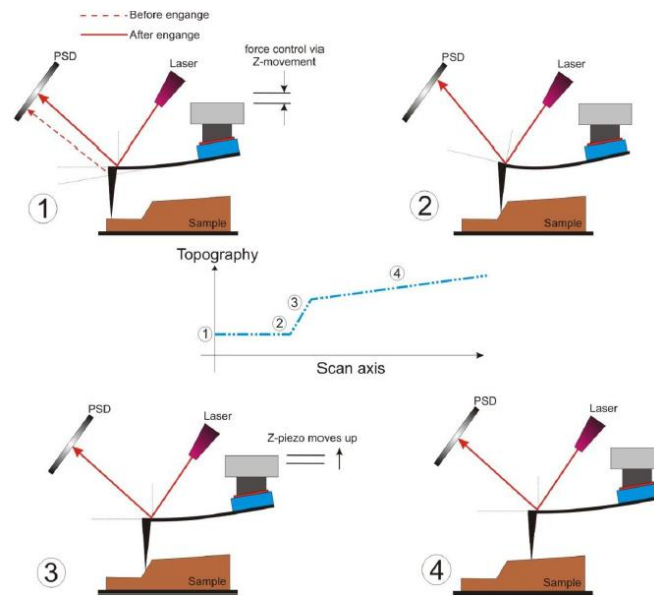


**Figure 5:** during contact mode AFM the force between tip and sample is kept constant to obtain information about the surface topography. Hence in step (2) the scan head moves upwards until a certain deflection of the cantilever is adjusted (3) and goes on to the next point repeating this procedure<sup>10</sup>.

While the height resolution with an AFM is excellent (usually below 1 nm) the ultimate lateral resolution is determined by the diameter of the apex, the shape of the tip and potentially present impurities. First of all the diameter of the tip apex should be as fine as possible, thus the tip can access even small cavities giving a well-resolved image, as a comparison between a fine (a) and a dull (b) tip in Figure 6 shows. In actual fact, the highest achievable resolution is limited to the diameter of the apex, which therefore should be as fine as possible. Next the shape of the tip will always lead to an intrinsic broadening (a) and for high aspect ratio structures to a side wall angle convolution, at which vertical walls cannot be depicted as such, as the tip apex cannot access the corners directly, due to the conic shape of the tip (c). At last impurities, which are attached to the apex or the side of the tip will, as depicted in (c), lead to an additional impurity related convolution.

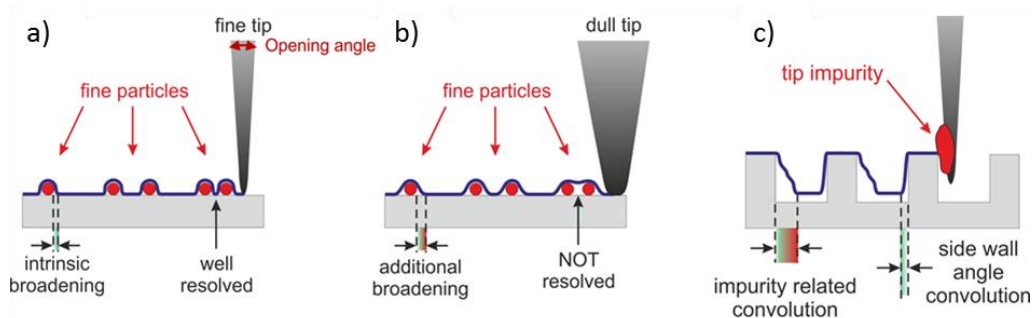


**Figure 6:** (a) some kind of intrinsic broadening of the image is unavoidable even for fine tips, however, a fine tip is desirable in order to be able to resolve even small sample features, which is not possible with a dull tip (b). (c) in addition side wall angle convolution will always be present in AFM images due to the opening angle of the tip and imaging artifacts might occur due to tip impurities<sup>10</sup>.

## 2.2 Thermal Scanning Microscopy

Using a heat sensitive tip turns the AFM into a Scanning Thermal Microscope (**SThM**). Specifically, a certain property of the probe, such as thermovoltage, change in electrical resistance or thermal expansion is observed or controlled, as the probe gets in contact with the surface<sup>15,16,17</sup>. The first investigation of such a kind was done by Williams and Wickramasinghe<sup>18</sup>, who used a thermocouple junction in close proximity (non-contact) to the surface. Currently, SThM measurements are mostly done by using either a Wollaston Wire (Figure 7 (a)) or coated probes (b), both utilizing the change of electrical resistance in order to determine thermal properties. A major problem is their large tip radius, which gets barely below 50 nm, representing a strong restriction to the possible resolution, as discussed before<sup>19</sup>.

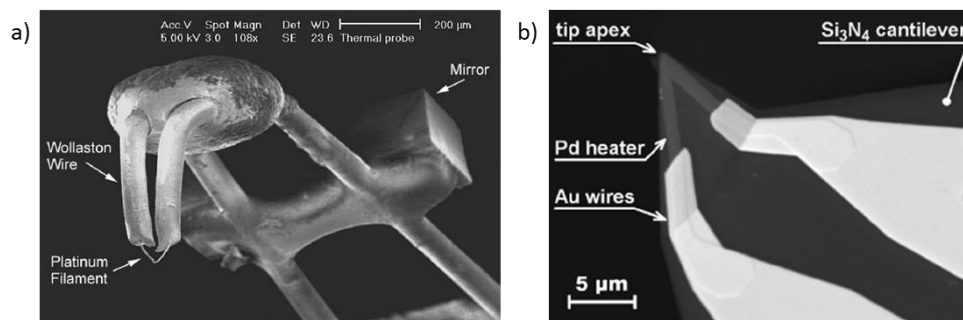


**Figure 7:** commonly used probes for SThM, (a) a Wollaston wire with an etched platinum filament<sup>20</sup>, (b) a Pd-coated cantilever<sup>21</sup>.

The field of operation modes in SThM currently allows thermometry measurements and thermal conductivity measurements. Thermometry, a measurement of the local sample surface temperature, is done by contacting the surface with the tip, leading to a change of the measured variable, which then can be correlated to the temperature on the surface. This in turn requests that a change of temperature and reaching a steady state temperature distribution in the probe tip has to happen rapidly to avoid long contacts with the sample surface, which would result on the one hand in long measurement times and on the other hand to a strong unwanted influence of the investigated surface<sup>19</sup>. Therefore certain probe architectures with small volumes and materials with high thermal conductivity and low specific heat capacity are favorable. Moreover, the exact behavior of the thermal probes under the influence of temperature change and hence an exact calibration is necessary in order to reliably correlate the change of the measured variable to the temperature.

## 2.3 Force Spectroscopy

As mentioned above the cantilever will experience a distinct deflection, due to the interaction between surface and tip. Fundamentally, the deflection of the cantilever tip and the interaction with the surface is equivalent to a serial connection of two or more springs (Figure 8), including the stiffness of the cantilever itself ( $k_c$ ), of the sample surface ( $k_{sa}$ ) and the probed structure ( $k_{st}$ ), for which the total stiffness ( $k_{tot}$ ) is given by Equation 1<sup>22</sup>. The elongation ( $\Delta z$ ) or compression of these springs can be described in the simplest case by Hooke's law<sup>22</sup> (Equation 2), making it possible to calculate the stiffness of an unknown structure, if one knows the stiffness of the cantilever. For the conducted experiments we assume that the stiffness of the sample compared to the other contributions is much larger, thus the inverse  $\frac{1}{k_{sa}}$  is in turn much smaller and the total stiffness is hence dominated by the cantilever and the structure. Therefore  $k_{st}$  can be written as Equation 3<sup>22</sup>. This approximation is only valid if no indentation occurs and the force driving the cantilever is perpendicular to the surface. Luckily all these factors account for the investigated systems, as we modified the cantilever in a particular manner to ensure that it will hit the nanostructures with a force driving perpendicular to the sample surface (section 5.3). No indentation occurs, as we can assume that the hardness of the sharp tip of the nanostructures compared to the cantilever tip is much smaller, due to the special composition of the respective material<sup>23,24</sup>.

$$\frac{1}{k_{tot}} = \frac{1}{k_c} + \frac{1}{k_{st}} + \frac{1}{k_{sa}} \quad \text{Equation 1}$$

$$F = k \Delta z \quad \text{Equation 2}$$

$$k_{st} = \frac{k_{tot}k_{sa}}{k_c - k_{tot}} \quad \text{Equation 3}$$

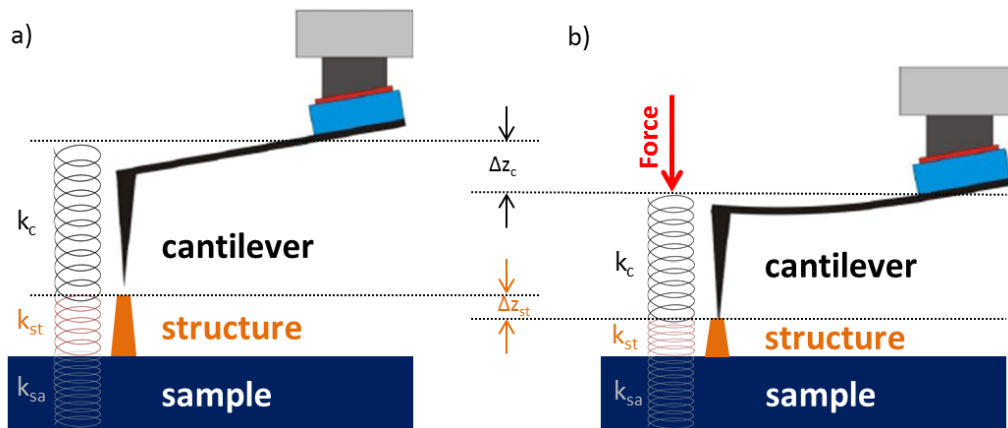


**Figure 8:** (a) the stiffness of cantilever, structure, and sample can be modeled as serial springs with their stiffness  $k_c$ ,  $k_{st}$  and  $k_{sa}$ , respectively. (b) if a force is applied to this system each spring will be compressed, relative to their stiffness<sup>10 (modified)</sup>.

## 2.4 Instrumentation

In this thesis the primarily used AFM is the AFSEM<sup>TM</sup>, which can be directly integrated into a Dual Beam Microscope as shown in Figure 9. For force spectroscopy the cantilever was provided by SCL-Sensor.Tech.<sup>3</sup> and modified as described in 5.3 beforehand to allow site-specific force spectroscopy measurements of 3D nanostructures. During investigations the stage of the DBM was tilted to  $-15^\circ$ , thus information about the qualitative movement of the structures was obtained by SEM imaging. Furthermore, a special scanner and sample holder were used<sup>25</sup>, so the scan head would move perpendicular towards the sample surface. Estimation of the cantilever stiffness was done via Finite Element Simulation and is discussed in section 5.3.

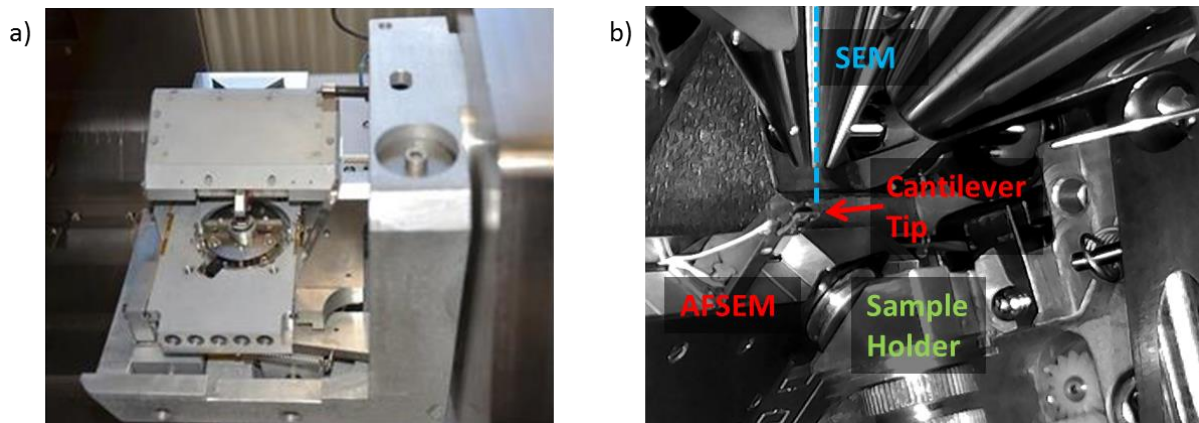


**Figure 9:** (a) the AFSEM as built into the DBM<sup>A</sup>. (b) a look into the DBM chamber while the AFSEM is installed shows that it was possible to view deformations with the electron beam (SEM).

### 3 The Dual Beam Microscope

The Dual Beam Microscope (**DBM**) combines the capabilities of a Scanning Electron Microscope (**SEM**) with the ones of a Focused Ion Beam (**FIB**), allowing high-resolution imaging and modification as well material removal of larger areas. Either can be used in combination with a precursor gas delivered to the surface by a Gas Injection System (**GIS**) to allow for site-specific deposition and / or etching<sup>26,27,28,29</sup>. Thanks to its theoretical imaging resolution of 1 nm and 5 nm for the SEM and the FIB, respectively, as well the possibility of fast mask-less direct write high-resolution 3D nano-fabrication the DBM is an incomparable nano processing tool. Within this field lies also the typical range of application, as shown in Figure 10: site specific sub-surface investigation (a), lamella preparation (b) for further transmission electron microscope investigations, circuit editing (d), mask repair and fabrication of functional (e) and delightful (c) nanostructures.

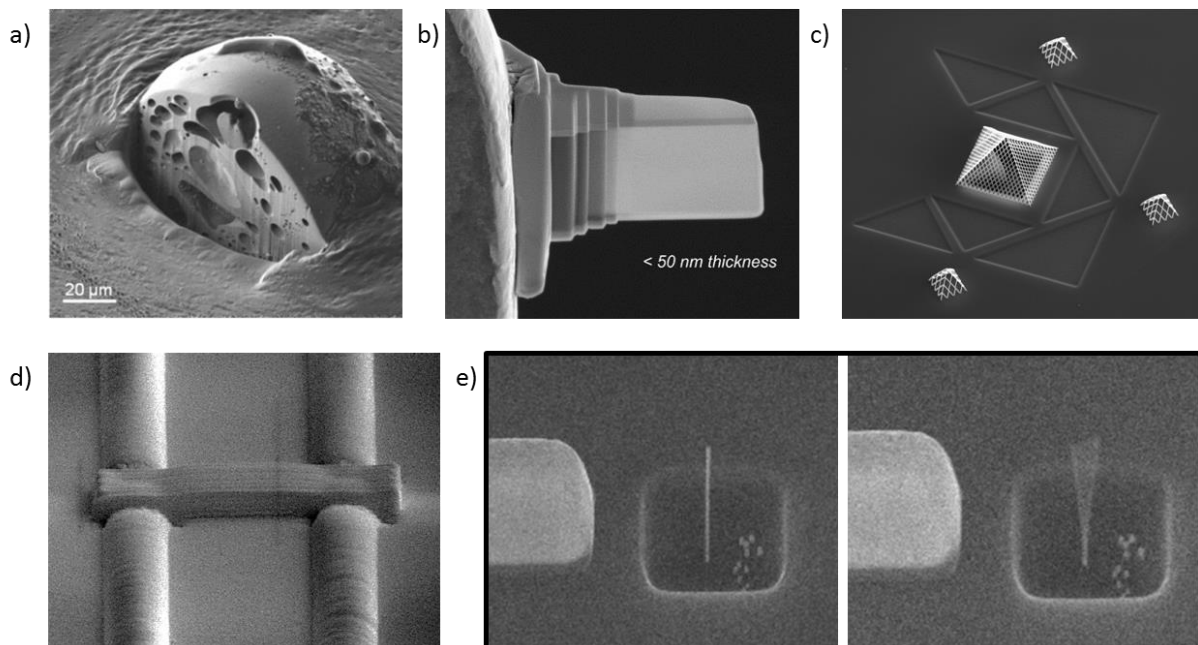


**Figure 10:** among many applications the DBM is capable of (a) site-specific sub-surface investigations<sup>10</sup>, (b) lamella preparation for transmission electron microscopy<sup>10</sup> (c) the fabrication of highly complex nanostructures<sup>25</sup>, (d) circuit editing<sup>30</sup>, (e) fabrication of functional nanostructures<sup>23</sup>.

During investigations the chamber of the DBM is kept under high vacuum, generated by a pump system consisting of a rotary vane pump and a turbomolecular pump. Furthermore, the FIB and SEM column are kept under ultrahigh vacuum by additional ion getter pumps, to allow for as long mean free paths of ions and electrons as possible. This is necessary in order to minimize electron scattering with gas atoms, thus keeping the electron / ion beam confined. Vertically integrated into the chamber is the SEM column, whereas the FIB column is integrated with respect of 52° to the SEM column, as shown in Figure 11 (a). The resulting point of coincidence for the particle beams is known as the “eucentric height”. While operating on a certain spot at the eucentric height, tilting of the

sample stage will keep this certain spot in focus. Therefore the eucentric height defines the working distance for the SEM and the FIB, which is about 4.9 mm and 19.5 mm, respectively. All Gas Injection Systems and detectors are optimized to this specific eucentric height. The insight of the DBM chamber is shown in Figure 11 (b), at which also one can see the interior alignment of the particle beam columns, as well various Gas Injection Systems and detectors.

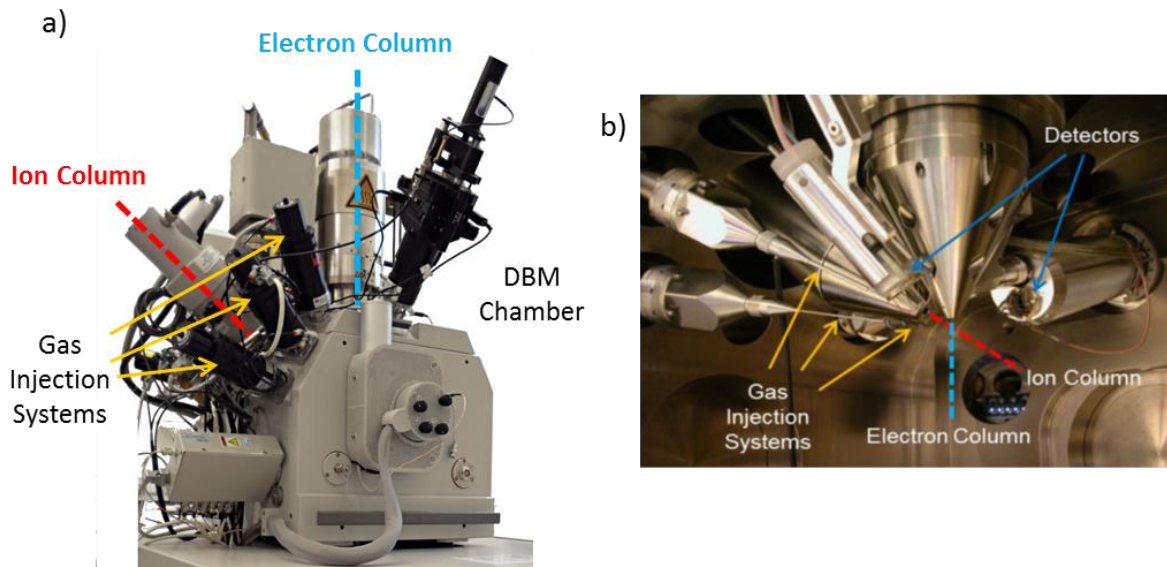


**Figure 11:** (a) the outside of the DBM, shows the integration of the electron and ion column into the DBM chamber. (b) the inside of the chamber shows the point of coincidence for electron and ion column, i.e. the eucentric height. Furthermore, one can see that several other features are aligned with this particular point<sup>10</sup>.

### 3.1 The Scanning Electron Microscope

The electron column, schematically shown in Figure 12 (a), consists of an electron source at the top and a lens system focusing the electron beam on the main optical axis and this way guiding the electrons towards the sample<sup>33</sup>. In more detail, the electron source, a Schottky Field Emitter (b), a heated tungsten tip with a  $ZrO_x$  coating, is placed in an electric field. The coating on the one hand reduces the work function of the tungsten tip, on the other hand the heating and the locally high electric field at the apex of the tip facilitates electrons to tunnel through the potential barrier of the material<sup>31</sup>. Emitted electrons are subsequently bundled by a Wehnelt cylinder into the 1<sup>st</sup> crossover, the virtual point source of the SEM. Subsequently, in the condenser lens system the electron beam is accelerated to 30 keV and the beam current is adjusted for values between 2 pA and 37 nA. Furthermore, the beam is demagnified and aligned to the optical axis. The lenses in the column are realized by means of magnetic coils (c), copper windings placed in an iron shell with a short opening (pole piece), in order to generate a preferably defined magnetic field in a short path and to minimize stray fields<sup>34</sup>. After the 2<sup>nd</sup> condenser lens the beam is decelerated to the desired value and guided

into a further lens system (DC upper and DC lower), which allow for the deflection of the beam, therefore scanning of the sample with the electron beam becomes possible. Finally, the electron beam is focused on the sample by the search final lens during normal operation (Search mode). During ultra-high resolution (UHR) imaging (black dashed line in (a)) the search final lens is turned off and the electron beam is aligned first parallel to the optical axis by the Intermediate lens and with a high convergence angle focused on the sample by the UHR final lens. Due to the high convergence angle, certain lens errors are minimized, thus allowing for a better resolution.

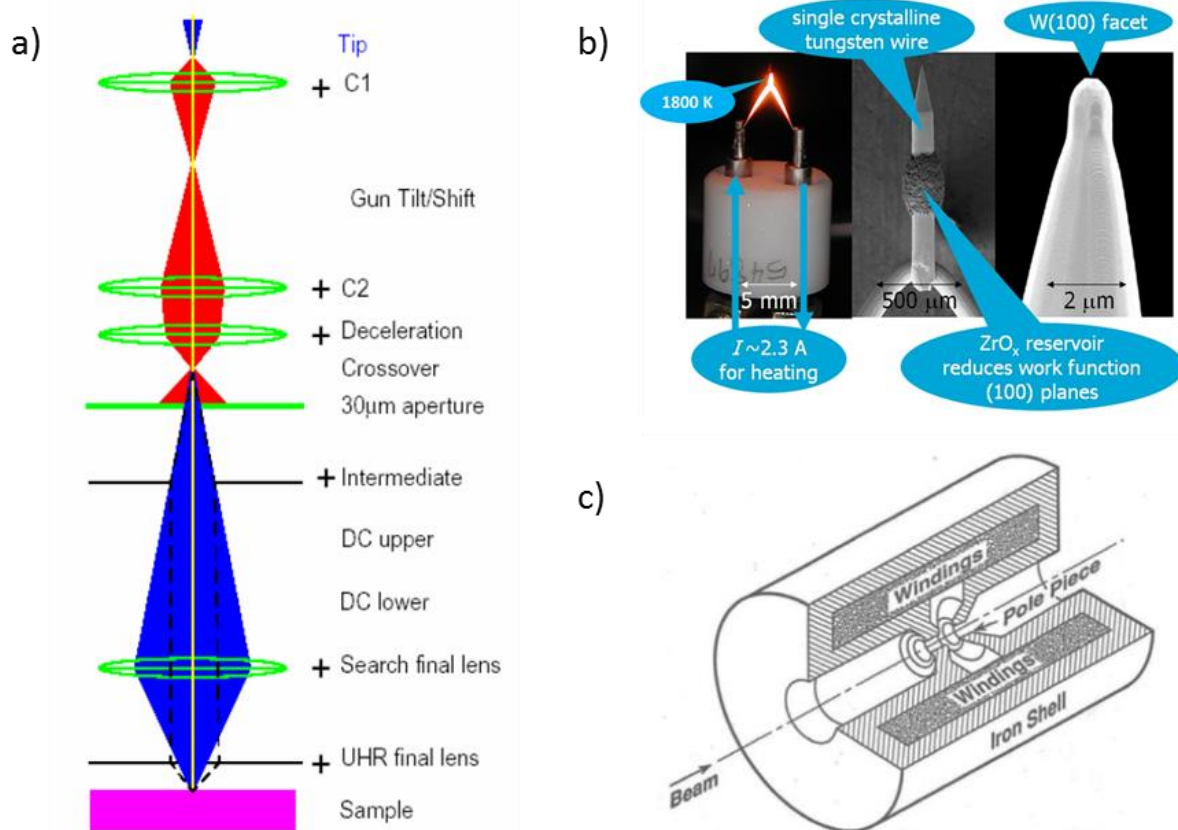


**Figure 12:** (a) schematic diagram of a SEM column showing the various lens systems (green), the electron beam generated at the tip (depicted in (b)) passes through the condenser lens system (red beam), is adjusted to the proper energy, then guided (blue beam) through DC upper and DC lower, where it can be deflected in x and y-direction, enabling rastering. Finally, in Search mode, the beam is focused on the sample by the Search final lens. (b) heating of a Schottky Field Emitter at a closer look one can see the  $ZrO_x$  reservoir of the tungsten tip, and the very end of the tip is a W(100) facet. (c) schematic cross section of an electron lens as it is used in the SEM column<sup>32,33,34</sup>

Theoretically, the resolution limit  $\delta$ , i.e. the smallest resolvable feature, of the SEM is determined by the Rayleigh criterion (Equation 4), a function of the wavelength  $\lambda$ , the refractive index  $n$  and the semi-angle of collection  $\beta$ . The wavelength of the electrons in turn is determined by de Broglie's

equation (Equation 5), as a function of the Planck constant  $h$ , the charge  $q$ , the mass  $m$  and the acceleration voltage  $U$  of the electron.

$$\delta = \frac{0.61 \lambda}{n \sin(\beta)} \quad \text{Equation 4}$$

$$\lambda = \frac{h}{\sqrt{2qmU}} \quad \text{Equation 5}$$

With a wavelength of about 7 pm for 30 keV electrons, the limit of resolution would thus be at 4 pm. However, this value is not achievable in practice for several reasons. First of all certain lens errors, due to non-perfect lenses, electron sources and electromagnetic stray fields from outside the column come into play, hence increasing this value. Moreover, the electron beam is not confined to a single spot but as it impinges on the surface has a gauss like distribution, whose Full-Width Half Maximum is denoted as the beam diameter ( $d_B$ ). Finally, as the electrons enter the substrate certain interactions will lead to the formation of the interaction volume and by that increasing the smallest resolvable feature even further.

## 3.2 The Focused Ion Beam

In comparison to the SEM the FIB column, Figure 13 (a) differs mainly by the particle source and the lens system. The former is a gallium liquid metal ion source (**LMIS**), schematically shown in (b), consisting of a metal reservoir, a tungsten needle, and extractor electrodes. The Ga-filled reservoir is heated above its melting point (29.8° C), leading to the wetting of the tungsten needle down to the apex. Due to the present electric field of the below-lying extractor electrodes the liquid Ga droplet experiences a distinct deformation, a Taylor cone, which in turn leads to an increase in curvature at the apex of the droplet, resulting in a high electric field intensity. As a result valence electrons of the Ga atoms are able to tunnel through the potential barrier, hence the Ga atom becomes ionized and is then accelerated towards the extractor electrodes and guided towards the condenser lens system, where the ion beam is accelerated to the desired energy, demagnified and aligned to the main optical axis. By the beam defining aperture, the current of the ion beam is determined at discrete values in a range from 1 pA to 20 nA. Finally, the  $\text{Ga}^+$  ions pass through octopole coils, which enable deflection of the beam for rastering followed by the objective lens, which focuses the ions on the sample.

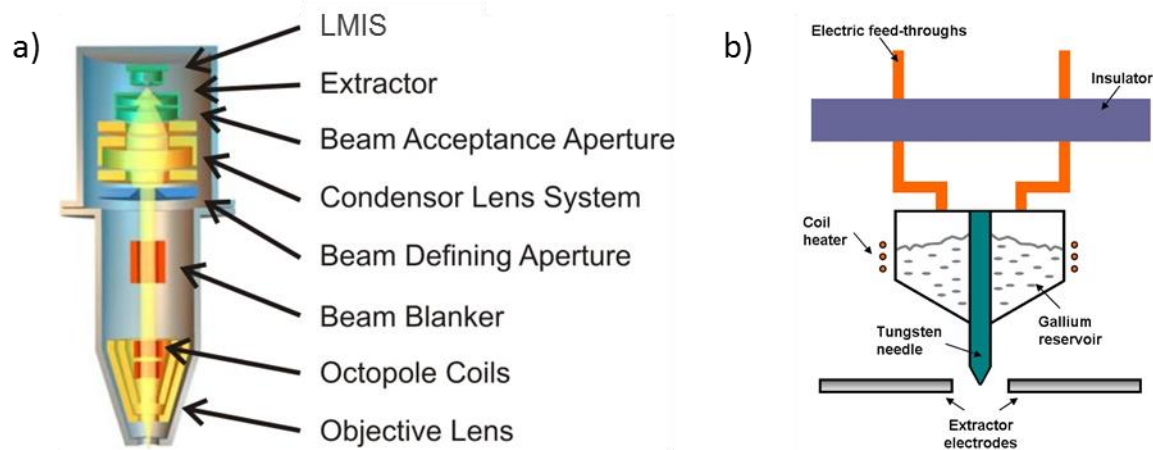


**Figure 13:** (a) schematic cross section of a FIB column. Ga ions are generated by a liquid metal ion source (LMIS, shown in (b)) and are then guided through the ion column, at which they are focused and aligned on the optical axis, as well the beam current and energy is adjusted. (b) the liquid metal ion source consists of a Ga-filled reservoir, which is heated. Thus liquid Ga can wet the tungsten needle, leading to the formation of a Ga droplet at the apex of the needle and subsequent deformation into a Taylor cone due to the extractor electrodes. From the Taylor cone,  $\text{Ga}^+$  ions are then emitted towards the extractor electrodes<sup>10,32</sup>.

### 3.3 Particle – Matter Interaction

After guidance through the column the electrons, denoted as primary electrons (**PE**) will hit the surface of the sample and enter the bulk. Within the bulk elastic and inelastic interaction with atoms and their electrons will lead to a change of direction, thus the formerly confined beam broadens and the so-called interaction volume is formed, as shown in Figure 14 (a) by a Monte Carlo simulation using the software CASINO<sup>35</sup>. Its size and shape are determined by the primary beam energy, the density and the mean atomic number of the bulk. In general for higher energy, at the same bulk properties, one will observe a larger size of the interaction volume. The same goes for lower density and smaller mean atomic number at the same primary beam energy. Fundamentally, the interaction volume can be seen as the source of a range of signals with different depths of origin (b): backscattered electrons (**BSE**), secondary electrons (**SE**), Auger electrons (**AE**), as well x-ray and light.

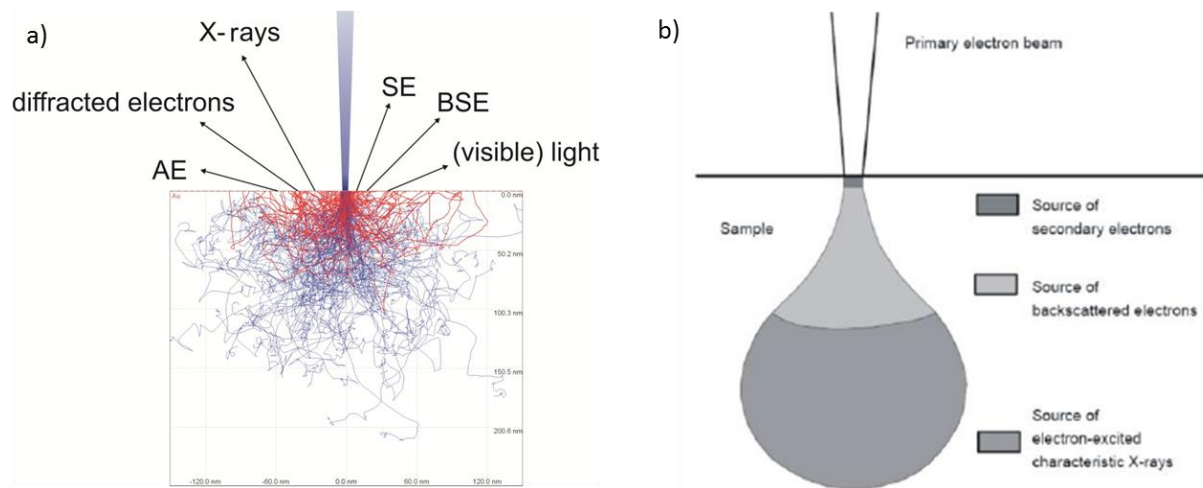


**Figure 14:** (a) formation of an interaction volume due to elastic and inelastic scattering of the PE, the path of the electrons in the sample were simulated using CASINO<sup>35</sup>. (b) the virtual range of depth for various species generated in and due to these scattering processes<sup>10</sup>.

In more detail, for elastic scattering events, i.e. mainly interactions with atomic nuclei, the electrons will experience no energy loss but a strong deflection, for which the angle of deflection depends primarily on the mean atomic number of the bulk<sup>34</sup>. At inelastic scattering events, which are collisions of electrons with weakly bound valence electrons and inner shell electrons, portions of the PE energy is transferred to them, hence they are able to leave the atom in an ionized state<sup>34</sup>. Inelastic collisions between PE and bulk atoms are neglected at this point, as they will neither lead to sputtering effects nor a significant signal, due to the relatively low mass of the electron compared to the atom nuclei. As PE enter the bulk they will typically experience a mixture of these processes, leading to the different aforementioned kinds of electrons, specified by their energy, as shown in Figure 15 (a), SE below 50 eV, BSE in the range between 50 eV and the energy corresponding to the acceleration voltage  $eU$ , with low-loss electron (LLE) at the very maximum of this energy range, which are PE that only experience elastic scattering. Furthermore, AE can be found at distinct peaks not contributing to the continuum of the spectrum, which is explained below, as well plasmon losses occur at distinct peaks, these are energy transfers of the PE / BSE to the valence electrons of the bulk, leading to the generation of collective electron oscillations (plasmons). Secondary electrons itself can be divided according to their origin into  $SE_1$ , which are generated at the irradiated area directly by the PE;  $SE_2$ , which are generated by BSE, hence they are typically farther away from the beam center; and  $SE_3$ , which arise from forward scattered PE. Since SE have a relatively low energy, their mean free path within the bulk materials is very short, so their origin is within several nm to the surface making them the ideal choice for imaging in the SEM.

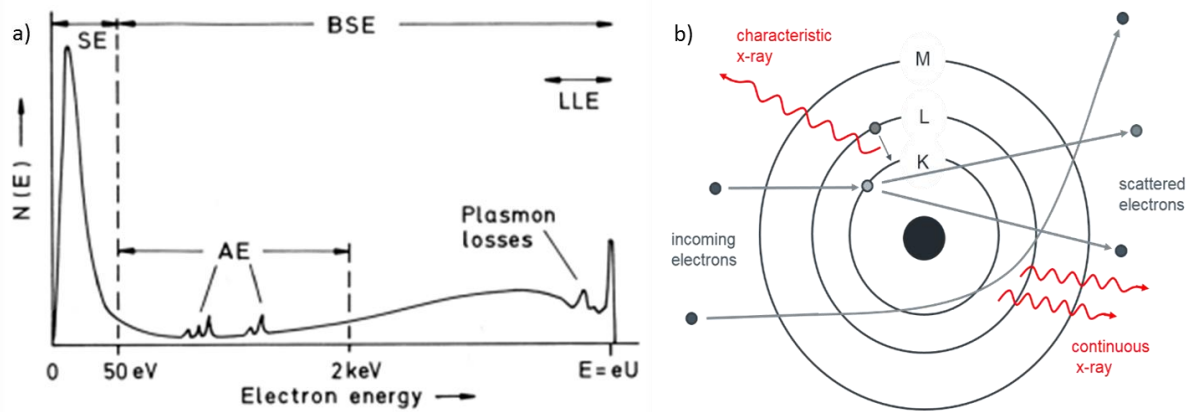


**Figure 15:** (a) the energy spectrum of reemitted and generated electrons, dividing into secondary electrons (SE) at energies below 50 eV, which are generated as primary electrons and backscattered electrons knock bulk atom valence electrons out of their shell. The energy defining BSE ranges up to the energy corresponding to the acceleration voltage of PE ( $eU$ ), where low-loss electrons (LLE) can be found. BSE can have arbitrary values within this range, while Auger electrons contribute with specific peaks to the spectrum, due to their generation process, as well plasmon losses, i.e. excitations of collective oscillations of the valence electrons in the bulk have distinct peaks<sup>36</sup>. (b) schematic representation of the generation of characteristic and continuous x-ray.

As bound electrons are knocked out from inner shells of the bulk atoms, outer shell electron can relax into the inner shell vacancy, representing a state of lower energy, as schematically shown in Figure 15 (b). The energy difference between these states is emitted either as x-ray or transferred onto a valence electron, which is subsequently emitted, better known as an Auger electron. Since the electron shells of elements have specific energy values, the emitted x-ray or AE will as well have a characteristic energy. Thus by recording a spectrum of these, one can identify the elements of the specimen by comparing the peak values to a database. Besides these characteristic peaks, one can see as well a continuum, which at first rises up at a few eV and then declines. The continuum emerges due to deceleration of PE within the field of the bulk electrons, leading to an indistinct loss of energy in form of a photon, for which the maximum intensity would be actually close to 0 eV. This however, cannot be seen by the detector, as these photons are absorbed by the protective entrance window of the detector. Towards the maximum value, the intensity of the continuum decreases exponentially and is finally limited by the maximal deceleration energy, i.e. the PE energy  $eU$ .

Compared to electrons impinging ions, denoted as primary ions (PI) will have, at the same acceleration voltage, a much smaller interaction volume, due to a higher interaction cross section and much larger stopping power, e.g. 30 kV  $\text{Ga}^+$  ions in Si have a penetration depth of roughly 700 Å, while the penetration depth for electrons with the same acceleration voltage in the same material is about 5 orders of magnitude higher. In addition due to their much higher mass PI will carry a much higher momentum, which will be transferred upon the bulk atoms launching collision cascades and in general leading to an extensive generation of phonons in the sample. In the process of the former SE, backscattered and secondary ions and excited surface atoms are generated, as well collision cascades ending at the surface can lead to direct removal of these atoms / clusters. Furthermore, phonon generation comes along, hence the sample is heated around the ion beam and this will lead to evaporation of the material. Both processes contribute to the material removal, called sputtering<sup>27,37</sup>.

Detection of SE and BSE is done for the used DBM primarily by the Everhart-Thornley Detector (ETD), schematically depicted in Figure 16. In principle, it is a scintillator for the detection of electrons, which is connected to a photomultiplier in order to amplify the signal. In front of the scintillator is a Faraday Cage, with adjustable bias. In case of a negative bias BSE are due to their high energy still able to reach the scintillator and generate a signal, while SE are deflected away from the grid. As the intensity of BSE depends on the mean atomic number and density of the sample it is possible to obtain qualitative information on different phases of the sample. Otherwise, if a high surface resolution is desired the cage is positively biased and will attract SE towards the scintillator, which will be then the highest contribution to the signal. Since the ETD has a distinct position within the DBM more SE and BSE are detected, from areas facing towards the detector. In addition, edges will contribute more to the signal compared to flat surfaces since the surface around the excited volume is bigger. In total, both effects will give a certain 3D character to SEM images.

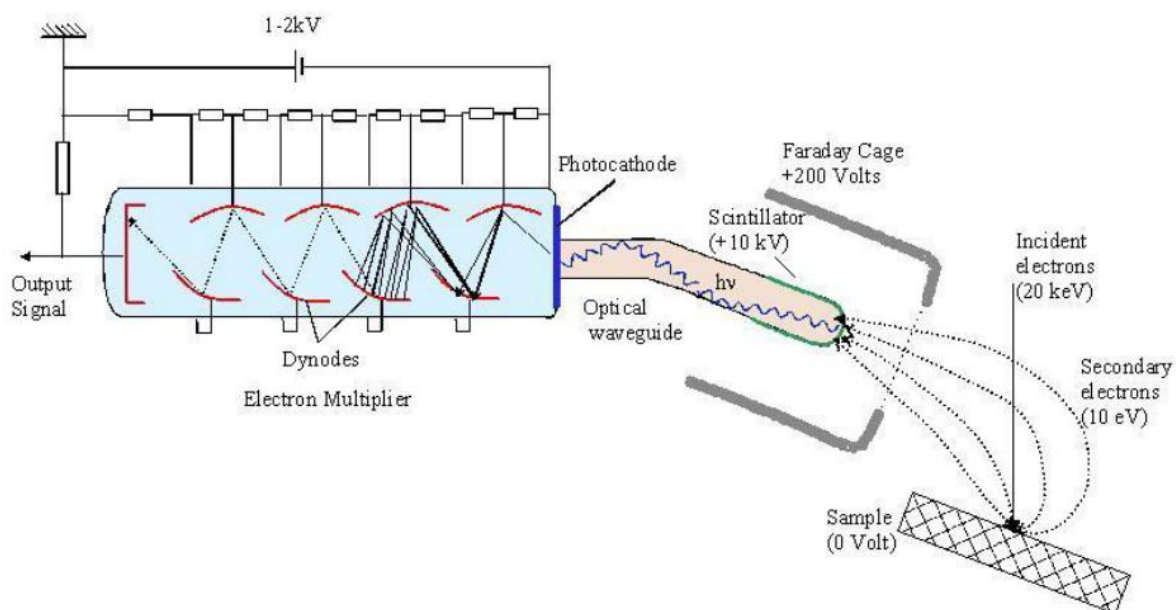


**Figure 16:** schematic cross section of an Everhart-Thornley detector (ETD), electrons are either attracted or deflected towards a / away from a Faraday Cage, depending on the applied bias. Attracted electrons are then bundled on a scintillator, where photons proportional to the number of electrons are generated. This signal is then amplified by a photomultiplier<sup>38</sup>.

### 3.4 Patterning and Image Formation

Patterning is the particular way a beam is operated, whether for imaging or beam induced processing. In the easiest case, as shown in Figure 17 the pattern is a square and the focused beam will start to irradiate the first point of the pattern, for a particular time, the dwell time (DT). After irradiation of one point the beam will move on to the next point, the distance to the next point is

denoted as the point pitch (**PoP**). This way the beam scans the first line, at which the direction is denoted as the fast scan axis, then move on to process the next line. The direction the lines are processed after another is denoted as the slow scan axis. Scanning each line from the same side to the other is known as raster scanning, while alternate scanning directions from line to line, is known as serpentine scanning (Figure 17). By detecting the signal at each point it is then possible to generate an image. Furthermore, we can define the loop time, which is the time span the beam needs to go once through the whole pattern, thus has irradiated each pixel once.

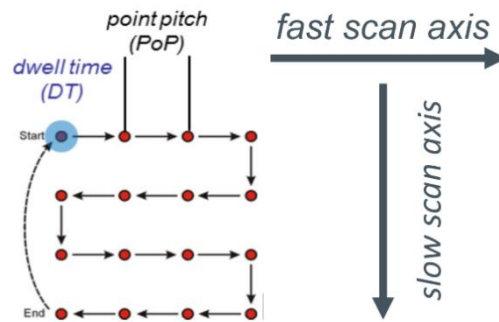


**Figure 17:** basic patterning of a square, consisting of 4 X 4 pixels. Irradiation of the pattern is done by serpentine scanning, as the scan direction changes from line to line. The time the beam stays at a certain spot is denoted as the dwell time (DT), the distance between neighboring pixels as the point pitch (PoP)<sup>10 (modified)</sup>.

Besides the patterning of easy shapes, such as rectangles, lines or circles one can specifically define the points and their respective DT the beam should irradiate using a stream file. Generally, this is a list of each points DT and pixel coordinates, at which the sequence of the points also determines the sequence of the points to be patterned. Since the total number of pixels for each magnification is the same, one has to be aware of using the right magnification while loading a stream file into the patterning engine of the microscope to obtain the desired dimensions and PoP.

## 3.5 Focused Electron Beam Induced Processing

### 3.5.1 Basics

Besides the capability to make images and to obtain site-specific analytical information of the sample, the electron beam can be used to modify the surface, called Focused Electron Beam Induced Processing (**FEBIP**). For this purpose, one makes use of a precursor gas, which is either present as an ambient gas in the chamber or directed via a gas injection system (**GIS**) towards a particular area on the surface of the sample<sup>26</sup>. Depending on the precursor gas it is possible to deposit magnetic<sup>39</sup>, conducting<sup>40</sup> and insulating<sup>41</sup> structures, do local etching<sup>28</sup>, a combination of the former two<sup>42</sup> or to

functionalize the surface<sup>43</sup>. In the following, a detailed description about Focused Electron Beam Induced Deposition (**FEBID**) of Pt is given, sketched in Figure 18 (a). The used precursor gas is trimethyl(methylcyclopentadienyl)platinum<sup>IV</sup>, shown in (b), in all discussions from now on it is either referred to as the Pt precursor or the precursor. At first, the precursor molecules are delivered by a nozzle towards the surface (1), where they can, defined by the sticking probability, physisorb (2). On the surface molecules can diffuse (3) and will after a certain time thermally desorb (4) again, characterized by the diffusion length and the mean residence time, respectively. For the used precursor on a Si substrate, these values are in the order of 25 nm<sup>44</sup> and 29  $\mu$ s<sup>45</sup>. If the precursor molecules are then in the vicinity of the beam, decomposition of the precursor can occur and parts of it will remain permanently adsorbed on the surface as a deposit (5). The actual deposition mechanism, however, is far away from being as simple as that and therefore discussed more in detail.

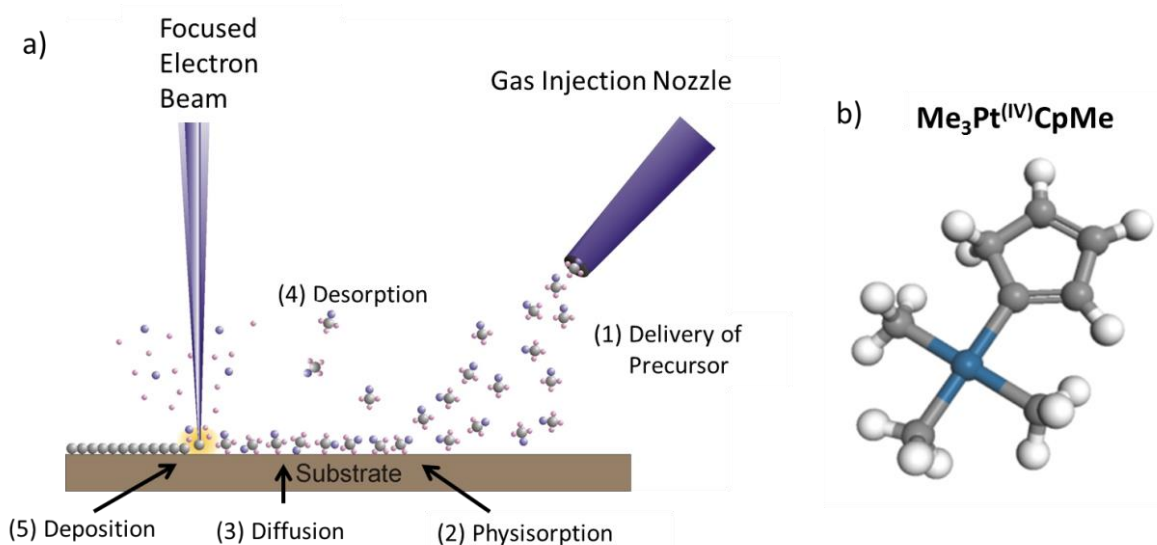


**Figure 18:** (a) during FEBID precursor molecules, such as  $\text{Me}_3\text{PtCpMe}$  (shown in (b)), will (1) be delivered to the surface, where they can (2) physisorb. On the surface, these molecules are able to (3) diffuse, after a certain time they might (4) desorb again into the vacuum. As long as they are on the surface they might, however, go (5) through certain dissociation processes and remain on the substrate as a deposit<sup>10</sup>.

### 3.5.2 The Adsorption Rate Model

The abovementioned steps are in sequential order for a single precursor molecule, but not for an entire gas flux as is normally the case during processing, for which these mechanisms happen side by side for a multitude of precursor molecules. One way to describe the precursor coverage on the surface during FEBIP is given by the adsorption rate model<sup>26,46,47</sup> (Equation 6), describing the change of precursor molecule coverage on the surface  $\frac{\partial n}{\partial t}$  as the interplay between adsorption (1), diffusion

(2), desorption (3) and decomposition (4). This model can describe in combination with the vertical growth rate<sup>26,48</sup> (Equation 7), the main outcomes during FEBIP.

$$\frac{\partial n}{\partial t} = sJ \left(1 - \frac{n}{n_0}\right) + D \left(\frac{\partial^2 n}{\partial r^2} + \frac{\partial n}{r \partial r}\right) - \frac{n}{\tau} - \sigma f n \quad \text{Equation 6}$$

$$R(r) = Vn(r) \int_0^{E_0} \sigma(E) f(r, E) dE \quad \text{Equation 7}$$

In detail, the replenishment of fresh precursor molecules directly through the gas flux depends on the sticking probability  $s$ , the gas flux  $J$ , and the number of free adsorption sites, at which  $n_0$  denotes the number of molecules for a complete monolayer. Replenishment by diffusion is described by the diffusion coefficient  $D$  and the concentration gradient. Thermal desorption is considered by the indirect proportionality to the mean residence time  $\tau$ . Last but not least, decomposition of the precursor is taken into account as the product of the beam distribution  $f(r, E)$  and the energy dependent dissociation cross section  $\sigma(E)$ . Other effects such as electron-stimulated desorption<sup>49</sup> and thermal assisted decomposition, which has been shown to play an important role at elevated substrate temperatures<sup>47,50</sup> are not taken into account as they are not of significance in the following discussion. The vertical growth rate is given as the product of the volume of the decomposed molecule  $V$ , the number of adsorbed molecules  $n$  and the integral over energy of the energy dependent dissociation cross section and the beam flux profile.

In the end, both equations are coupled by the decomposition, which consumes precursor and gives rise to a deposit, hence by understanding the given equations one can gain deep insights of the deposition process, as a function of available precursor molecules and dissociating electrons, i.e. PE, SE, and BSE. However, it should be emphasized that the dissociation cross section is energy dependent and has a maximum at about 150 eV<sup>51</sup>. Yet, SE give the biggest contribution to the energy spectrum with a maximum at a few eV, and are therefore mostly responsible for precursor decomposition<sup>52</sup>. Furthermore, the dissociation process of a ligand complex will not be completed within a single electron reaction but requires several subsequent reactions. In addition, for the particular case of  $\text{Me}_3\text{Pt}^{\text{IV}}\text{CpMe}$  a preferential cleavage of the Pt-Me bonds occurs<sup>53</sup>, and in fact decomposition of the precursor will not be complete, hence deposits will always include a certain carbon content, which ranges depending on the processing parameters between 70 at.% and 90 at.%<sup>54</sup>. Moreover, the deposited material will have a peculiar inner structure, as shown in Figure 19 (a), one can see that after deposition crystalline Pt grains (black) have formed with a diameter in the range of 2 - 3 nm<sup>55</sup>, which are embedded in a carbonaceous matrix (gray). The distance between neighboring Pt grains depends strongly on the process parameters. In order to explain this phenomenon, we look back at the above-described model, from which two important regimes emerge in the extreme case, i.e. the electron limited regime (**ELR**) and the molecule limited regime (**MLR**). Former is characterized by an excess of precursor molecules and a limited amount of electrons, therefore dissociation will be incomplete, leading to a high incorporation of unwanted precursor fragments, i.e. Me and Cp Ligands<sup>54</sup>. However, for the vice versa case in the MTL a high degree of dissociation is achieved at first, but the excess of dissociating particles will then initiate polymerization of precursor fragments, which in turn leads again to a high carbon incorporation. Thus, one might assume that in the intermediary regime, i.e. to balance dissociating particles and precursor molecules should result in a low carbon content. Indeed this has been observed by Plank et al.<sup>54</sup>, but with the big disadvantage that during growth the processing parameters would have to be constantly adapted, which becomes evident for the deposition of a single pillar, for which one can

observe different Pt to C ratios with increasing height of the pillar, as depicted in Figure 19 (b). This problem arises, due to a change of the surface diffusion mechanism, which in the beginning is dominated by diffusion from the surrounding substrate. With increasing height the necessary diffusion path for precursor molecules from the substrate increases, therefore it becomes more and more probable that these molecules will desorb before they can reach the irradiated area<sup>44,54,56</sup>. In this case, precursor replenishment by diffusion is governed by those molecules, which adsorbed on the deposit surface before, which however constitutes a much smaller reservoir of precursor molecules. During the whole process, direct replenishment from the gas phase is assumed to be constant but becomes due to the decrease of substrate related replenishment, relatively more important.

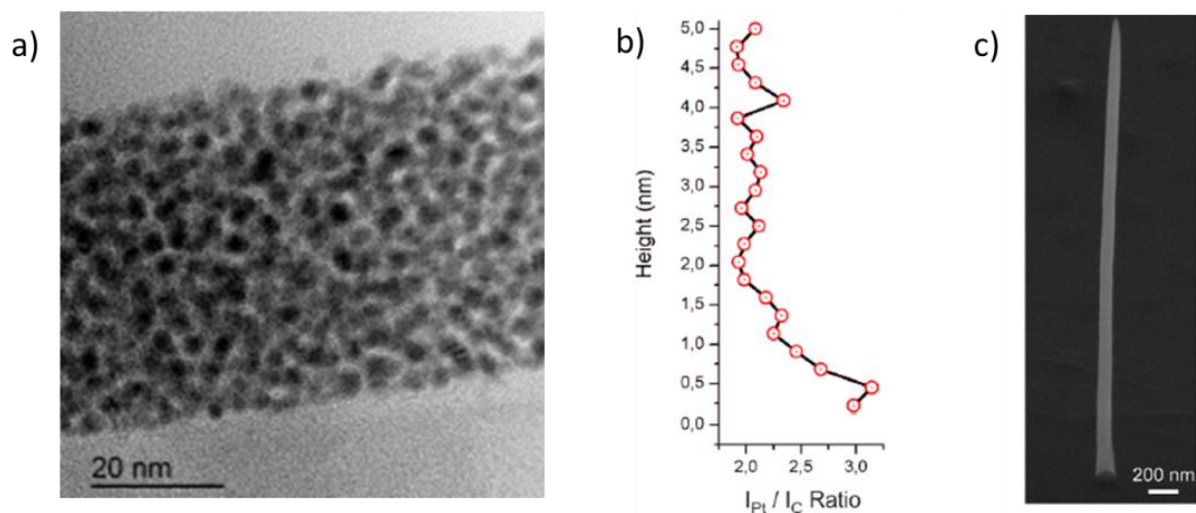


**Figure 19:** (a) TEM image of the inner structure of a deposition from the considered precursor showing Pt grains (black), 2 – 3 nm in size, embedded in a carbonaceous matrix (gray)<sup>55</sup>. (b) during deposition with constant parameters, a regime shift is observed, which becomes evident by shifting Pt to C ratios as observed for the growth of a single pillar(c)<sup>54</sup>.

### 3.5.3 3 Dimensional Nanofabrication

The above-described situation was for a long time the reason that the fabrication of desired 3D nanostructures was more a trial and error than a predictable process, as regime changes during processing are basically unavoidable. However, thanks to the works by Winkler and Fowlkes et. al.<sup>44,56,57</sup> it was possible to turn this situation from trial and error to design desired 3D structures within a CAD software, which will then compute the necessary stream file. Beforehand the software is calibrated to fit the experimental setup, which depends on the used precursor, the nozzle alignment, the beam energy and beam current. Determination is done by FEBID of diving board structures or iteratively adapting the calibration parameter until the CAD is equivalent to the fabricated structure. This parameter is entered in field (1) in the user interface of the software,

Figure 20. In field (2) the vertices of the structure are entered, whose exact position can be determined by coordinates in field (3). A connection between 2 particular vertices is realized by entering the indices of the 2 points in field (4) and pressing *Submit*. Finally, by pressing *Build CAD* (5) a stream file is generated, which includes the coordinates (in units of length) and necessary DTs of the patterning points in the optimized order. Afterward the coordinates of the generated stream file are transferred into pixel coordinates.

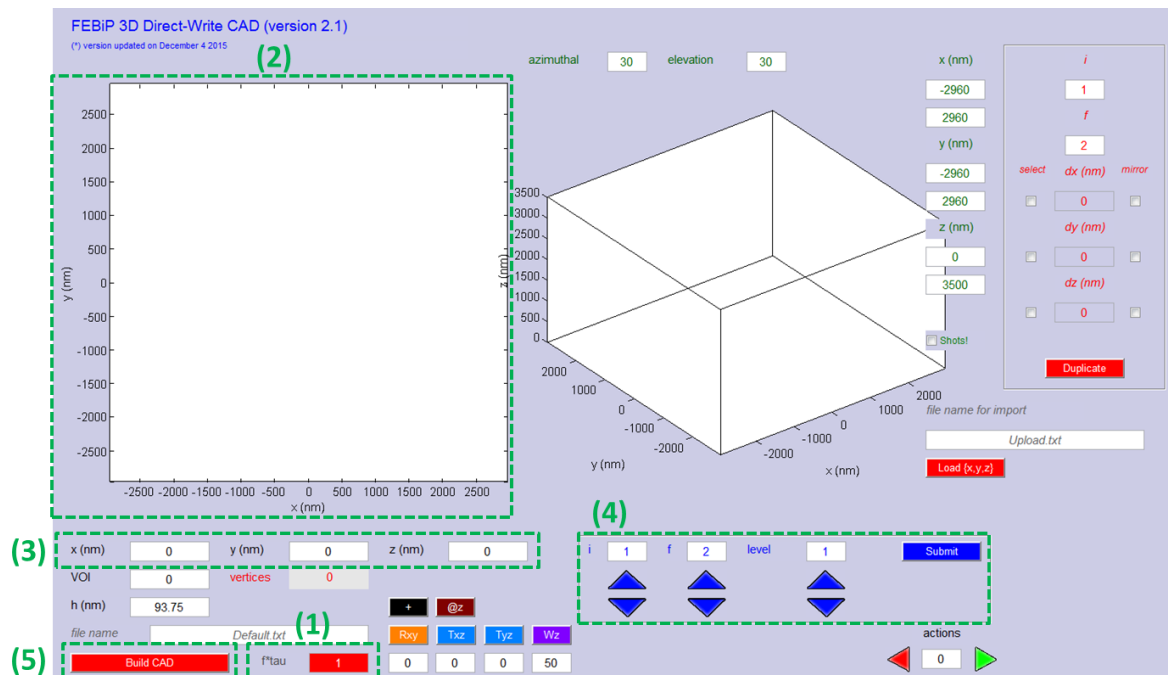


**Figure 20:** the CAD software used to design freestanding 3D nanostructures. The most important steps in the design are framed by green dashed lines, i.e. (1) input of the calibration parameter, (2) input of the vertices (3) exact definition of the vertices by metric coordinates (4) creation of links between particular vertices and (5) submitting the constructed design.

### 3.5.4 Post-Deposition Treatment

As mentioned before, the deposited structures from the Pt precursor have a high content of carbon and different approaches during processing, without involving another precursor species, haven't resulted in pure Pt. However intense research by Porrati et al.<sup>58</sup> and Plank et al.<sup>59</sup> revealed that it is possible to modify the as-deposited structure by irradiation with an electron beam, called e-beam curing. Incompletely and non-dissociated precursor molecules are further dissociated during this process, which leads to the formation of new Pt grains and as well to the growth of already existing ones<sup>59</sup>. Both effects contribute to the decrease of the distance between neighboring crystallites, and hence the physical properties of the deposit change. This effect has been shown to be much stronger

for deposition in the ELR compared to MLR since incompletely and non-dissociated precursor molecules contribute most to this particular process.

Furthermore, it was shown by Geier et al.<sup>55</sup> that it is indeed possible to obtain pure Pt structures with a post-deposition treatment, i.e. a purification treatment. This is done by irradiation with an electron beam in ambient H<sub>2</sub>O atmosphere within an environmental SEM. During processing it is assumed that H<sub>2</sub>O diffuses into the deposit, where it is dissociated in atomic H and O due to SE, which thereafter binds to C atoms, becomes volatile and subsequently can gas out.

### 3.5.5 Physical Properties of Deposits

Due to their special composition and inner structure the physical properties of deposits are far off from those of their respective bulk materials. This opens the door to new applications, such as environmental gas sensors<sup>23,60</sup>. These possible applications, due to the special physical properties stem from the inner structure of the Pt-C deposit, where crystalline Pt grains are embedded in a carbonaceous matrix. Since this thesis is part of a project to develop a nanoprobe for thermal sensing applications the properties regarding conductivity, mechanical behavior and thermal properties, and their specific interplay have to be taken into account.

Electrical conductivity is described for as-deposited structures and shortly to intermediate cured deposits by correlated variable range hopping, for higher degrees of curing metallic behavior is observed<sup>58,61</sup>. Overall an increase in conductivity with decreasing space between neighboring grains is observed. Conductance in deposits described by variable range hopping encounter an exponential increase in conductivity with increasing temperature, while for highly cured deposits with metallic conductivity a decrease with temperature is observed. Furthermore, it has been shown by Schwalb et al. that Pt-C structures can be utilized as strain sensors<sup>62</sup>. This in particular, has to be considered in this work, as the nanoprobe will receive some degree of deformation, hence a non-thermal related change in resistance of the probe is expected to occur.

It has been shown by Georg Arnold<sup>23</sup> that the mechanical properties also strongly depend on the degree of curing, thus Young's modulus is tunable within a range from about 10 GPa (uncured) up to 70 GPa (fully cured). In particular, he found out that the mechanical properties of as-deposited structures are primarily determined by the surrounding carbonaceous matrix, which resembles in this state the structures of disordered nano-tubes (10 GPa) and polyhedral graphite particles (12.8 GPa). The increase, however, is regarded mainly to the change of grain size and intergranular distance, since for fully cured structures higher moduli were observed as suggested by literature for the carbonaceous matrix, which undergoes a partial transformation into a graphite crystal structure (36 GPa).

### 3.6 Instrumentation

The used DBM is an FEI Nova 200, equipped with 5 GIS; for deposition: Pt, Au, and SiO<sub>2</sub>, for etching: I<sub>2</sub>, and XeF<sub>2</sub>. The base pressure in the chamber during imaging and force spectroscopy was typically in the range of about  $(5 - 7) 10^{-6}$  mbar. Before deposition the GIS was turned on until a steady state pressure was reached, which was in the range between  $(0.9 - 1.3) 10^{-5}$  mbar. The Pt reservoir was heated to 45 °C at least for an hour prior to deposition. The GIS alignment can be seen in Figure 21. The nozzle is built into the chamber with 38° with respect to the sample, the distance above the surface is about 110 μm. The position of the electron beam center relative to the nozzle apex is at 50 μm, perpendicular to the nozzle main axis (X) and 520 μm, in the direction of the nozzle main axis (Y). Before all depositions test spots were deposited with a TET of 5 s to get an estimation of the quality of beam focus and astigmatism correction.

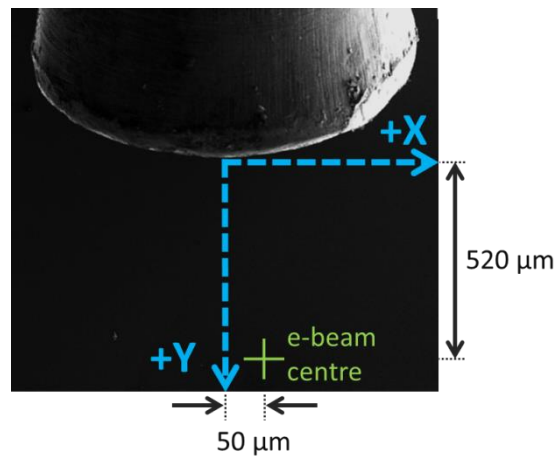


**Figure 21:** the GIS alignment relative to the e-beam center (green cross), also indicated are the GIS main axis (+Y) and the direction perpendicular to the main axis (+X).

## 4 Simulations

This thesis focuses on the mechanical properties of 3D structures, for which the aim is to explain the underlying physics of certain observed effects in order to build reliable and reproducible free-standing 3D nanostructures, which can be utilized for practical applications. The architecture, its dimensions, and certain design features altogether build up a multidimensional parameter space, thus approaching this problem only by an experimental study would, on the one hand take time excessive experimental series, on the other hand special structural features cannot be isolated or eliminated in experiments, thus one will always observe a convolution of several mechanisms. To avoid both these problems targeted experiments were performed in combination with simulations and in an iterative process, an explanation on the most important qualitative and quantitative mechanical properties is found. The simulations done were Finite Element Simulations, for which a short theoretical introduction is given below, which is compared to an analytical solution of the simplified problem beforehand to better understand the relation between the parameters and the resulting properties.

### 4.1 Finite Element Method

Many problems in physics are given as Partial Differential Equations (**PDE**), like the Euler-Bernoulli beam equation or the heat equation. For systems with a high degree of complexity, i.e. when the geometry or boundary conditions of the investigated domain get complicated, a straightforward analytical solution of these PDEs is hard to impossible to find. One approach to overcome this problem is the Finite Element Method (**FEM**), at which the geometry is subdivided into smaller regions (finite elements) and the PDEs in each element are approximated by algebraic or ordinary differential equations, which can be solved more easily. Besides the advantage that complex geometries can be more easily represented, it is also far easier to include non-homogeneous material properties, e.g. space dependent Young's Modulus. The value of this particular property will simply stay the same within one element and change somehow for the neighboring elements. Another advantage is to capture local effects, therefore it is easy to see how certain parts of the investigated domain will behave under certain conditions. A much more sophisticated introduction to FEM simulations and its applications can be found in various books<sup>63,64</sup>.

Besides these advantages one has to be aware what exactly is happening in the simulation, therefore results should be reviewed very critically, as they depend strongly on the boundary conditions, the discretization of the problem and the setting of the analysis itself, i.e. solver, convergence, number of iterations and others. Therefore a short overview of the most important factors is given in the following subsections with regard to the used FEM Software package, COMSOL Multiphysics 4.3<sup>65,66</sup>.

### 4.1.1 Mesh

The geometries of the investigated structures were built using the internal Computer Aided Design (**CAD**) module of COMSOL. Within the structure of each domain all internal boundaries were turned off, thus structures consisting of several elements would be fully unified. After designing the geometry, its body is meshed, thus dividing the whole domain into smaller sub-regions. For all simulations the shape of the sub-elements chosen would have the form of a tetrahedral. Other possibilities are bricks, prisms, and pyramids. Compared to the other possibilities, tetrahedrals are made in such a way that they are built with an aspect ratio close to unity, while this is not the case for other element forms, which can result in lower computational cost by making the element size bigger in directions where no significant influence is expected. However, for the here investigated structures we cannot assume that certain directions might be less important for the results. Furthermore, a major advantage of tetrahedrals is that almost any geometry can be assembled by such, which is of high importance for the here discussed architectures.

More important than the element type is the meshing size, i.e. the size of the sub-elements relative to the model. The automatic meshing option gives in total 9 adjustment options ranging from *Extremely fine* to *Extremely coarse*. While a finer mesh would give a result, better representing the real situation, it would also take a much longer time of computation. Before investigations on each particular architecture, an investigation was done on how much the result changes if the mesh size would be decreased one further step, as shown in the example for the stiffness of a single pillar in Figure 22. On the abscissa is the meshing options ranging from *extra coarse* to *extremely fine*, the black curve (left axis) represents the stiffness relative to the value at *extremely fine*, the red curve represents the total computation time (right axis). Furthermore, for each meshing option an exemplary meshed volume is shown below, which immediately points out that geometries with a meshing coarser than *normal* are not suited for such investigation, as in such case the cylindrical shape of the pillar is not considered, which consecutively explains the huge difference in relative values around these meshing sizes. Also, it can be seen in this figure that in general decreasing the mesh in the range from *normal* to *extremely fine* would change the result by less than 0.001 %, while the computational time would increase from 1 s to 120 s (Intel Core i5 3.5 GHz Quadcore, 16 GB RAM). In most cases the meshing was set to *finer*, which gave a reliable result at a moderate computational time.

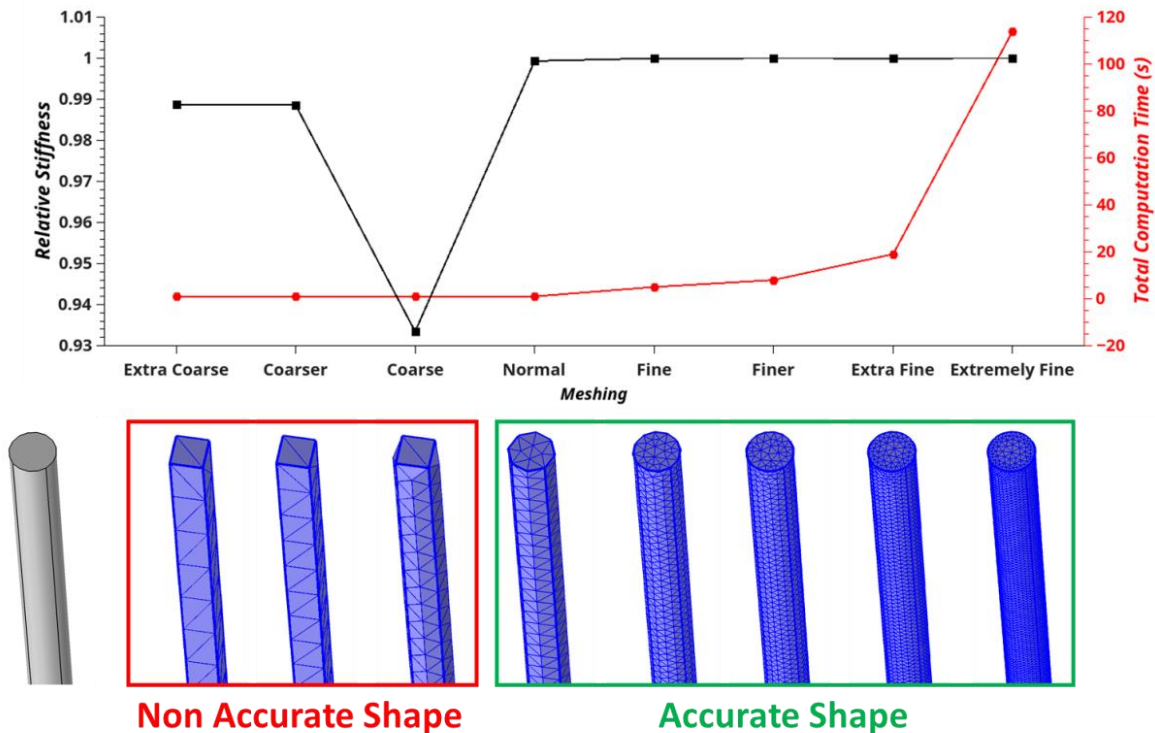


**Figure 22:** the relative stiffness (black curve / left axis) and the total computation time (red curve / right axis) as function of the meshing size. The modeled geometry is shown at the bottom left, below each meshing step the respective geometry is shown. Meshing below normal results in this case in non-accurate shapes and therefore in general dismissed.

#### 4.1.2 Equations and Solver

The simulations regarding the stiffness were conducted using the *Structural Mechanics Branch* of COMSOL. It was chosen to be a *stationary study*, as there are no time dependent parameters present in the comparable investigations on real structures. In this formulation of the problem time derivatives in the underlying equations become zero, thus simplifying the problem and therefore less computation is needed. The underlying equations are based on the principle of virtual work, which sets the external load equal to the work from internal stresses<sup>66</sup>.

#### 4.1.3 Accuracy and Convergence

Of course, the results obtained from such models will be not representing the exact reality. This stems from several factors. First of all, the structures are divided into smaller elements, hence for an exact representation of the real behavior these elements should be infinitesimally small. Although one can see that with decreasing element size the investigated properties converge as shown before in Figure 22, they will still differ by a small amount from reality.

The used solver works iteratively, thus starting with an initial guess to get a first result, which is then improved by each iteration step. Iterations are repeated until the convergence criterion is reached, i.e. when the relative tolerance becomes smaller than a given threshold or the absolute tolerance becomes smaller than a model size dependent value. The latter is the absolute difference of the investigated value between two iterations steps, therefore it is model size dependent and an exact value cannot be given. In general, the better convergence criterion is the relative tolerance, which is the absolute difference relative to the value of the last iteration step and therefore, not model size dependent, at which a value of 0.01 rel. % does account for all simulations, independent on the model size. For mechanical simulations, the absolute difference refers to the total amount of work performed by the system.

Finally and most important of all it should be kept in mind that the modelled structures are of course highly simplified, i.e. no consideration of the microstructure, rippled surface features, constant diameter of the pillars, not including the surrounding environment, and all models are assumed to have a totally fixed connection to the substrate, thus the stress is not transferred to the underlying surface. Such a simplification is on the one hand necessary to avoid extended computation times, on the other hand this opens the possibility to investigate the impact particular features in a simulation will have, as done in this thesis.

## 5 Analysis of Mechanical Properties

Among the major requirements for the fabricated probes is that their stiffness in the direction perpendicular (axial) to its base should be higher than the stiffness of the cantilever, thus the cantilever itself will bend more than the respective nanostructure, as compared in Figure 23. Besides that, the stiffness in other directions should have a certain minimum value in order to avoid undesired lateral bending of the probe itself, which would lead to falsification of measurements and a loss in imaging resolution. In order to find a suitable geometry, several sweeps of its parameters changing the architecture and dimensions of the probe were conducted. However, in order to fully understand the problem and to get a feeling for the intrinsic relations our investigations start with a look at the analytical solution for a single pillar.

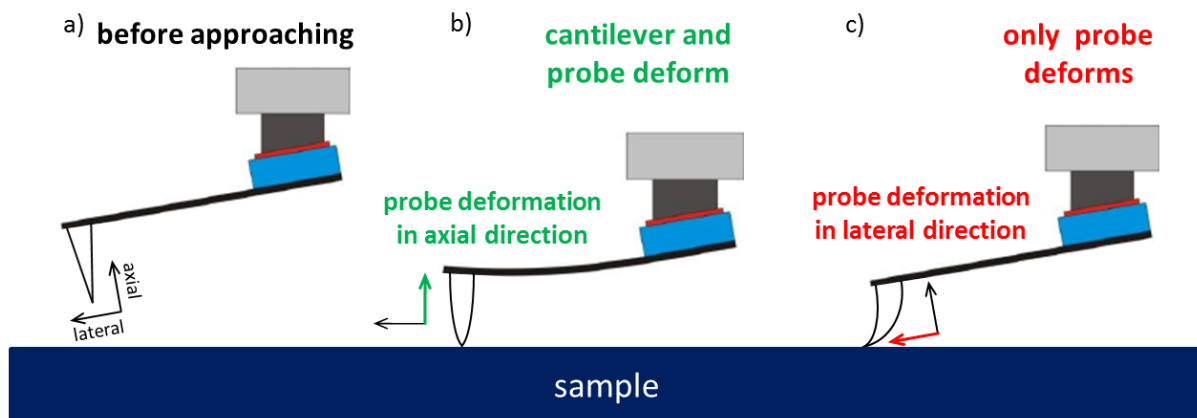


**Figure 23:** (a) the undeformed probe on the cantilever before approaching. (b) in the ideal case of an approached cantilever, its deflection will be stronger than that of the nanoprobe, therefore reliably measurable, furthermore, the probe deformation occurs in axial direction. (c) in the worst case only the probe instead of the cantilever deforms, as well deformation of the probe in lateral instead of the preferred axial direction occurs.

### 5.1 The Underlying Model

#### 5.1.1 Analytical Solution of a Single Pillar

The geometry and the considered displacement cases are depicted in Figure 24, the pillars geometry and mechanical properties are defined by its height  $H$ , diameter  $D$  and Young's modulus  $E$ . In the following discussions the vector perpendicular to the base of the respective structure going through the apex is referred to as the axial direction, while the plane perpendicular to this axis and at the apex of the pillar is referred to as the radial plane, while arbitrary vectors in this plane are referred to as radial directions. In case of a force acting in radial direction  $F_r$  a displacement  $u_r$  in this direction will occur, while an axial Force  $F_a$  will result in an axial displacement  $u_a$ . The magnitude of the

displacement at the top of the pillar for each case can be calculated via Equation 8 and Equation 9, thereupon it is possible to calculate the stiffness in each case with Equation 10. From these equations one can already see that lesser heights as well bigger diameters of the pillar will lead to smaller deflections at the same force, thus in total a higher stiffness. Exemplary for our model a cylinder with a length  $L=5 \mu\text{m}$ , a diameter  $d=50 \text{ nm}$  and a Young's Modulus  $E=14 \text{ GPa}^{23}$ , one will obtain values of  $k_r=1.03 \cdot 10^{-4} \text{ N/m}$  and  $k_a=5.5 \text{ N/m}$ , for the radial and axial case, respectively. One can already see that there is a huge difference between the stiffness in radial and axial direction of about 4 orders of magnitude.

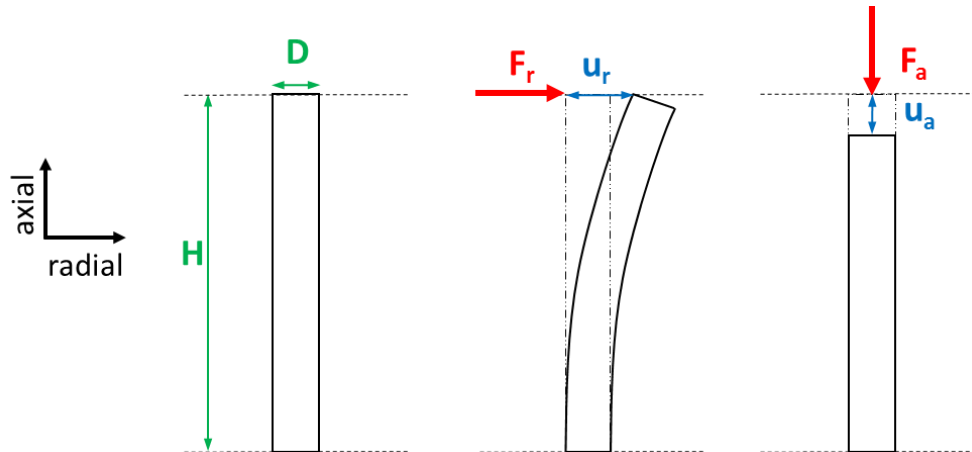


**Figure 24:** the geometry of a single pillar, characterized by its diameter  $D$  and height  $H$ . Under radial and axial force  $F_r$  and  $F_a$  the single pillar will be deflected to a certain extent,  $u_r$  and  $u_a$  according to Equations 9 and 8, respectively.

$$u_a = \frac{4 F_a H}{\pi d^2 E} \quad \text{Equation 8}$$

$$u_r = \frac{64 F_r H^3}{3\pi d^4 E} \quad \text{Equation 9}$$

$$k_i = \frac{F_i}{u_i} \quad \text{Equation 10}$$

### 5.1.2 Pre-investigations

The first simulations were not dealing with the geometry but were conducted to understand the influence of a yet unknown material property, Poisson's ratio  $\nu$ , the ratio between transversal and axial strain, for stress in the axial direction. In general, assuming a cube, at which a stress is applied on its top surface compressing it in the direction perpendicular to this surface one will observe a decrease of the dimension of the cube in this direction, described by the axial strain, i.e. the change of length relative to the original length. At the same time, one will (in most cases) observe an increase of the transversal dimension of the cube, described by the transversal strain. This

investigation was necessary as there is little to no information available about this mechanical property for nanocrystalline systems, especially for the here investigated material, nanocrystalline Pt in an aC matrix. From literature we only know about the values for pure platinum, diamond carbon, graphite and amorphous carbon, which are listed in Table 1.

Table 1: Literature values for materials which are chemically comparable to our investigated material.

Material	Poisson's ratio $\nu$
Platinum	0.39 <sup>67</sup>
Diamond	0.18 – 0.22 <sup>68</sup>
Graphite	0.17 – 0.23 <sup>69</sup>
Amorphous Carbon	0.12 -0.17 <sup>70</sup>

Since there are too many factors influencing the value of Poisson's ratio, a short investigation was conducted on how much this parameter would influence the stiffness of a pillar. For this investigation the geometry was set to a height of 5  $\mu\text{m}$ , a diameter of 50 nm and Young's modulus of 14 GPa. The variation is shown in Figure 25 together with the analytical solution (black curve) for the case of radial (a) and axial (b) displacement. For both cases a superlinear increase of the stiffness (blue curve / left axis) with  $\nu$  is observed. However, relative to the stiffness at  $\nu=0$  (red curve / right axis) one can see that only close to  $\nu=0.5$ , the highest possible value for Poisson's ratio, the radial stiffness exceeds an increase of 1% and 0.1% for the axial stiffness. The overall negligible influence of  $\nu$  stems from the high aspect ratio (**AR**) of the geometry, which implies that a volume change in the axial direction will result in an almost negligible volume change in radial direction.

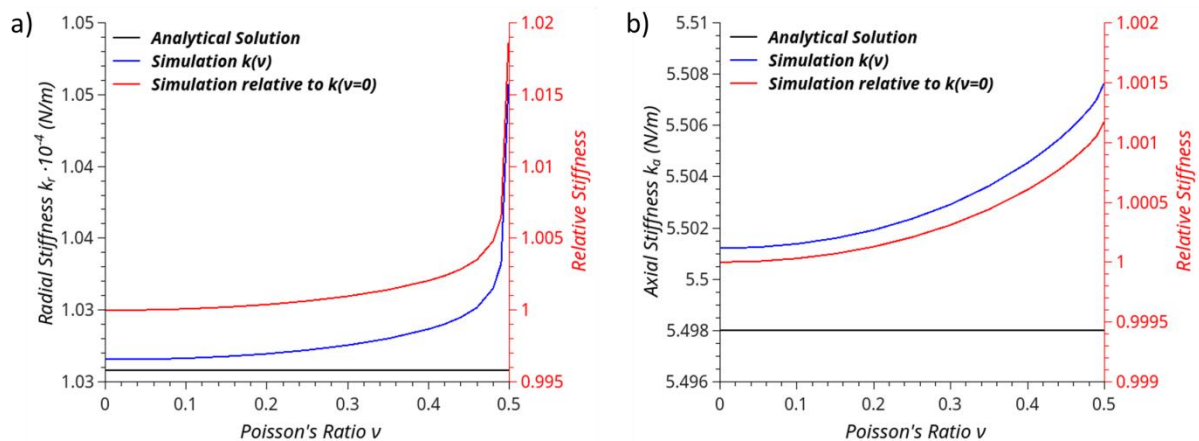


Figure 25: dependence of the absolute stiffness (blue curves/ left axis), the relative stiffness (red curves/ right axis) and the analytical solution (black line) for a variation of Poisson's ratio in radial (a) and axial (b) direction.

Although, the exact value of Poisson's ratio is unknown, the results point out that for the considered high AR geometries an experimental determination is not necessary to obtain reliable results from the corresponding simulations. Based on the outcome in this section  $\nu$  was set to a value of 0.2 in all further investigations. At the one hand, this is justified since this value is in the range of similar

systems (aC or graphite) according to literature. On the other hand, only values close to 0.5, as for rubber materials, would result in changes larger than 1 %.

### 5.1.3 Simulations – Single Pillar

Although it was clear from the beginning that the single pillar architecture would not be suitable for our purpose, it represents a good starting point for our simulations, as the results can be compared to analytical solutions and from that the problem can be mapped onto more complicated structures with higher degrees of complexity, e.g. more branches, bending in mixed directions or inhomogeneous morphological properties.

The radial and axial stiffness was investigated using the same material parameters as mentioned before, for a variation of the height and diameter in ranges from 1  $\mu\text{m}$  – 5  $\mu\text{m}$  and 20 nm – 100 nm, respectively. Results are depicted in Figure 26 (a) and (b) for radial and axial stiffness. One can see that in general the radial and axial stiffness increases strongly as the height is decreased and the diameter is increased, showing the highest value in the investigated ranges at  $H=1 \mu\text{m}$ ,  $D=100 \text{ nm}$ . As seen before, the axial stiffness is much higher than compared to the radial stiffness. Qualitatively and quantitatively, the higher stiffness with bigger diameter and smaller height is in both cases in accordance with analytical calculations, as pointed out by a relative comparison between simulated behavior and analytical values, shown in Figure 27. From this relative comparison one can see that in both cases stiffness deviations of the simulated from the analytical value are smaller than **1%**. At which for the axial stiffness (b) one can see a stronger deviation towards smaller diameters and larger heights as well towards smaller heights and bigger diameters. While for the radial stiffness deviations from the analytical value seem to behave like a mix of 2 dimensional sinus functions. However in both cases, the relative deviation is still so small that in general it can be assumed that the simulations of single pillar deflections are reliable and a transition to more complicated structures will still give valid results.

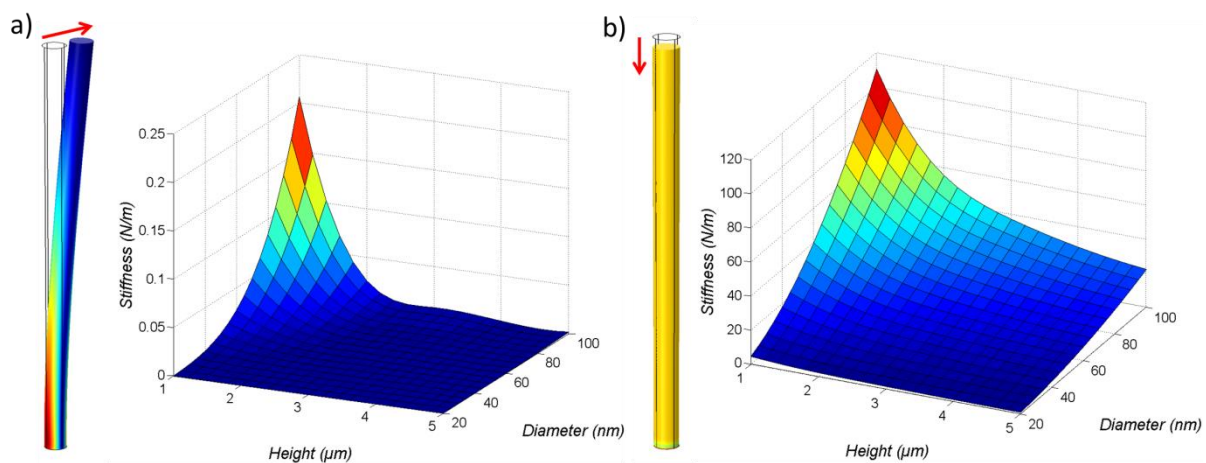


**Figure 26:** the radial (a) and axial (b) stiffness of a single pillar depending on its geometry parameters height and diameter. Next to each plot the respective deflection of the pillar geometry is shown.

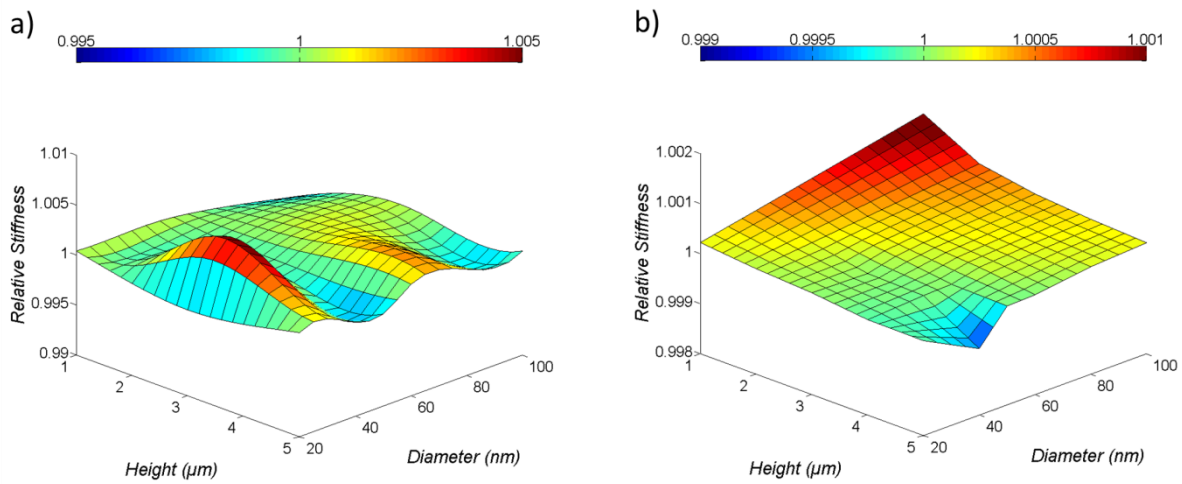


**Figure 27:** the radial (a) and axial (b) stiffness relative to the analytical value of a single pillar depending as function of its geometry parameters height and diameter.

#### 5.1.4 Bipod and Tripod

In the following investigations the architecture becomes more complex by adding further branches, such is the case for the bipod and tripod, which are made up of 2 and 3 slanted pillars, as shown in Figure 28 characterized by three parameters of geometry, i.e. the pillar height ( $H$ ), diameter ( $D$ ), and the angle relative to the ground ( $\alpha$ ). The branches of each structure are arranged virtually on a circle, which are placed  $180^\circ$  and  $120^\circ$  apart, respectively. A certain span ( $S$ ) between onset points of the individual branches arises dependent on the height  $H$  and the angle  $\alpha$ . Height, diameter, and  $\alpha$  were varied in ranges from  $1 \mu\text{m} - 5 \mu\text{m}$ ,  $40 \text{ nm} - 100 \text{ nm}$  and  $50^\circ - 85^\circ$ , respectively. Due to their non fully axial symmetric geometry in the radial plane, simulations regarding the stiffness in different directions of the radial plane were carried out. Furthermore, a few simulations were conducted on a tripod structure with a given height offset for one branch of a tripod, which represents the case of two branches connecting two electrodes, while a third branch stabilizes the structure but being deposited in the trench between these electrodes.

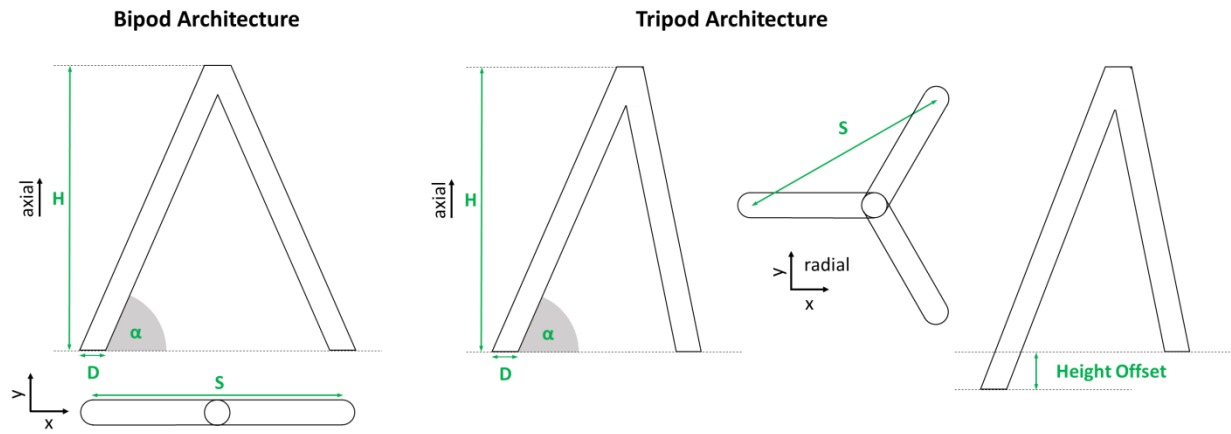


**Figure 28:** bipod and tripod architecture are defined by the parameters height ( $H$ ), diameter ( $D$ ), angle relative to ground ( $\alpha$ ) and from this follows a certain span ( $S$ ). Furthermore, the geometry of a tripod with a height offset for one of its branches is shown.

**The Axial Stiffness ( $k_a$ )** of bipod and tripod architecture (diameter of 60 nm) is shown in Figure 29 for a bipod (a) and tripod (b), at which the bottom axis represents the height  $H$  and the right axis represents the angle  $\alpha$ . Both plots have in principal the same qualitative form. One can see that the dependency on  $\alpha$  shows increasing stiffness towards larger opening angles  $\alpha$ , which seems to saturate as the angle approaches  $90^\circ$ , in fact, the stiffness approaches the double / triple value of a single pillar, which is in accordance with a fundamental understanding of such a structure, as going towards  $90^\circ$  is equivalent to the case of several parallel single pillars for which the stiffness should be equal to the number of pillars times the stiffness of one. Otherwise, the qualitative dependency on alpha seems to go with a sine function. Compared to the results for the single pillar one can see that again stiffness decreases significantly with height, in fact the dependency of the stiffness is inverse proportional to the height, as pointed out for bipods and tripods of various geometries in Figure 30 (a). In addition the dependency of the stiffness on the diameter is the same as for the single pillar, i.e. proportional to the square of it, depicted in Figure 30 (b).

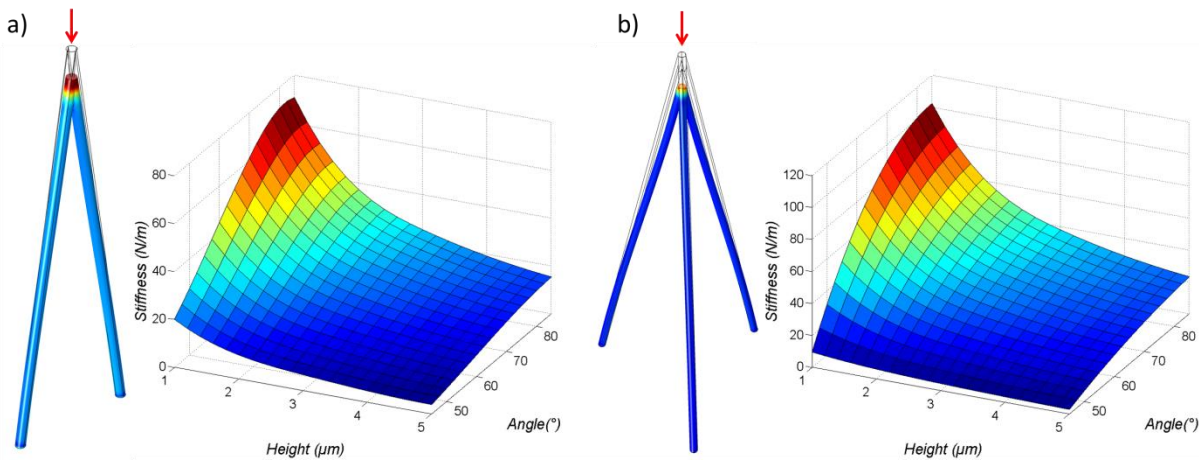


**Figure 29:** the axial stiffness of a bipod (a) and a tripod (b) as function of the height (bottom axis) and the opening angle  $\alpha$  (right axis) show, albeit their different architecture, qualitatively the same behavior. In absolute values, the tripod is however stiffer.

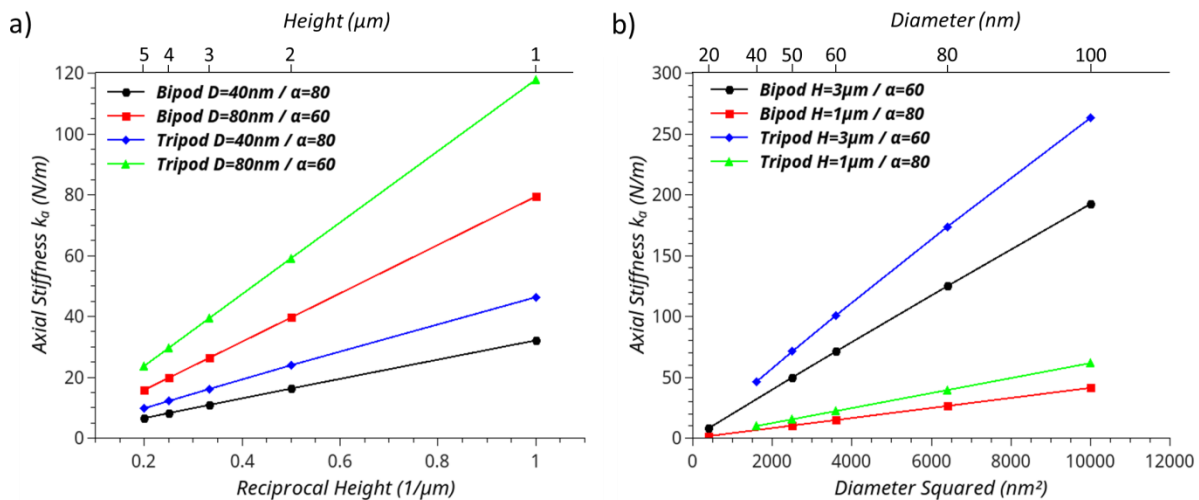


**Figure 30:** the axial stiffness as function of the reciprocal height (a) and the diameter squared (b) for different geometries of bipods and tripods show linear curves as plotted against the reciprocal height and the squared diameter, thus exhibiting the same basic dependency as the single pillar.

**The Radial Stiffness** was determined by simulations as depicted in Figure 31, introducing  $\theta$ , the angle of the applied force relative to the x-axis. The calculated stiffness as function of  $\theta$  is depicted as a polar plot for exemplary structures ( $H=2 \mu\text{m}$ ,  $\alpha=70^\circ$ ,  $D=60 \text{ nm}$ ) in Figure 32 (a), which reveals that both architectures behave quite different. The stiffness of the bipod (black curve) is clearly non-radial symmetric, while the stiffness of the tripod (red circle) has this property. Actually, the stiffness of the bipod in the given polar plot has the shape of an oval, but due to the immense decrease for already small angles of  $\theta$  cannot be seen as such. To further underline this peculiarity a semilogarithmic plot of the stiffness versus the polar angle is shown in Figure 32 (b), showing that already for an angle of  $1^\circ$  between applied force relative to the branch direction the stiffness drops one order of

magnitude. At its minimum, i.e. the direction perpendicular to the branch direction, the stiffness is about three orders of magnitude lower. The elliptic shape of stiffness in the radial plane was observed in general for all investigated geometries and therefore the stiffness of bipods can be fully described by two parameters, i.e.  $k_x$  and  $k_y$ . The quantitative values however, depend on the geometry as will be shown later.

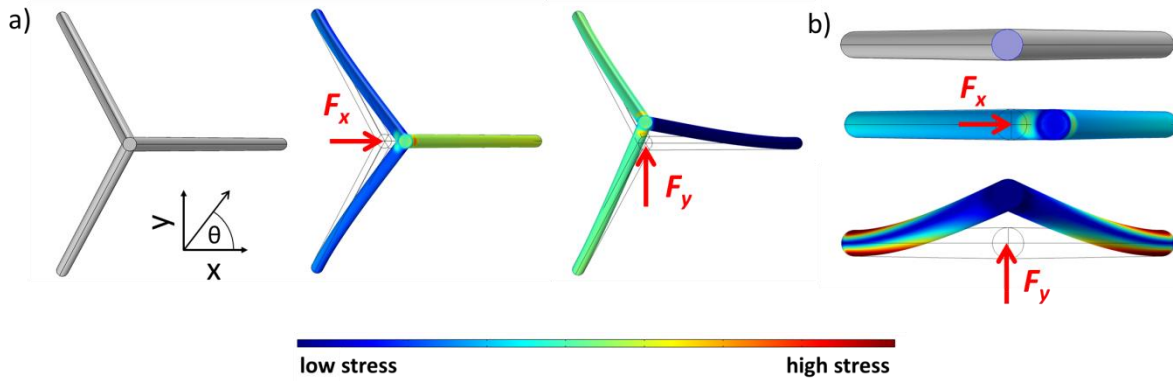


**Figure 31:** deflection of a tripod (a) and bipod (b) in the radial plane along the x and y-direction. The induced stress in the respective branches also points out that, those structures that are aligned more towards the applied force will contribute higher to the calculated stiffness.

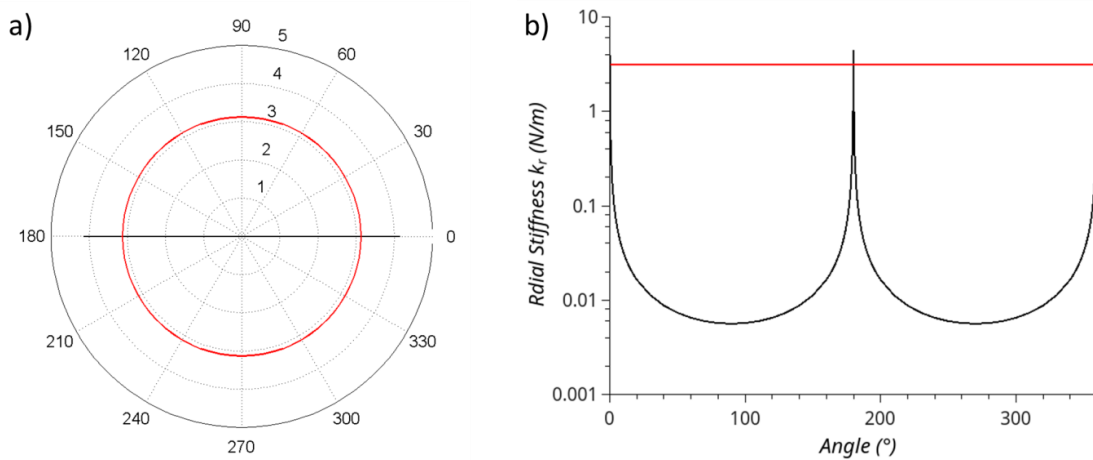


**Figure 32:** the radial stiffness of a bipod (black curve) and tripod (red curve) depicted in polar coordinates (a) and as a logarithmic plot of stiffness versus polar angle (b). Both structures have the following geometrical parameters  $H=2 \mu\text{m}$ ,  $\alpha=70^\circ$ ,  $D=60 \text{ nm}$ .

From a fundamental point of view, the result is not surprising, as Hooke’s law (Equation 2) in general is described in matrix form, Equation 11. Thus assuming a distinct force in the radial plane is acting on the apex of a structure, generally the deflection is described not only by one, but 4 stiffness constants,  $k_{xx}$  and  $k_{yy}$  relating the deflection in the direction of the applied force as well  $k_{xy}$  and  $k_{yx}$

relating the deflection in direction perpendicular to applied forces. The latter in turn become zero, for certain symmetric properties. In such a case the absolute deflection  $u$  can be related to the absolute force  $F$  by Equation 12. In the case of a bipod, assuming a force acting in the direction of one of the branches ( $x$ ), deflection in perpendicular directions can not occur, as no distinct geometrical property would induce a deflection in either direction, the same accounts for the  $y$ -direction. Hence  $k_{xy}$  and  $k_{yx}$  become zero and the bipods radial-plane stiffness is determined by two constants  $k_x$  and  $k_y$ , therefore has the shape of an oval, as shown above.

For the tripod we obtained a constant radial-plane stiffness, a circle. As before the mixed stiffness constants become zero due to symmetry along branches. Furthermore, it is obvious that due to its symmetry, this structure has to deflect the same way along each branch. This, in turn means that below equation has to give the same deflection  $u$  for a  $\theta$  of  $120^\circ$  and  $240^\circ$ , which is only possible if  $k_x$  and  $k_y$  have the same value. In general, for structures with at least three-fold axial symmetry both stiffness constants are the same.

$$\begin{pmatrix} F_x \\ F_y \\ F_z \end{pmatrix} = \begin{pmatrix} k_{xx} & k_{xy} & k_{xz} \\ k_{yx} & k_{yy} & k_{yz} \\ k_{zx} & k_{zy} & k_{zz} \end{pmatrix} \begin{pmatrix} \Delta x \\ \Delta y \\ \Delta z \end{pmatrix} \quad \text{Equation 11}$$

$$F = u \sqrt{(k_x \cos\theta)^2 + (k_y \sin\theta)^2} \quad \text{Equation 12}$$

Regarding the dependency of  $k_x$  and  $k_y$  on the geometrical parameters, one can see in Figure 33 (a) and (b) that the biggest difference in the qualitative appearance of the curves is their different dependency on  $\alpha$ . Showing that  $k_x$  increases towards smaller opening angles, while  $k_y$  shows the exact opposite behavior, it increases towards higher opening angles. This can be understood in a simple picture. While keeping other parameters the same, for smaller  $\alpha$  the branch length will effectively increase. In the direction perpendicular to the branch, the bipod can be seen as two single pillars, for which it was shown before that with increasing height the radial stiffness decreases. On the other hand looking at the bipod along the branch direction, with smaller  $\alpha$ , the deflection mechanism resembles more and more the deflection mechanism of a single pillar in axial direction. With decreasing  $\alpha$  this property increases, thus in turn the stiffness increases. Besides this dependency on  $\alpha$  it is shown in Figure 34 (a) and (b), that contrary to deflection of a single pillar in radial direction (Equation 9), the stiffness in  $x$  and  $y$ -direction are both linear with the reciprocal height and the squared diameter. Again, for the  $x$ -direction the abovementioned argument holds, that an increasing character of axial deflection determines its behavior, hence also the geometrical dependencies are mapped on the stiffness in  $x$ -direction. For the  $y$ -direction a similar effect, yet not as strong comes into play. In absolute numbers the stiffness in  $x$ -direction is overall about three orders of magnitude higher.

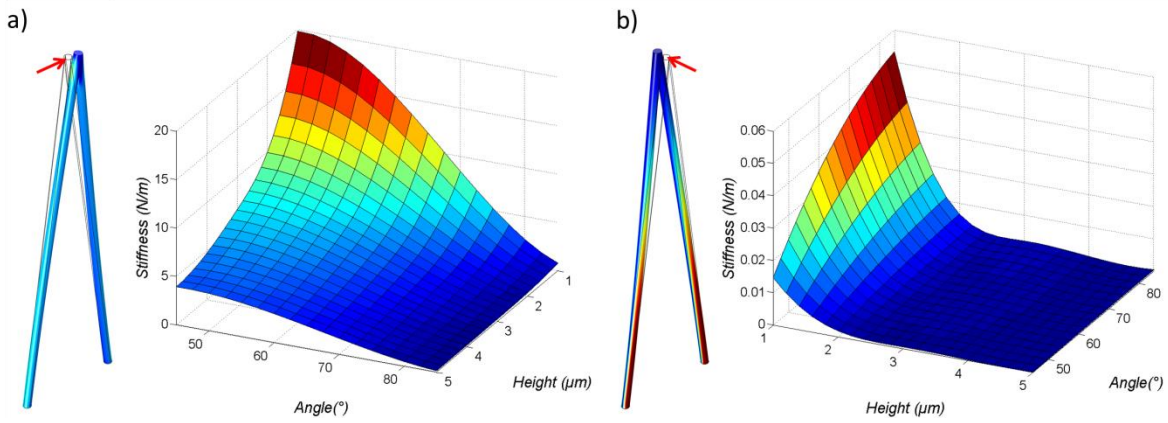


**Figure 33:** the stiffness values  $k_x$  and  $k_y$  in the radial plane of a bipod. Please note the different arrangement of the axis for better visibility.

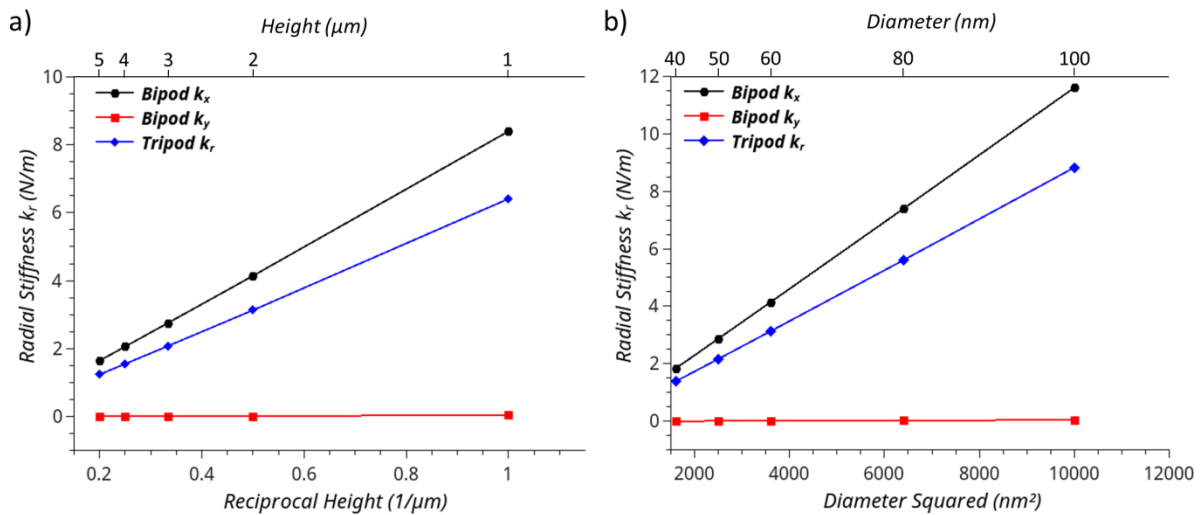


**Figure 34:** the bipods and tripods stiffness  $k_x, k_y$  and  $k_r$  are proportional to the reciprocal height (a) and the squared diameter (b) as is the case for the axial stiffness of a single pillar, due to an increasing character of compression in the in-branch direction.

The results for the tripods radial stiffness are shown in Figure 35 (a) for a diameter of 60 nm. One can see the same shape of the curve as discussed for the bipod in x-direction. As well in Figure 34 (a) and (b) the same dependencies as discussed before on the height and the diameter are seen. Yet the absolute value in stiffness of a bipod  $k_x$  is bigger than  $k_r$ , at the same parameters, although the tripod has more branches. To explain this, the same argumentation as before is used, it is that the relative character of axial deflection is bigger for a bipod as the deflection occurs along two whole branches, while for the tripod the deflection occurs along one full branch and only a fraction of 2 branches, therefore has to be lower.

Simulations on a structure with a height offset for one of the pillars showed that, due to loss of symmetry, the structure will respond differently to forces in directions of the radial plane, shown exemplary as a polar plot (Figure 35 (b)), at which the black circle represents the radial stiffness of a standard tripod, the red oval is a tripod with the same basic geometric parameters, but an additional height offset for one branch. The depicted angle corresponds to the angle relative to the branch with offset. Along this particular branch, i.e.  $0^\circ$  the lowest value in stiffness is observed, which is in accordance with a qualitative picture, that since this particular branch has an increased height the stiffness in turn decreases. Yet, in the  $y$ -direction the same stiffness for both structures is observed. This can be regarded to the negligible influence of the offset branch as it is perpendicular to the direction of deflection, as shown before for bipods. The dependency of the axial and radial stiffness on the geometric parameters stayed the same, but with slightly decreased values.

Summing up, from the investigations so far it can be said that most properties of the architectures can be derived in a qualitative picture from the single pillar behavior, which becomes evident by the same scaling with geometrical parameters height and diameter as for axial deflection of a single pillar. Tripods have a constant stiffness in the radial plane, while a bipods stiffness in radial directions is determined by two values, i.e. the stiffness along the branch direction and the stiffness perpendicular to this direction. The difference between these values is about 3 orders of magnitude, at which the stiffness along the branch is much higher since the contribution from the axial branch direction is much larger compared to deflections in other directions.

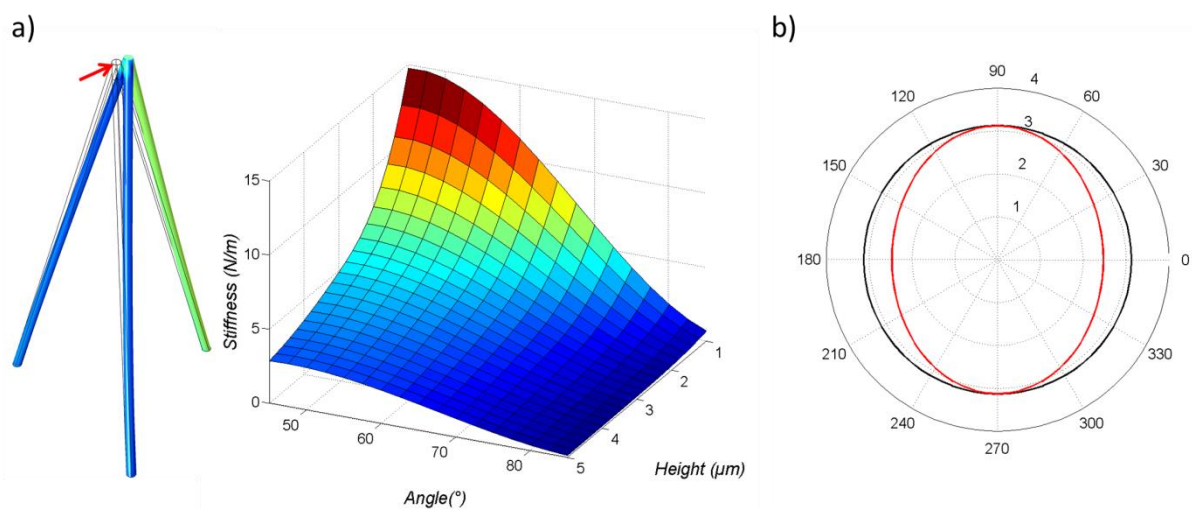


**Figure 35:** (a) deflection of a tripod in radial deflection and the radial stiffness. (b) polar plot of the stiffness in different directions in the radial plane for a symmetric tripod (black) and a tripod with a height offset for one of its branches (red).

### 5.1.5 Tetrapod

Adding another pillar to the architecture leads to the tetrapod, shown in Figure 36 with the same basic parameters as for the tripod. For the simplest case the slanted pillars are placed on the corners of a square (width  $S$ ) leading to 4-fold axial symmetry in the radial plane, thus a constant stiffness is observed in this plane. Parameter variations were done for the height  $H$ , the diameter  $D$  and the angle  $\alpha$  relative to the ground in the same regimes as for the investigations before. Besides the case of a square footprint the behavior of the structure was investigated for rectangular footprints, considering aspect ratios of 1:1.5, 1:2 and 1:3, yet it should be mentioned that with a certain AR of the footprint the angle of the branch relative to the ground changes as well.

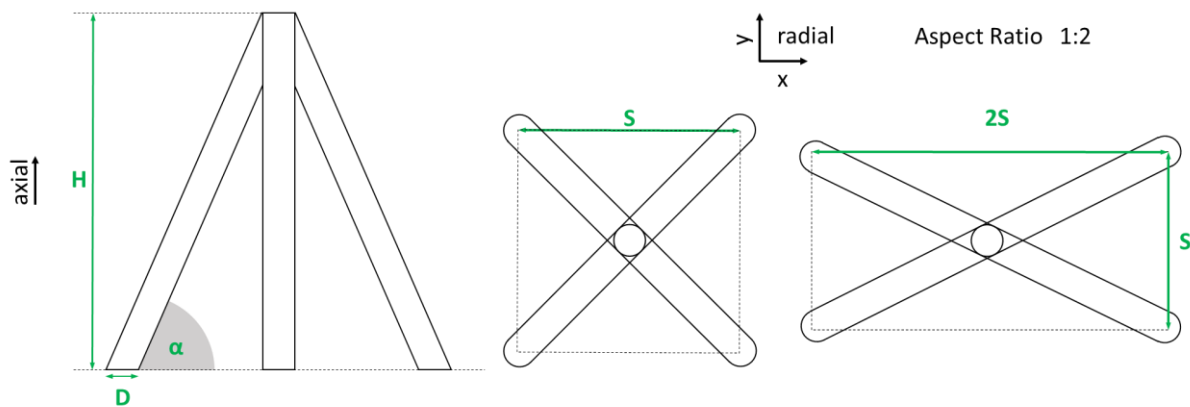


**Figure 36:** front and top view of a tetrapod architecture, determined by the parameters height ( $H$ ), diameter ( $D$ ), angle relative to ground ( $\alpha$ ) and from this follows a certain span ( $S$ ). Square footprints and rectangular footprints with certain AR were considered, as for example an aspect ratio of 1:2.

For the case of a square footprint one can see qualitatively the same shape of the radial (a) and axial (b) stiffness in Figure 37 as discussed before for the tripod, at which the absolute values of the axial stiffness are higher by a factor of about  $4/3$  compared to the tripod, which in turn can be directly explained by the added branch. While the axial stiffness has about the same value as simulated for the bipods, which stems from the fact, that on the one hand this architecture has an axial-symmetric stiffness and deflection in direction of a branch is comparable to the situation of the deflection of a bipod in the branch direction plus a deflection of a bipod in the direction perpendicular to the branch direction. Since the contribution from the former is about 3 orders of magnitude higher it determines the stiffness in radial direction.

With the introduction of a certain aspect ratio of the footprint a change of the radial stiffness from a circle to an oval is observed, depicted in Figure 38 (a) for an exemplary structure ( $H=2 \mu\text{m}$ ,  $\alpha=70^\circ$ ,  $D=60 \text{ nm}$ ). Again this behavior stems from the loss of symmetry, as discussed before for the case of a tripod. The change of the stiffness towards different directions is regarded to an increase / decrease of the ratio of in-branch deflection in the  $x$  and  $y$ -direction, respectively. Remarkable at this result is however that in all cases of an AR the increase in  $x$ -direction goes by a much larger factor than the decrease in  $y$ -direction. Moreover, the change in the dependency of the axial stiffness on the aspect ratio is depicted in Figure 38 (b) for tetrapods with heights of  $1 \mu\text{m}$ ,  $3 \mu\text{m}$  and  $\alpha$  of  $80^\circ$ ,  $60^\circ$ . It can be

seen that in general the axial stiffness decreases for all observed heights and angles, which is in agreement with the findings before, which showed that with decreasing  $\alpha$  and increasing branch length / height, the axial stiffness decreases as well. However, the introduction of a certain AR might overall be beneficial, as it increases the stiffness in a certain direction considerably, yet the axial stiffness and the other radial stiffness values only decrease by a small amount. However, this could be a big advantage for the tetrapods application as probes on cantilevers, since the structure could be deposited in such a way that the higher stiffness aligns with the scan direction of the cantilever, thus reducing the influence of undesired lateral bending of the probe as was discussed in Figure 23 (c).

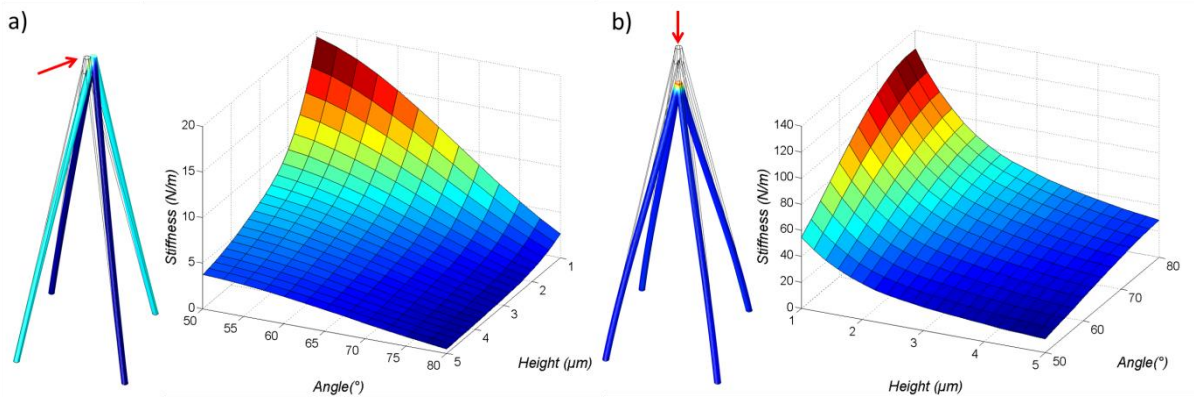


**Figure 37:** radial (a) and axial (b) deflection of a tetrapod and their derived stiffness as function of the height  $H$  and angle  $\alpha$  for a diameter  $D=60$  nm.

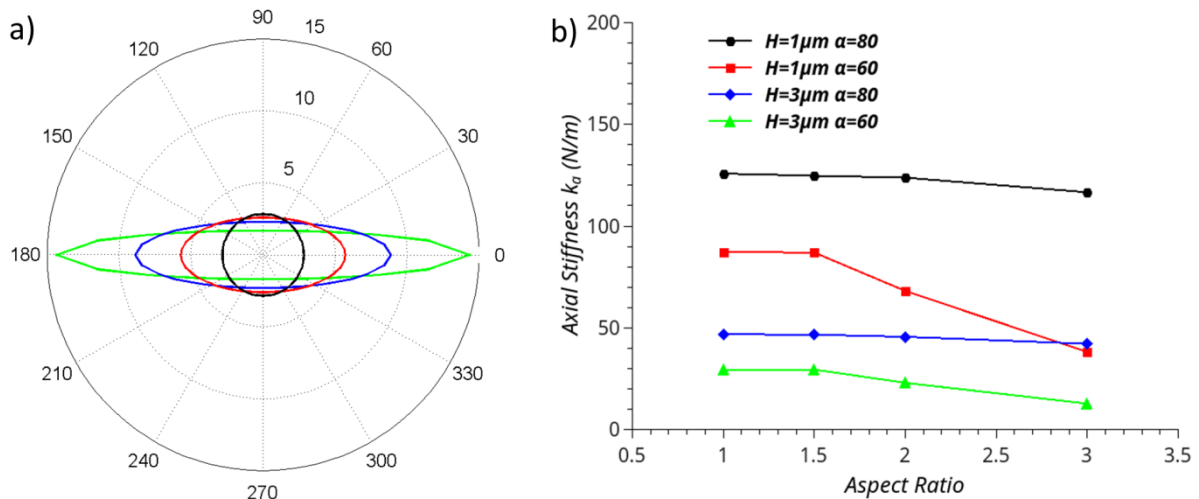


**Figure 38:** a polar plot (a) reveals a change of the radial stiffness for the considered AR of 1 (black), 1.5 (red), 2 (blue) and 3 (green), for which the loss of stiffness in one direction is not as high as the gain of stiffness in the other direction. (b) a plot of the axial stiffness versus the aspect ratio for certain geometries reveals that the axial stiffness decreases with increasing AR, which is stronger for tetrapods, whose initial angle  $\alpha$  were already smaller for a square shaped footprint.

### 5.1.6 Overall Behavior

For the above-mentioned architectures we observed in all cases a linear behavior between displacement and force, thus the stiffness is constant and not dependent on the displacement. An exemplary curve is shown for the case of axial deflection of a tetrapod in Figure 39, clearly showing linear behavior between displacement and force. The two points at large displacements deviating from the linear behavior can be attributed to non-converged solutions. This, in turn points out a limitation of our simulation.

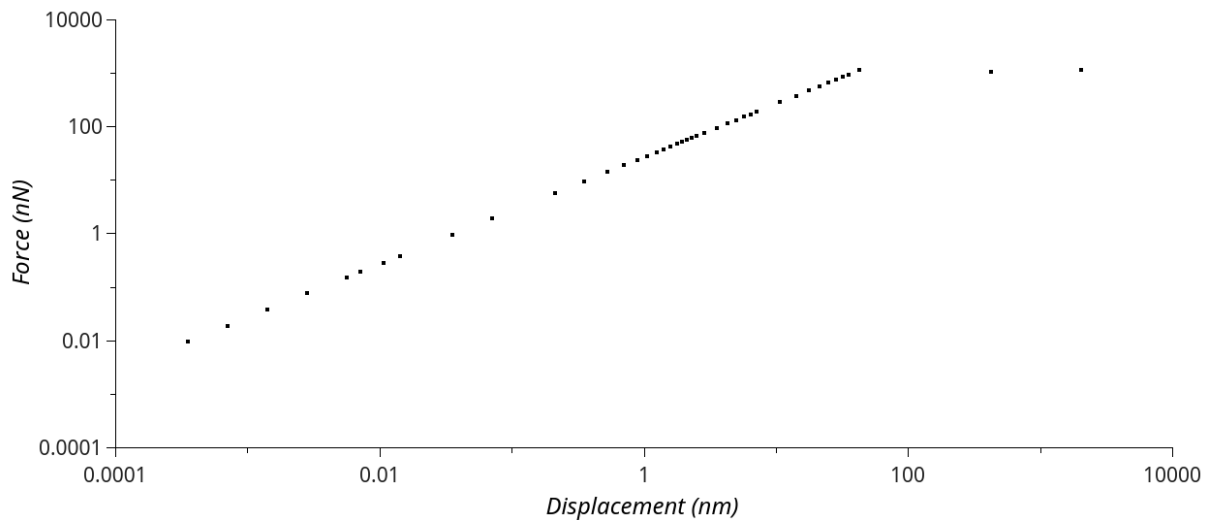


**Figure 39:** a double logarithmic plot of the force – displacement shows a linear slope. The two outliers at high displacement are no representative for the simulations, as they represent non-converged solutions.

Since for all investigated structures similar trends were observed a short comparison is given between the different architectures. Figure 40 shows the change of axial (a) and radial (b) stiffness as more and more branches are added to the architecture, for different geometries. Fundamentally, the branches can be seen as individual springs, which in total comprise a system of parallel springs. Therefore each branch will contribute, depending on the direction of applied force, somehow to the total stiffness. In axial direction, Figure 40 (a), the stiffness increases with increasing number of branches, at which the slope from bipod to tetrapod is linear because each branch contributes in the same way, as they have relative to the applied force the same orientation. The single pillar is not on this straight line, as it differs from the other geometries by its angle relative to the ground!

Regarding the radial stiffness, Figure 40 (b), one can see that in general, its value is at least one order of magnitude lower than in axial direction. The stiffness of the single pillar is by far the lowest of all architectures, simply because its structure does not confront the applied force anyhow. This situation changes drastically for multi-branched structures. The bipods radial stiffness is determined by two constants, at which the in branch direction is the much higher one and in fact has almost the

tetrapods stiffness. Yet, as discussed and shown in Figure 32, the bipods overall radial stiffness is more influenced by the stiffness in the perpendicular direction, which is comparable to a single pillar. A tripods stiffness is lower than the maximum bipods stiffness, but constant in the radial plane. This property arises, as the bipod structure has two full branches in one particular direction, while the tripod has effectively only one full and fractions of 2 other branches. Finally, the tetrapod architecture has the highest stiffness in the radial plane, which is as well constant.

Based on these simulations the experiments in the following focus on tetrapod structures, as they exhibit the highest stiffness in all directions, as well being constant in the radial plane. The latter fact is of extreme importance for structures that should be utilized as AFM nanoprobe, as it reduces an unwanted lateral bending of the probe, as shown in Figure 23 (c). Moreover, they can be deposited symmetrically on two electrodes, which would not be the case for a structurally symmetric tripod. This property in turn results in a more homogeneous current flow as would be the case for a thermal nanoprobe.

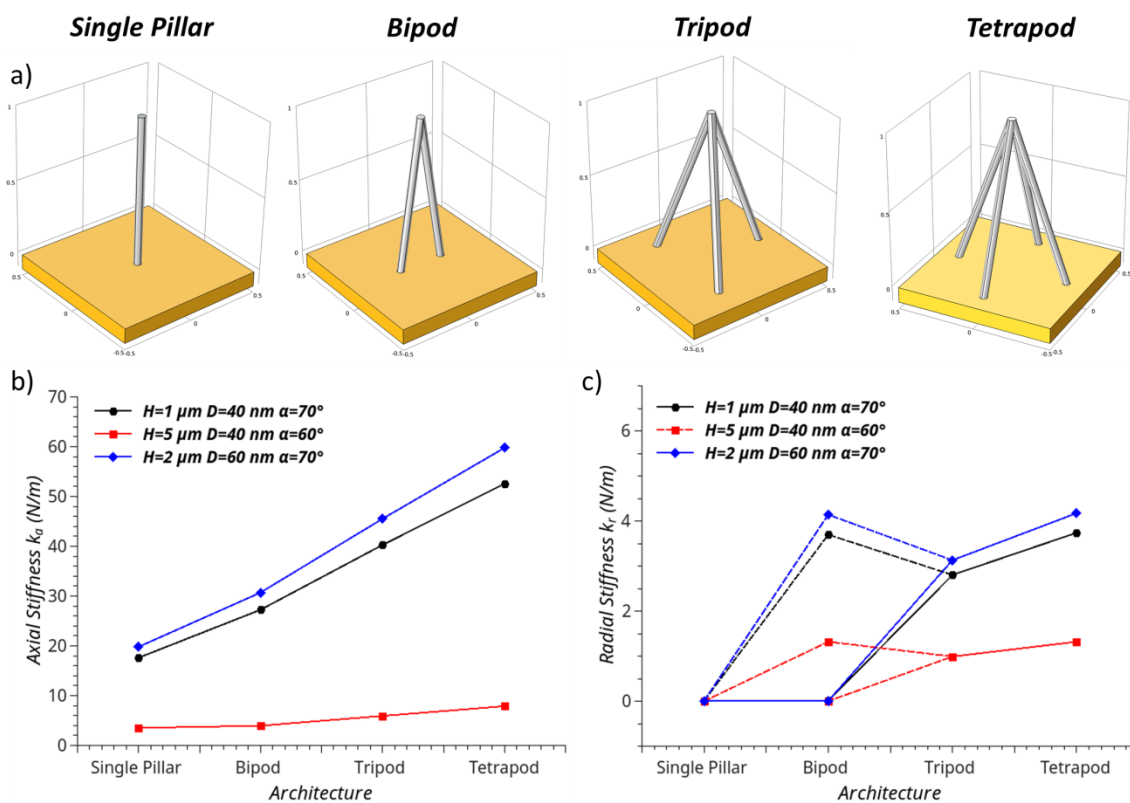


**Figure 40:** (a) the investigated architectures in this study. A relative comparison on the stiffness in axial (a) and radial (b) direction for the investigated architectures for various geometries. One should consider in (b) that the radial stiffness of a bipod is determined by two values,  $x$  and  $y$ , the former being the much higher value and connected by dashed lines.

## 5.2 Deposition of Tetrapods

Before the mechanical characterization of the tetrapods two experiments regarding the design rules were conducted considering the patterning arrangement and the deposition parameters. The former is, as discussed in section 3.5 determined by the GIS alignment, which on the other hand is fixed due to technical reasons. Hence it is basically only possible to change the angle of the pattern relative to the GIS nozzle. This was done with a focus on the quality of the deposited structure, i.e. the similarity between different branches, therefore highest quality is seen when all branches have the most similar appearance. For that purpose, structures with an intended height of  $2\ \mu\text{m}$  and opening angle  $\alpha$  of  $60^\circ$  were deposited, as such small angles are most prone to influences of the patterning arrangement. The rotation angle of the pattern relative to the gas flux vector (**GFV**) was varied in steps of  $5^\circ$ . Between each deposition the stage was moved to the next position in order to avoid any possible influence of the beam shift or spatial variations in precursor coverage. Before deposition the stage was not moved at least for 5 minutes, to minimize any influence from subsequent stage drift. A comparison of different angles, Figure 41, shows that the best overall quality was achieved for an angle of  $45^\circ$  between GFV and branches of the tetrapod. For all angles it was observed that a certain difference in the branch quality is always present, which reveals that the deposition regime is not, as desired, electron limited but determined by surface diffusion and direct gas flux replenishment. Especially in case of  $0^\circ$  and  $15^\circ$  pattern rotation relative to the GIS main axis one can see that branches growing away from the gas flux vector (**GFV**) are built much lower than all other branches, and therefore cannot merge at the top. The root cause of the different branch quality is schematically depicted from different views in Figure 42. It is assumed that as depicted in (a) branches that are built perpendicular to the GFV have a better replenishment by diffusion from the deposit, as their sides face the GFV, resulting in higher branches than those that are built along the GFV. The difference in branch quality parallel to the GFV stems most likely from shadowing effects on the substrate<sup>71</sup>. As can be seen in (b) the geometrical shadow of branches that are built away from the GFV is much bigger than those that are built towards the gas flux. Hence the reservoir from which precursor molecules can diffuse towards the deposit is effectively smaller and therefore a difference in height can be seen even if the pattern is aligned at an angle of  $45^\circ$  relative to the GIS. The here observed effects are most pronounced for taller heights and smaller angles of the branch relative to the ground and restrict the possible geometries in the following investigations.

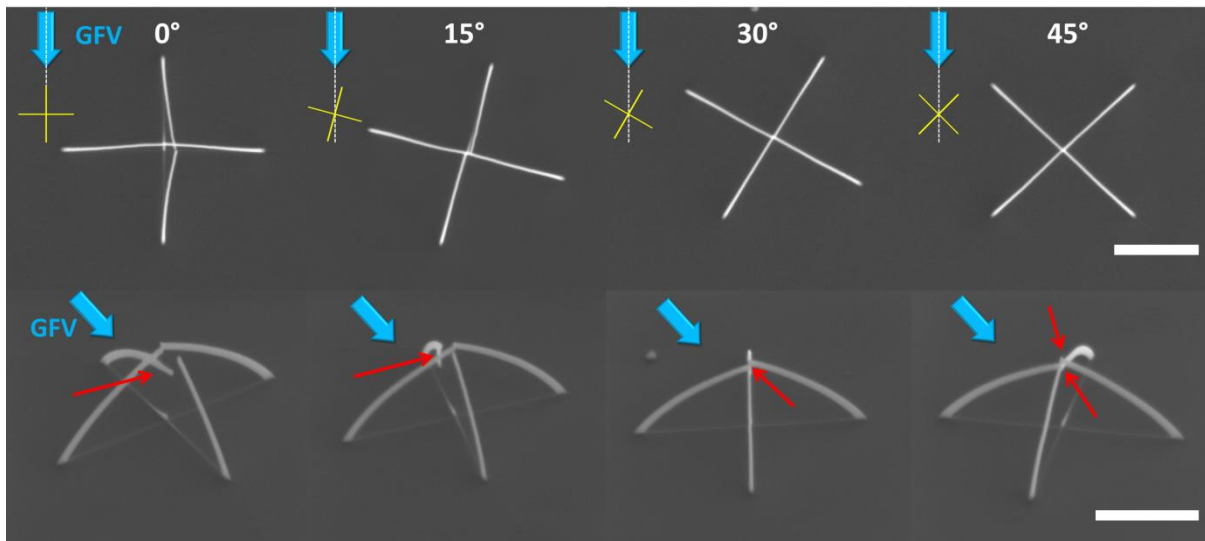


**Figure 41:** variation of the angle between pattern and gas flux vector shows on the one hand that the deposition regime is in all cases not electron limited, as branches differ dependent on their alignment relative to the gas flux vector (GFV). This is indicated by red arrows, pointing towards the arising shadowing effects. Qualitatively best results are achieved for an angle of 45° between branches and GFV, yet still a qualitative difference is still present in branches growing towards the GFV and those that are growing away. The white scale bar for each row corresponds to 1  $\mu\text{m}$ .

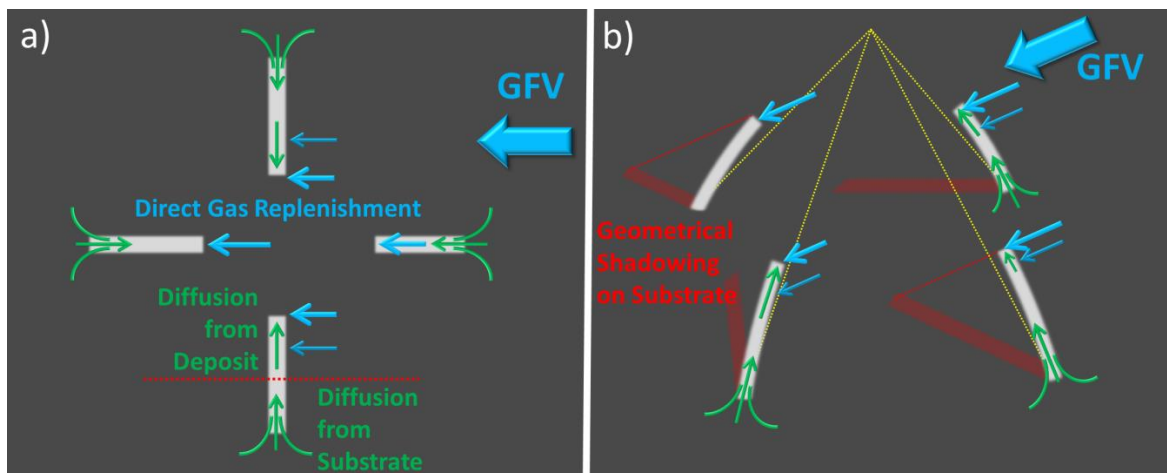


**Figure 42:** top view (a) and tilted view (b) on a schematical explanation for different branch qualities and their origin, as different replenishment mechanisms are prevalent. Determined by the geometry and the direction of the direct gas flux vector (GFV) replenishment by direct gas flux, diffusion from substrate and diffusion from deposit occurs. The GFV and replenishment channels by such are indicated as blue arrows, while replenishment channels by diffusion are indicated by green arrows. The intended structure of the tetrapod is shown as yellow dotted lines. Depending on the geometry and the GFV a certain shadowed region emerges (red shaded).

Considering the processing parameters the acceleration voltage was fixed at 30 kV and the beam current at 21 pA, since these parameters are closest to the desired ELR, thus making the deposition of free standing 3D structures much easier. Moreover, the PoP was set to 0.1 nm, i.e. the smallest possible applicable value considering tetrapods with largest footprints. Therefore basically only the DT is left to be varied. However, this parameter is determined by the input parameter  $\tau$  of the

FEBIP CAD software<sup>57</sup>, which was therefore effectively varied for the heights 1  $\mu\text{m}$ , 2  $\mu\text{m}$  and 3  $\mu\text{m}$  considering angles of 50°, 60°, 70° and 80°. Yet it should be mentioned that especially for higher structures and larger footprints (smaller  $\alpha$ ) the actual structure deviates strongly from the intended as shown in comparison in Figure 43 (a), at which the intended geometry is superimposed on the actual geometry as yellow dashed lines. In the further discussion the angle  $\alpha$  is split into the effective angle  $\alpha_{\text{eff}}$ , representing the angle between the surface and a straight line from the onset of the branch to the tip, while the take-off angle  $\alpha_{\text{TO}}$  is defined by the initial angle of the branch, both depicted in Figure 43 (b). The immediate decrease of the branch angle at a height of about 200 nm can be directly linked to the change of the replenishment regime from surface diffusion by substrate to direct gas flux replenishment. As indicated in Figure 42 (a) by a red dotted line diffusion from substrate is limited by the mean diffusion length of the precursor molecules to a certain height of the branches. Whereas the further ongoing decrease might be caused by an electron beam field-induced movement of the branches and / or a decrease of the interaction volume within the structure as the path the electrons are able to travel within the structure becomes smaller<sup>72</sup>, which are topics of other ongoing investigation. The optimized values in order to obtain particular heights at given angles ( $\alpha_{\text{eff}}$ ) are shown in Figure 44 (a), at which one can see higher values of  $\tau$  for higher and steeper branches. Considering the same height, the same paths are patterned (the same pixels are addressed), therefore a longer DT is needed in order to deposit more material at a certain pixel. Then for higher structures again a higher value of  $\tau$  becomes necessary, due to the curvature of the branch. This is further underlined in Figure 43 (b), which shows the ratio of  $\alpha_{\text{TO}}$  to  $\alpha_{\text{eff}}$  versus  $\alpha_{\text{eff}}$  and the height  $H$ . One can see that with increasing height and decreasing  $\alpha$  the actual structure diverges more and more from the intended one, because a higher  $\alpha_{\text{TO}}$  becomes necessary to compensate for the curvature of the branches.

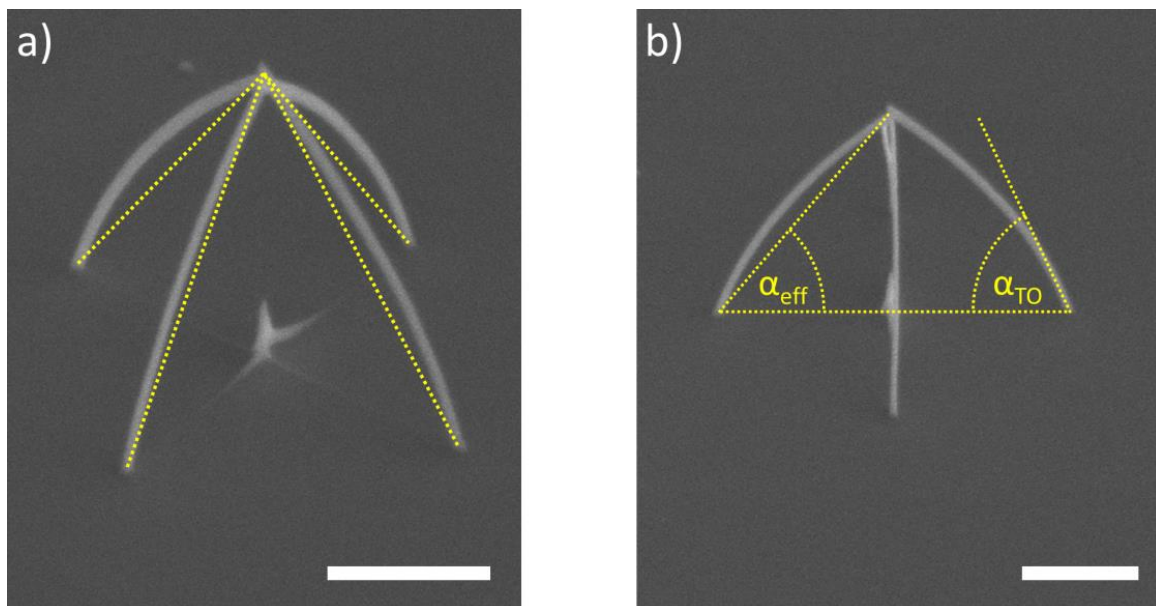


**Figure 43:** (a) tilted view of a tetrapod shows a clear deviation of the actual structure from the intended, which is superimposed on the picture as red dotted lines. (b) Therefore to characterize the tetrapods better the opening angle  $\alpha$  is replaced by two characteristic angles, i.e. the effective angle  $\alpha_{\text{eff}}$  and the angle of the branch close to the surface  $\alpha_{\text{TO}}$ . The scale bar shown in each micrograph at the bottom right corner represents 1  $\mu\text{m}$ .

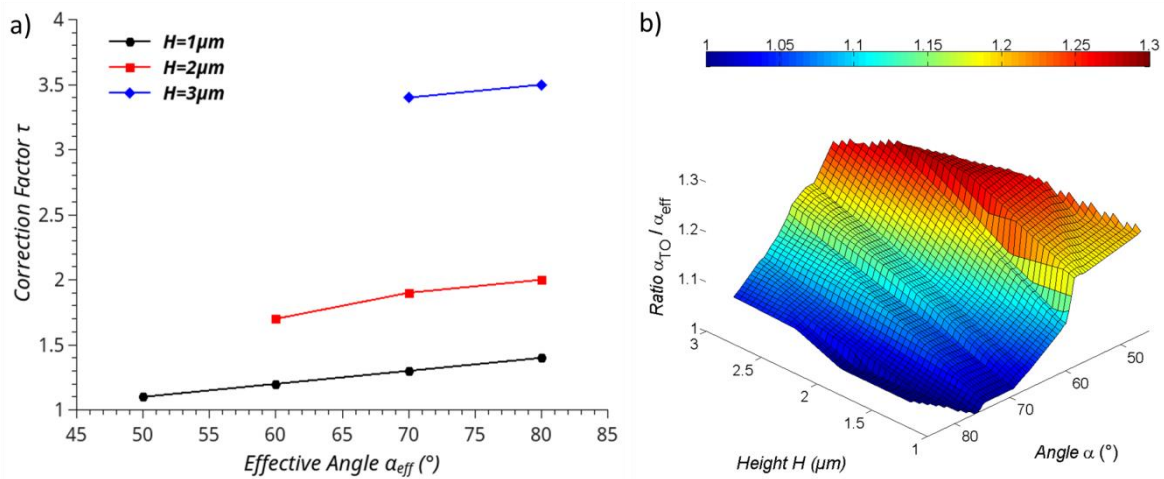


**Figure 44:** (a) the ideal  $\tau$  (abscissa) to obtain the desired angle  $\alpha$  (ordinate) for heights of  $1\mu\text{m}$  (black),  $2\mu\text{m}$  (red) and  $3\mu\text{m}$  (blue). (b) the deviation of the actual from the intended structure indicated by the ratio of take-off angle  $\alpha_{\text{TO}}$  to effective angle  $\alpha_{\text{eff}}$ .

### 5.3 Preparation and Characterization of the Cantilever

Before mechanical measurements, the cantilever (Figure 45 (a)) had to be modified in such a way that 3D structures can be probed in a reliable way. In detail, the front of the cantilever was removed (b), thus the tip would be accessible by the electron beam, which allows for imaging during probing. Then the tip itself was trimmed in such a way that a probing plateau would emerge, which would be parallel to the base of the probed structures during measurements. Finally, the total area of the tip was reduced in order to avoid probing of any structures which would lie behind the tip and to ensure that the probing conditions are similar for all measurements.

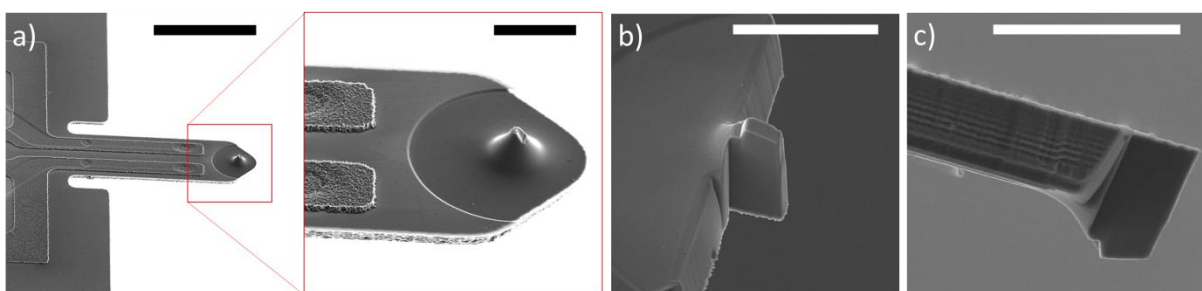


**Figure 45:** modification of the cantilever tip (a), at which the front of the tip was cut off (b) and a probing plateau (c) was cut, thus the probing area would approach the structures perpendicular. The shown scale bars correspond to  $50\mu\text{m}$  in the first micrograph and  $10\mu\text{m}$  for the others.

After modification, the stiffness of the cantilever  $k_c$  had to be determined, which was done by analytical calculation (Equation 13<sup>73</sup>) and FEM simulations. For both a Young's Modulus of 150 GPa was assumed<sup>24</sup> and the true geometrical parameters of the cantilever were used, i.e. a length  $L$  of 330  $\mu\text{m}$ , width  $w$  of 110  $\mu\text{m}$  and thickness  $t$  of 4  $\mu\text{m}$ . Furthermore, for simulations (Figure 46) a density of 2330  $\text{kg m}^{-3}$  and a Poisson's ratio of 0.22, as well the aluminum connections on the cantilever were included. By calculations, the stiffness was determined to be 7.35 N/m, by means of simulations to be 7.45 N/m. As this value is on the one hand close to the analytical value and on the other hand no other possibility was given to check its validity, it was adopted to be the cantilevers stiffness.

$$k_c = \frac{Ewt^3}{4L^3} \quad \text{Equation 13}$$

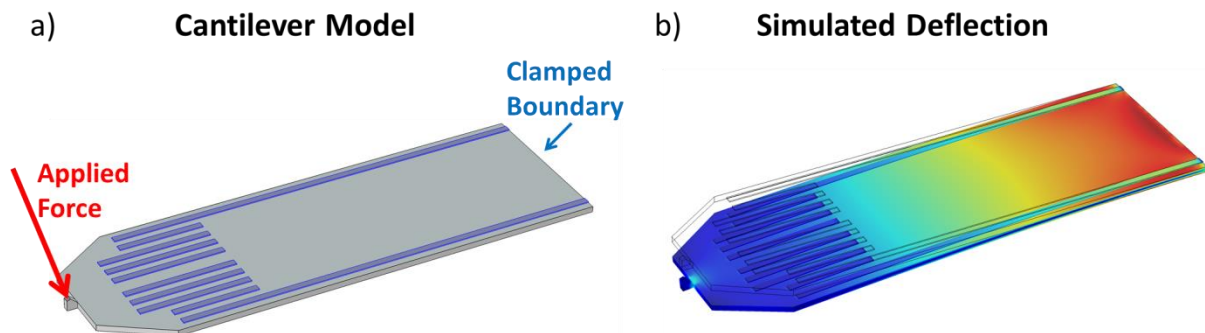


**Figure 46:** (a) model of the cantilever including the metal connection. The applied force which will act on the cantilever is indicated by a red arrow, while the only fixed connection is at the cantilevers back. (b) after simulation, the cantilever would deflect in a particular manner, from which its stiffness can be determined.

As described in section 2.3, a quantitative determination of the stiffness necessitates the knowledge about the cantilever sensitivity, i.e. the change of the voltage in  $V_w$  with applied deflection, in actual fact the stiffness in units of V/nm. Determination of this parameter was done simply by probing a silicon substrate, as it can be assumed that the stiffness of the substrate is several magnitudes higher than the cantilever, thus the reciprocal value becomes negligible in Equation 1 and the slope of this measurement is virtually equivalent to the cantilever sensitivity,  $s=0.29$  mV/nm. The conversion factor from units of V/nm to N/m is calculated to be 26.23  $\mu\text{N/V}$ .

## 5.4 Qualitative Measurements

First measurements of tetrapods were done to understand the qualitative behavior of the mechanics better, to see if in fact measurements on such a small scale would be feasible, how certain parts of the structure would bend under a load or if the as-deposited structures would have actually brittle character and thus are not suitable as AFM probes. Moreover, this would give a first look at how much the conducted simulations are in accordance with the real tetrapods. A quantitative evaluation was not possible at the same time since for this investigation the AFSEM had to be operated in amplitude mode, thus within the feedback loop not the voltage on the Wheatstone bridge is used to adjust the cantilever but the amplitude while the cantilever is in resonance vibration. This became necessary for two reasons, charging of the cantilever and the sensitivity of the feedback signal. The former comes from irradiation with the electron beam, which in turn leads to charging of the Wheatstone bridge during contact mode AFM, thus the measurement would be systematically wrong. A higher sensitivity was necessary as higher and low angled tetrapods with low stiffness are extensively compressed before a proper signal for  $V_w$  is obtained. All measurements with the AFSEM were done using a tilted holder to gain as much accessibility with the electron beam as possible (Figure 9 (b)).

A typical investigation is depicted in Figure 47. In (a) one can see the tetrapod before deflection. To be sure that the cantilever was properly in contact with the structure the stage was approached towards the cantilever until a certain deflection was visible (b). Problematic about this step is the control of the z-movement of the stage by a mechanical screw, which allows only, relative to the dimensions of the tetrapod, a coarse movement, hence already during the approaching step a strong compression was induced. After the cantilever was in contact with the structure a ramping of the z-position of the cantilever was executed, at which the tetrapod would be compressed (c) and then released (d). After the measurement, a plastic deformation was visible (e), which however is much smaller than the deflection at the highest deflection of the structure (c). Therefore it can be said that the tetrapod exhibits widely elastic behavior, as well to be more ductile than brittle. Both properties make these structures in general applicable as nanoprobe.

However, in (e) a comparison between measurement and simulation is given and at once it is obvious that the biggest difference between simulation and experiment is a twisting of the structures, observed for almost all geometries, with the exception of very stiff tetrapods (small heights and  $\alpha=80^\circ$ ). In these cases instead of a branch twisting a preferable deformation of the tetrapod apex appears, as shown in Figure 48 (b). In detail, as the cantilever ramps this particular structure (a) it seems that the apex is first deflected in a radial direction (b) which is as well evident by a plastic deformation in radial direction (c) after measurement. This can be understood by looking closer at the particular geometry (d), as it can be seen that the branches merged together, not at the final apex, but much earlier (indicated by a red arrow). This, in turn, results in a hybrid structure of a tetrapod with a single pillar on its top. As discussed in section 5.1.3 the radial stiffness of a single pillar is much lower than a tetrapods axial stiffness. Hence under load, the apex of this structure is first deflected before the branches are bent.

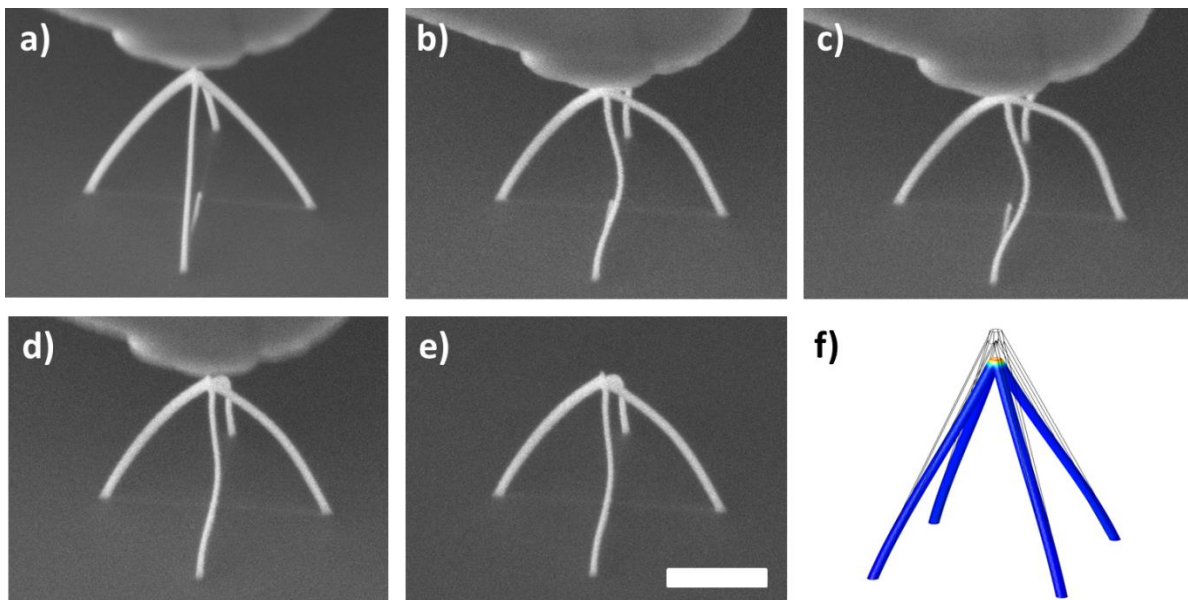


**Figure 47:** a typical investigation on the tetrapod structure. Before approach (a), as approached (b), during ramping (c,d) and afterward (e) compared to a similar simulation (f). At once a difference in the branch deformation during compression becomes obvious. The scale bar shown in (e) corresponds to  $1\ \mu\text{m}$  and is valid for micrographs (a) to (e).

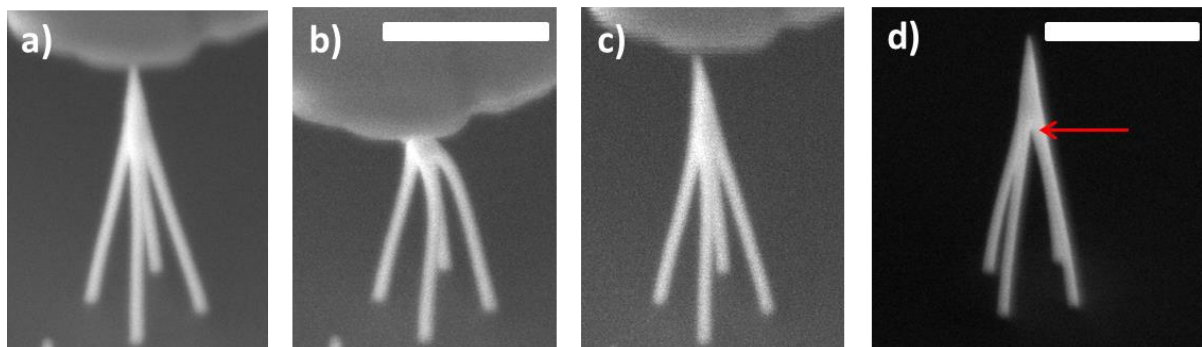


**Figure 48:** for stiffer structures ( $H=2\ \mu\text{m}$ ,  $\alpha=80^\circ$ ) as shown in (a) a stronger deflection of its apex (b) than in its branches was observed, which resulted as well in a higher plastic deformation (c) in this region. (d) the cause of this particular behavior is the merging of the branches (indicated by a red arrow) before the total height of the tetrapod. The shown scale bars correspond to  $1\ \mu\text{m}$ .

Regarding the bending of the branches different kinds of twisting were observed, as shown in Figure 49, clockwise (a), counterclockwise (b), symmetrically (c) as well non-symmetric (d) twisting of the branches occurred, meaning that in some cases not all branches were twisting into the same direction of rotation. In order to explain this peculiar motion, the model was adapted to include certain deposition related features.

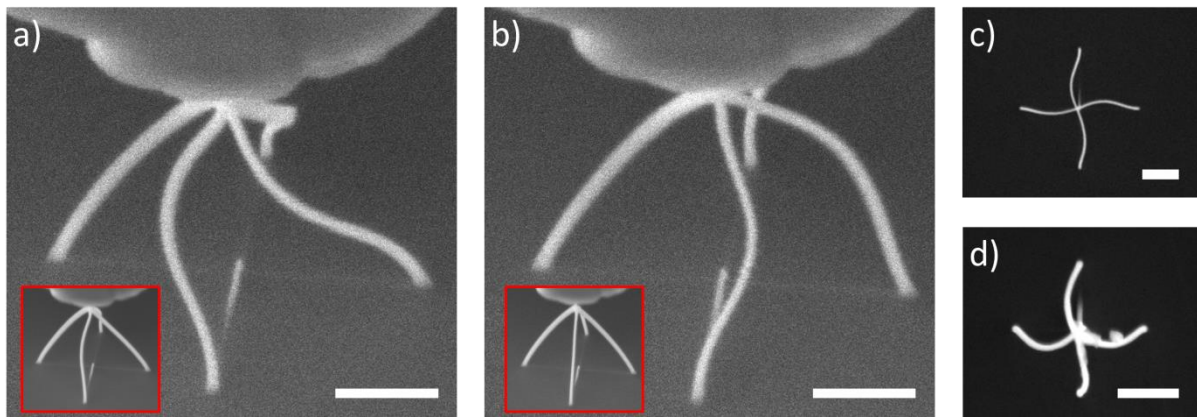


**Figure 49:** for the geometrically same structure a clockwise (a) as well counterclockwise (b) twist was observed. In each case, the red framed inlet shows the structure as approached. Furthermore, symmetric (c) and nonsymmetric (d) twisting were observed. Scale bars at the bottom right corner correspond to  $1\ \mu\text{m}$ .

## 5.5 1<sup>st</sup> Adaptation of the Model

The origin of the twisting motion of the deposited tetrapods has to be caused by some kind of inhomogeneity within the tetrapod structure or in the measurement, which distorts or destroys the axial symmetry. A measurement inhomogeneity might stem from a non-parallel alignment of the cantilever probing face with the base of the tetrapod, which would lead to a load acting not only in the axial direction of the tetrapod but also including some radial direction. Simulations, Figure 50, reveal that indeed a certain out-of-branch-axis-plane bending is obtained, but this does not resemble the above-seen measurements, as the branch bend asymmetrically. Furthermore, one can see that for such cases the apex of the tetrapod is deflected strongly in the radial plane, which was not observed at all before. In total, measurement inhomogeneities might be present but cannot be the sole cause of the twisting motion.

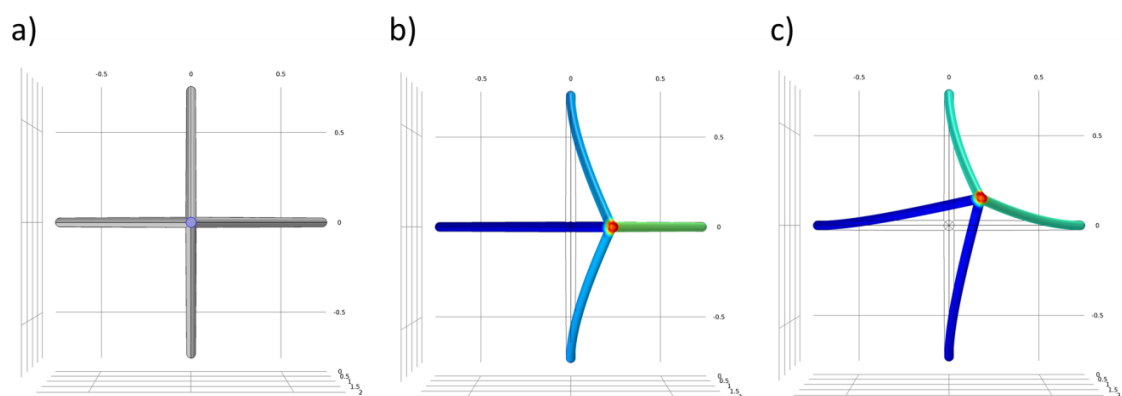


**Figure 50:** top view of an undisturbed tetrapod (a), a tetrapod under axial-radial load in different directions (b,c), as it would occur for a non-axial measurement. One can see indeed a certain bending of the branches occurring as a mix of radial and axial direction, yet a symmetric twist cannot be caused by this kind of inhomogeneity.

A closer look at the apex of a tetrapod, Figure 51, reveals a certain mismatch for the merging zone of the individual branches in axial direction (b) as well in the radial plane (c), indicated as a red shaded area. Therefore, this particular feature was introduced into our simulation, by keeping the onset position of each branch fixed and change the end point of the branch, thus a mismatch to the virtual middle of the tetrapod arises. Representative simulations for a tetrapod ( $H=2\ \mu\text{m}$ ,  $\alpha=60^\circ$ ) in Figure 52, including different types of mismatches, of single (a) and several branches (b) in axial direction show the different resulting cases of obtained twist. Interestingly, these results are obtained even for a mismatch as small as 1 nm, which is essentially below the resolution limit of a SEM. On the other hand since the resolution of FEBID structures is well above this limit, a mismatch in this range will most likely always be present. Due to these findings, it can be said that the main cause of the twisting motion is mismatches in the merging zone of the branches.

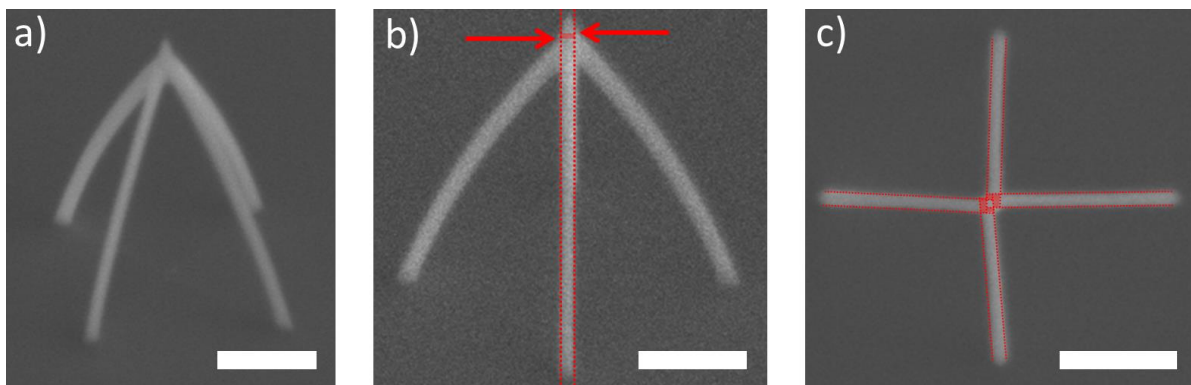


**Figure 51:** (a) tetrapod with a height of  $1.5\ \mu\text{m}$  and  $\alpha_{\text{eff}}$  of  $65^\circ$  shows minimal mismatches in the merging zone of the branches in axial direction (b) and in the radial plane (c). Mismatching areas are indicated as red shaded. Scale bar in the right bottom corner correspond to  $500\ \text{nm}$ .

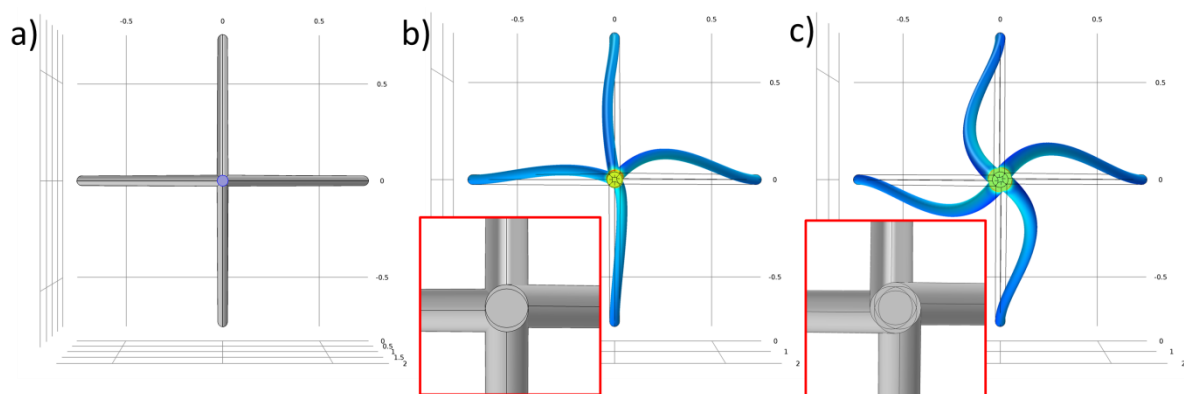


**Figure 52:** (a) the model of a tetrapod ( $H=2\ \mu\text{m}$ ,  $\alpha=60^\circ$ ) can be refined by introducing a mismatch of the merging branches of one branch (b) leading to an asymmetric twist, of all branches (c) leading to a symmetric twisting.

## 5.6 Quantitative Measurements

In order to obtain quantitative values for the stiffness, the tetrapods were approached in a similar manner as described above, while the AFSEM has to be operated in contact mode. This, in turn, leads to unwanted charging of the cantilever during electron beam imaging, which is nonetheless unavoidable to approach the structure exactly towards the cantilever. After imaging the cantilever discharges over a longer period of time, which becomes evident in force measurements by a certain offset ramp. This offset ramp is indicated by a blue line for a typical measurement in Figure 53 (a). By a linear fit (1) through the non-approached cantilevers measurement data this ramp can be adjusted, subsequently setting the baseline to a constant value of 0 V, as shown in (c). This, in turn, is justified, as the discharging is clearly linear (blue line) in the considered time frame, as depicted in (b). In the following discussion, all measurements are shown charge corrected. The slope of the discharging ramp lies in the range between 0.15 and 0.50  $\mu\text{V}/\text{m}$  and is higher in cases for a longer use of the electron beam. Yet, a quantitative value could not be derived from imaging duration and charging-discharging. Anyhow, one can see a further distinctive feature in the measurement, that is to say, a certain shift of the onset point towards smaller values of the cantilever height becomes evident ((2) indicated by red dashed lines in (a)). Regarding this feature, a comparison of several measurements is given in Figure 54 (a) plotting the starting point of retract (solid) and approach (dashed) versus the measurement time, including the 1<sup>st</sup> (substrate), 70<sup>th</sup>, 140<sup>th</sup> and the last (199<sup>th</sup>) measurement. Approach and retract were split into two curves, as during retract adhesion forces would always give a bigger value in height for the onset point of the cantilever deflection. Important in this diagram is not the absolute value on the ordinate but the slope of each curve since for each measurement the cantilever was approached onto the tetrapods to a different starting position. Even though the lines only go through two data points, it is remarkable that the slopes of the respective curves are pairwise parallel and in general have a similar gradient. Therefore, it is assumed that the shift of the onset point towards smaller heights stems either from a drift in the piezo actuator of the scan head or a drift of the sample stage. We can rule out plastic deformation as the main underlying mechanism, as for that case a nonlinear drift of the onset point would be seen. Furthermore, it is assumed that already after approach the tetrapod is at its maximal plastic deformation since ramping is done only towards positive height values. Besides these general setup related influences, several recurring features were observed. In measurements two plateaus can be seen, i.e. for large heights the uncontacted cantilever (3), therefore no deflection is measured, while for small heights the cantilever continuously deforms the structure without an increase of its own deflection (4), hence compressing the tetrapod at a constant force. Both plateaus are connected by a curve, which is linear (5) close to the onset point, i.e. when the cantilever first contacts the structure (during approach) or close before it loses the contact (during retract). With decreasing height, this linearity is lost (6), the slope of the curve decreases steadily until the upper linear plateau is reached. The linear part of this curve corresponds to the elastic response of the structure, hence it is possible to determine the stiffness of the structure by fitting a straight line through these data points, as shown in (c) by red lines. The non-linear part and the upper plateau correspond to the plastic response of the structure, i.e. a permanent deformation of the structure, which was as well observed before (Figure 47, Figure 48, Figure 49). Furthermore, one can see a certain difference in the applied force of the plateaus (7), even after charge correction, indicated as a red arrow in (c). It was observed that if a split of this plateau is present it would go in most cases towards lower values of deflection, hence less force is

needed with subsequent ramping. This indicates an increasing degree of plasticity within the structure, as it is continuously probed. In addition to that in several measurements, encircled red in Figure 54 (b), a peculiar spike during retract was observed, which occurred almost always exclusively in the first retract of the cantilever. Specifically, the sequence during measurement means that first, the cantilever approaches its equilibrium position or even deflected downwards (0 mV or less), then suddenly it is again highly deformed towards the structure, indicated by a rapid increase in deflection and afterward decreasing steadily again. Because the increase and subsequent decrease of the deflection until equilibrium happen over a few seconds, a snapping of the cantilever due to adhesion forces can be ruled out, as this would happen within a much shorter time frame and should occur not only for the first cycle. At the moment this feature of the curve is not fully understood but it is assumed an electrostatic discharge occurs at the moment of losing contact between cantilever and tetrapod, causing the tetrapods apex to snap up again, thus the positive deflection. Another evidence, that the structure itself comes into play in this effect is given by the similarity of the slopes before and after this spike occurs.

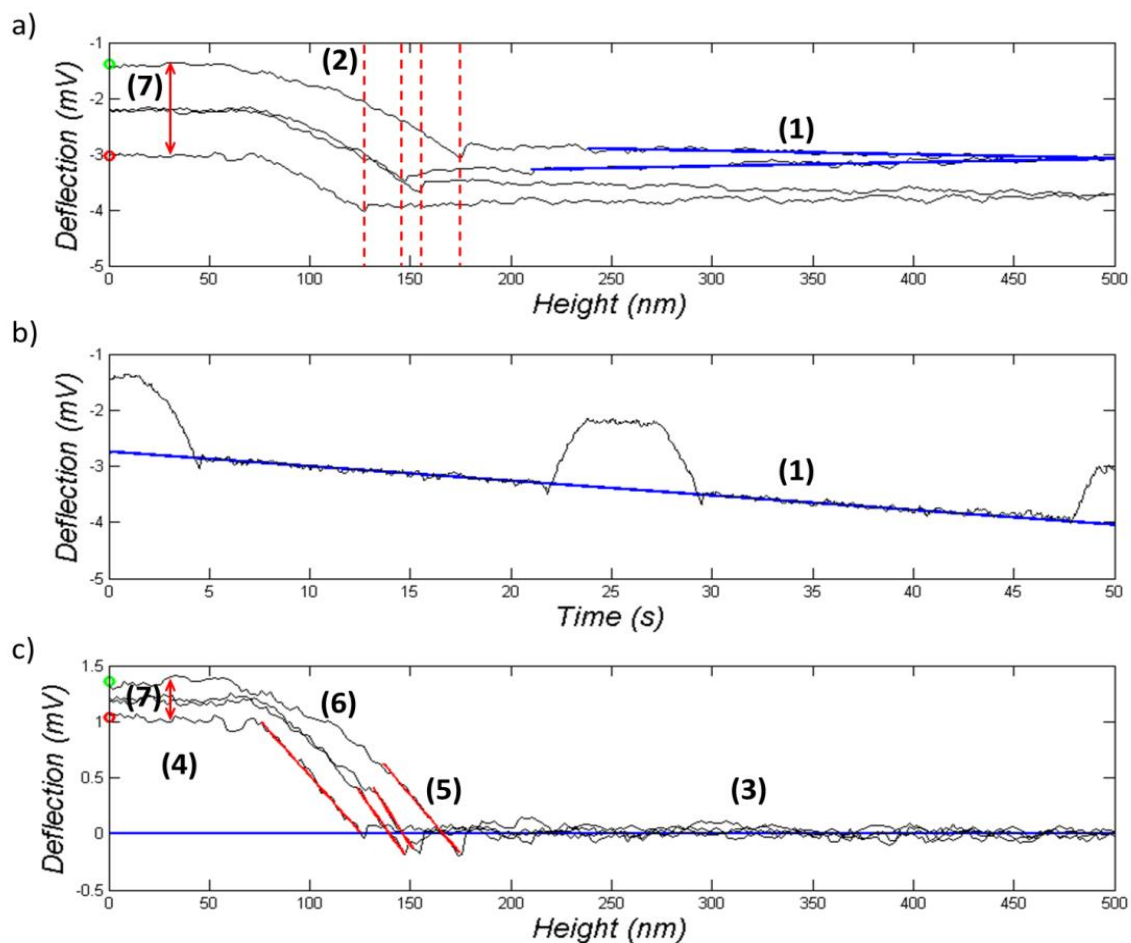


**Figure 53:** uncorrected cantilever deflection obtained from a typical force measurement for two full cycles (retract-approach), plotted against the height (a) and against the time (b). (c) the measurement after correction by setting the linear discharging of the Wheatstone bridge (1) to zero. In (a) and (c) the start and end point of the measurement is marked by a green and red circle, respectively. Furthermore, in (a) and (c) a difference in the measurement is visible at the same cantilever positions, indicated by red arrows (7). A piezo drift induced change of the scan head height or a stage drift leads furthermore to a shift of the onset point (2), indicated by red dashed lines in (a). The stiffness of the probed structure was determined by linear fits through the linear onset (5), indicated by red lines in (c).

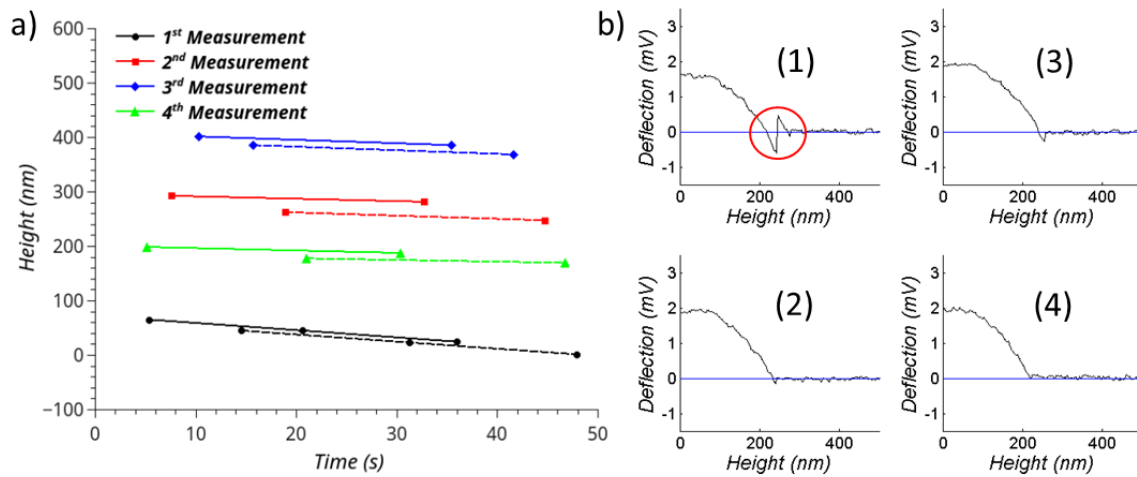


**Figure 54:** (a) comparison of several measurements regarding the onset points for the cantilever show pairwise parallelity for retrace (solid) and approach (retrace). At which the retrace respectively is at higher values, due to adhesion forces. (b) a force measurement splitted in its respective cycles, (1) 1<sup>st</sup> cycle retract, (2) 1<sup>st</sup> cycle approach, (3) 2<sup>nd</sup> cycle retract, and (4) 2<sup>nd</sup> cycle approach. At the first moment of contact loss a spike in the measurement occurs encircled red.

After determining the slope, by a linear fit for each individual measurement, the stiffness of tetrapods was calculated with Equation 3 and subsequently converted to units of N/m, as described in section 5.3. In the following, it was then possible to map the measured stiffness, Figure 55 (a), in order to compare them with the conducted simulations, shown in (b). In detail, (a) shows measurement points indicated by white / black spots, considering their actual geometrical parameters  $H$  and  $\alpha_{\text{eff}}$ . Between measurement points, a cubic spline interpolation was done in order to obtain a full map. Qualitatively both maps are similar, as they show in general strong increase in stiffness towards smaller heights and larger angles. Yet there is one distinct difference, which can be seen for the isoline at a height of 2  $\mu\text{m}$ , which exhibits a maximum of stiffness at an angle of about 80°. This can be regarded to the hybrid form of these structures, discussed in Figure 48, as they are more similar in shape to a combination of tetrapod and single pillar at the apex, radial compression happens quite easily and therefore in total the stiffness decreases as the angle goes from 80° to 90°. From a quantitative point of view one can see that the total values of stiffness differ by a factor of 2 – 20, with particularly strong differences at smaller angles and increased heights.

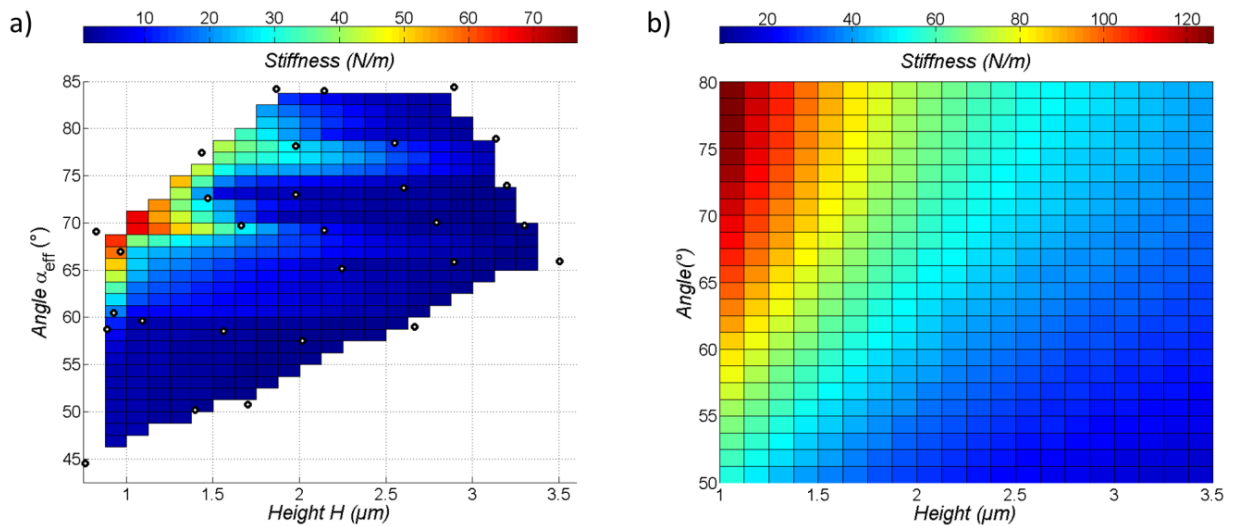


**Figure 55:** a comparison of the stiffness maps between conducted measurements (a) and simulations (b). The basic behavior is the same, i.e. stiffness increase towards increasing  $\alpha$  and decreasing height, yet certain features don't appear in the simulations and the quantitative values differ by a factor of 2 – 20.

At this point, it was assumed that the difference in stiffness observed in simulation might stem from the before observed mismatch, which was not yet introduced into the model for a quantitative determination of the stiffness. Therefore a study was undertaken on how much the stiffness would decrease with an increasing mismatch. In particular one can see in Figure 56 the implication on the axial stiffness for a tetrapod ( $H=2\ \mu\text{m}$ ,  $D=60\ \text{nm}$ ,  $\alpha=60^\circ$ ) as the mismatch increases for all branches. Although the stiffness definitely decreases, even with a high mismatch of 8 nm (a), one can see that the experimental values are still not reached. In a very simple picture, the mismatch should actually change the stiffness not at all, as actually, the branches are the same as without mismatch and in principal it should not matter how they would be placed relative to each other (considering compression in axial direction only!). However, the reduced stiffness stems from a change of the preferred direction of deflection of the branches. In particular, the mismatch leads to a deflection in mixed direction as a certain twist indicates, hence to the total stiffness both directions, axial and radial, will contribute. Therefore, not only the axial stiffness is relevant but as well the radial stiffness leading from the best case (no mismatch) to increased contribution from the radial direction and therefore an overall decrease in stiffness is observed.

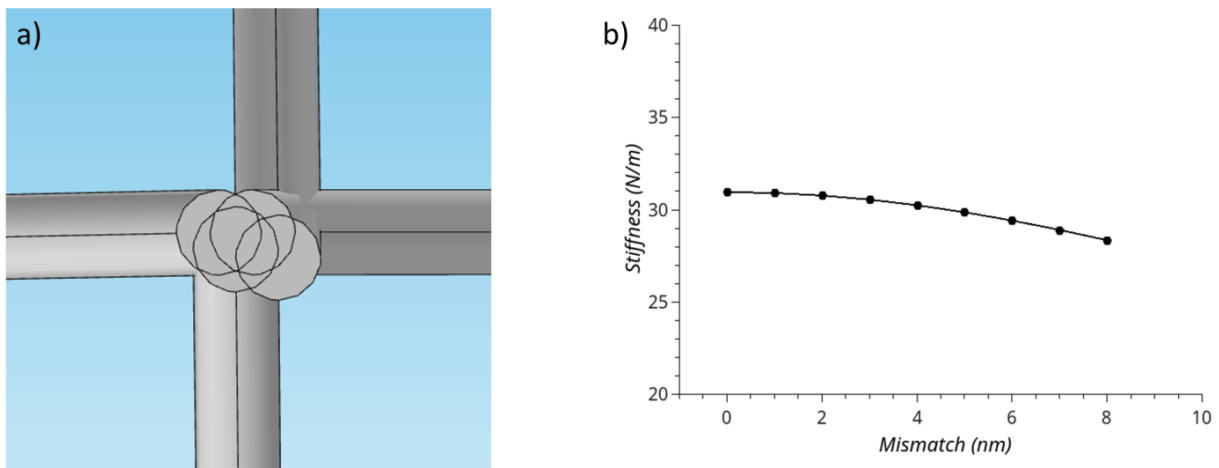


**Figure 56:** (a) introduction of a mismatched branch merging into the model at the extreme case of 8 nm mismatch for all branches. (b) the stiffness would decrease from 31 N/m to about 29 N/m in the extreme case of 4 mismatching branches with 8 nm each.

## 5.7 2<sup>nd</sup> Adaption of the Model

Since measurements and simulations differed by a considerable margin (factor 20) the underlying model was adapted. As discussed already in section 5.2 the branches of the tetrapod are far from being straight, which becomes more eminent for smaller angles  $\alpha$ , as was pointed out in Figure 44 (b). A detailed characterization of a single branch, as shown in Figure 56, reveals that an accurate description of the curvature using a simple mathematical model, such as a 2<sup>nd</sup> order polynomial function or a logarithmic function is actually a quite good approximate description, yet not fully equivalent. Again, this can be explained by the interplay of several complex mechanisms which come into play during the deposition of free standing 3D structures, as for a full description a change in the interaction volume plus a change of SE yield, a change of diffusion regime, an additional species of dissociating particles ( $SE_{III}$  and FSE), possible movements of the branch itself and a consideration of the mean free path of PE in a decreasing branch diameter would have to be included. Therefore the curvature is much more likely to be described by a convolution of several functions.

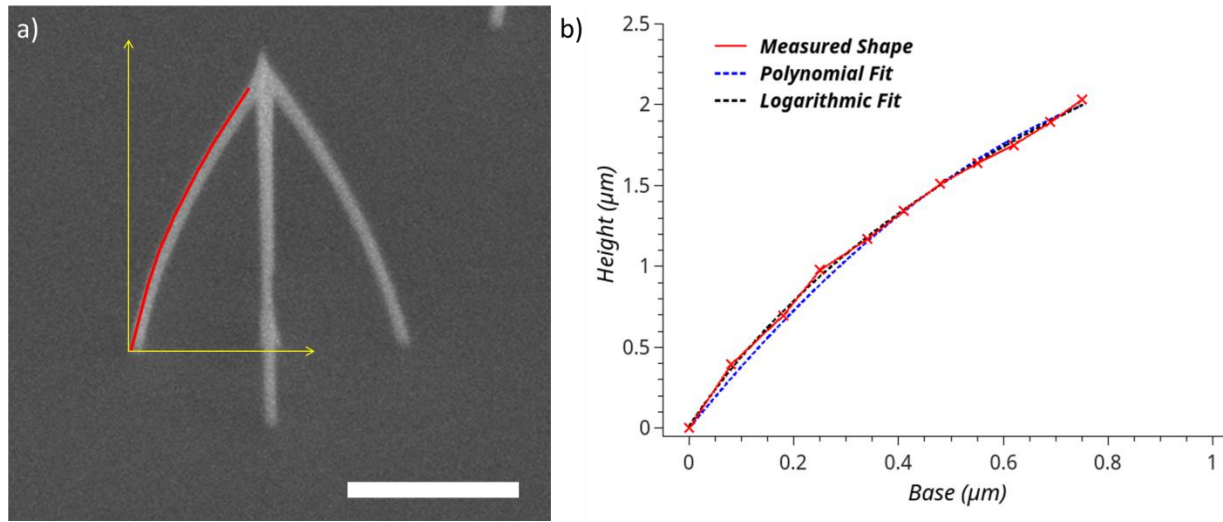


**Figure 57:** (a) the measurement of a single branch (red) transferred in a coordinate system (b) and compared with a polynomial (blue) and logarithmic fit (black). The scale bar in (a) corresponds to 1  $\mu\text{m}$ .

For the following simulations, the model was adjusted in such a way to include the curvature of each branch as a 2<sup>nd</sup> order polynomial function. This was done for three reasons, first of all, such a function can be directly described by two parameters, which in turn are given by the effective angle  $\alpha_{\text{eff}}$  and the take off angle  $\alpha_{\text{TO}}$ . Then, the implementation of such a function into the model is straightforward, making it possible to systematically investigate the dependence of stiffness as  $\alpha_{\text{eff}}$  and  $\alpha_{\text{TO}}$  deviate, meaning that it is not necessary to exactly measure the full shape of each branch of each tetrapod. Thirdly, from a practical point of view, a 2<sup>nd</sup> order polynomial is the easiest function to handle for the used software, as singularities are totally avoided, which might not be the case for a logarithmic function. In more detail, the polynomial function is given by Equation 14, at which the slope of the curvature around the onset of the branch is determined by the take-off angle, while the second parameter is further determined by the height and the effective angle. For investigations, each branch was divided in ten cylinders, whose displacement of the top relative to its respective bottom were determined by this function.

$$y(x) = ax + bx^2 \quad \text{with } b = \frac{1}{H} \left( \frac{1}{\tan(\alpha_{\text{eff}})} - a \right), \quad a = \tan(90^\circ - \alpha_{\text{TO}}) \quad \text{Equation 14}$$

The implication of this particular curvature on the final stiffness is depicted exemplary ( $H=3 \mu\text{m}$ ,  $\alpha_{\text{eff}}=60^\circ$ ) in Figure 58. One can see clearly within the first  $10^\circ$  of deviation between  $\alpha_{\text{eff}}$  and  $\alpha_{\text{TO}}$  the stiffness decreases drastically by an order of magnitude and seems to settle afterward to a saturation value. This remarkable result points out that in the end the stiffness of a tetrapod is determined most likely more by the curvature than its other geometrical parameters, such as the height and it explains as well the observed difference in stiffness between measurements and initial simulations. Moreover, this result in itself points out the demand on the fabrication process of nanostructures, as it becomes of essential importance to avoid curved branches! However, the simply put demand of straight branches, in turn, will require thorough research and more sophisticated studies, hence were not undertaken in the frame of this thesis.

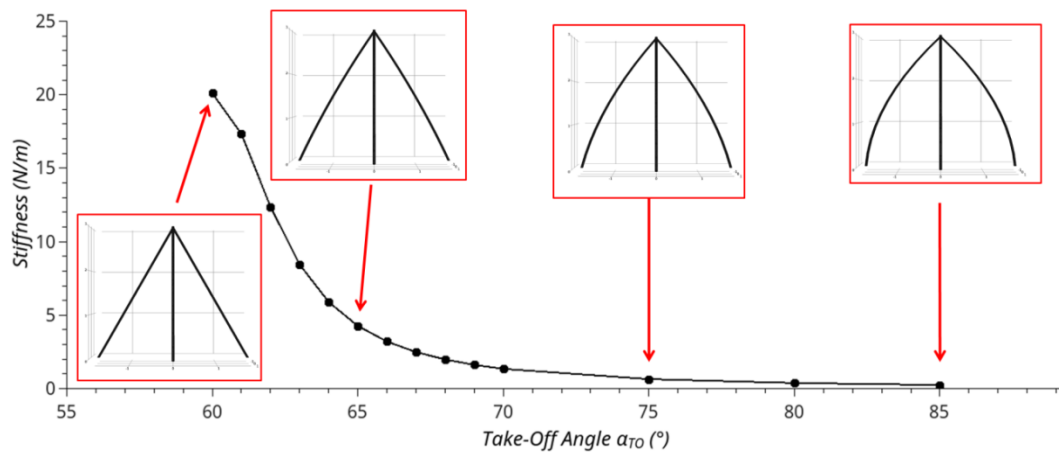


**Figure 58:** with increasing curvature of a tetrapod ( $H=3 \mu\text{m}$ ,  $\alpha_{\text{eff}}=60^\circ$ ,  $D=50 \text{ nm}$ ), determined by the parameter  $\alpha_{TO}$ , the stiffness decreases strongly. In fact, the highest decrease, **an order of magnitude**, is observed within the first  $10^\circ$  of deviation of intended from real structure.

The fact that the curvature of the branches has such an impact on the results is even more underlined by a simulated Force-Displacement curve (black line), shown in Figure 59, for a tetrapod with a height of  $2 \mu\text{m}$ ,  $\alpha_{\text{eff}}=60^\circ$  and  $\alpha_{TO}=75^\circ$ , and diameter of  $50 \text{ nm}$ . In addition in the same figure, the adjusted curve of a tetrapod with the same geometrical parameters is shown as red curve, at which only the first retract is shown and the onset point was adjusted to be at the same position as the simulated curve. Both curves show the same qualitative behavior, i.e. linear at the onset point and then a saturation towards stronger displacements. Moreover the actual values, of about  $85 \text{ nN}$  and about  $53 \text{ nN}$ , for measured and simulated, respectively are very close to each other, which again points out the relevance of this finding.

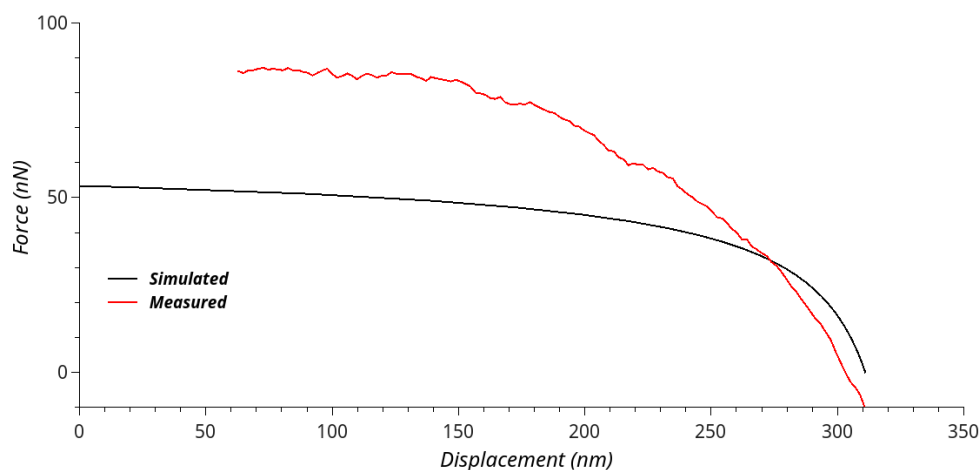


**Figure 59:** including a certain curvature ( $H=2 \mu\text{m}$ ,  $\alpha_{\text{eff}}=60^\circ$ ,  $\alpha_{\text{eff}}=75^\circ$ ,  $D=50 \text{ nm}$ ) the simulated force curve (black) shows the same behavior as observed in the measurements (red), i.e. about linear for small displacements and a saturation towards larger displacements. The displacement of the measured curve was adapted to have the same onset point, yet the force values were not further modified in order to be compared to the simulation.

Motivated by the obtained results a full comparison between measurements and simulations was done, which would include the exact height, as well the take-off angle and the effective angle of each structure, as measured by the SEM. A comparison of measured stiffness (a) to simulated (b) can be seen in Figure 60. This time not only some qualitative trends of the curves can be seen in both, but as well distinctive features of the curves are the same, e.g. the maximum line which stretches into the surface from the left at an angle of  $65^\circ$ . Moreover, also the absolute quantitative values are almost the same, yet not fully equivalent, although the difference is typically within the range of about 50 %. This general comparison again shows that the biggest influence on the stiffness stems from the curvature of the branches.

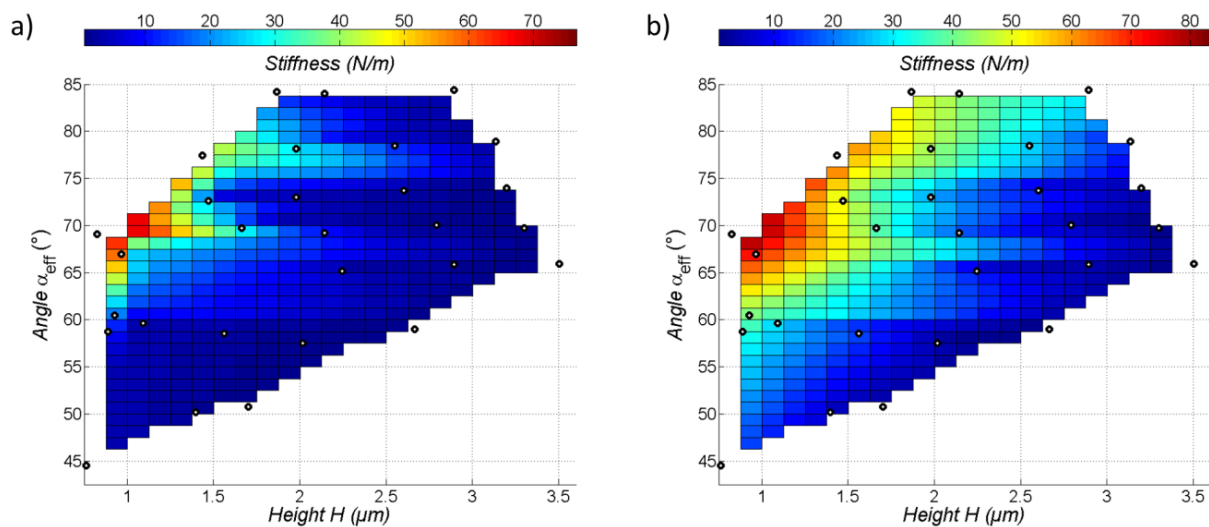


**Figure 60:** a comparison of measured (a) and simulated (b) stiffness, including the respective geometrical parameters of the tetrapods, i.e. the height,  $\alpha_{eff}$  and  $\alpha_{TO}$  in both cases the simulated geometries are indicated by black-white spots and the stiffness map was obtained by interpolation in between these points.

## 5.8 Imaging Capability of Nano-Probes

The experiments and measurements in this section were carried out by Jürgen Sattelkow, whose support is gratefully acknowledged at this point. After thoroughly determining the geometrical parameters for suitable tetrapods a short investigation on the imaging capabilities was done. In a similar manner as described in section 5.3, a cantilever was prepared in order to allow deposition of a tetrapod on its tip, as shown in Figure 61 (a). After modification, a tetrapod (b), was deposited (intended  $H=1 \mu\text{m}$  and  $\alpha=70^\circ$ ) on the tip with a 5 kV / 25 pA electron beam. Despite the fact that for the investigations before a 30 kV beam was used, the deposition parameters had to be adjusted, as it is yet not feasible to reliably deposit a structure on a cantilever with 30 kV, due to a terrible signal to noise ratio as similar amounts of SE are emitted on the top and backside of the cantilever, thus almost no image contrast can be achieved and an exact focusing of the electron beam becomes

nearly impossible. After deposition, the respective cantilever chip was mounted on the AFSEM and the principal imaging capability was proofed by rastering a standard test sample (c).

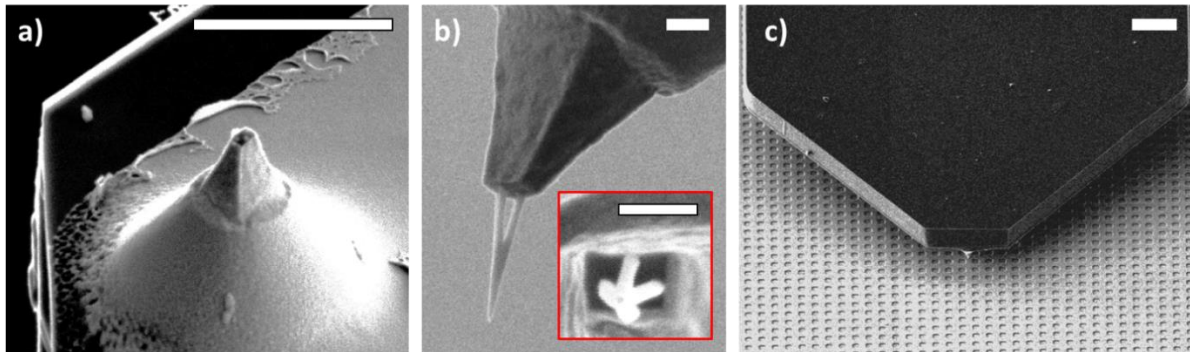


**Figure 61:** (a) a similar modification of the cantilever was done as before in order to deposit a tetrapod (b) on its tip. (c) mounting the cantilever on the AFSEM in order to test the imaging capability of the tetrapod on a standard sample. The scale bars represent  $5\ \mu\text{m}$  (a),  $1\ \mu\text{m}$  (b), and  $10\ \mu\text{m}$  (c).

In detail, a surface with rectangular shaped holes was scanned in a certain area, indicated by a blue dashed rectangle, shown in Figure 62 (a). It was possible to obtain morphological information even at *ultra-high* scan speeds as fast as  $200\ \mu\text{m/s}$ , depicted in (b) by a 3D AFM image. Furthermore one can see in (c) scans taken with a speed of  $20\ \mu\text{m/s}$ . Although a certain difference in forward and backward direction can be seen, the quantitative information is very accurate as the standard sample has hole depths with a nominal height of  $180\ \text{nm}$ . The lateral difference in forward and backward direction can be regarded to a radial plastic deformation, as observed before for steep tetrapods (section 5.4). Due to this deformation, the apex of the tetrapod is dragged differently in different directions, thus forward and backward are not exactly overlapping, which in principle points out the importance that a certain minimum radial stiffness is to avoid this problem and obtain reliable measurements. Overall already with this first trial, it is shown that in principal the imaging capability of the here investigated structures is given. As well they should be suited even for *ultra-fast* scan speeds, making even the imaging of certain biological processes possible, as those happen typically within shorter time frames.

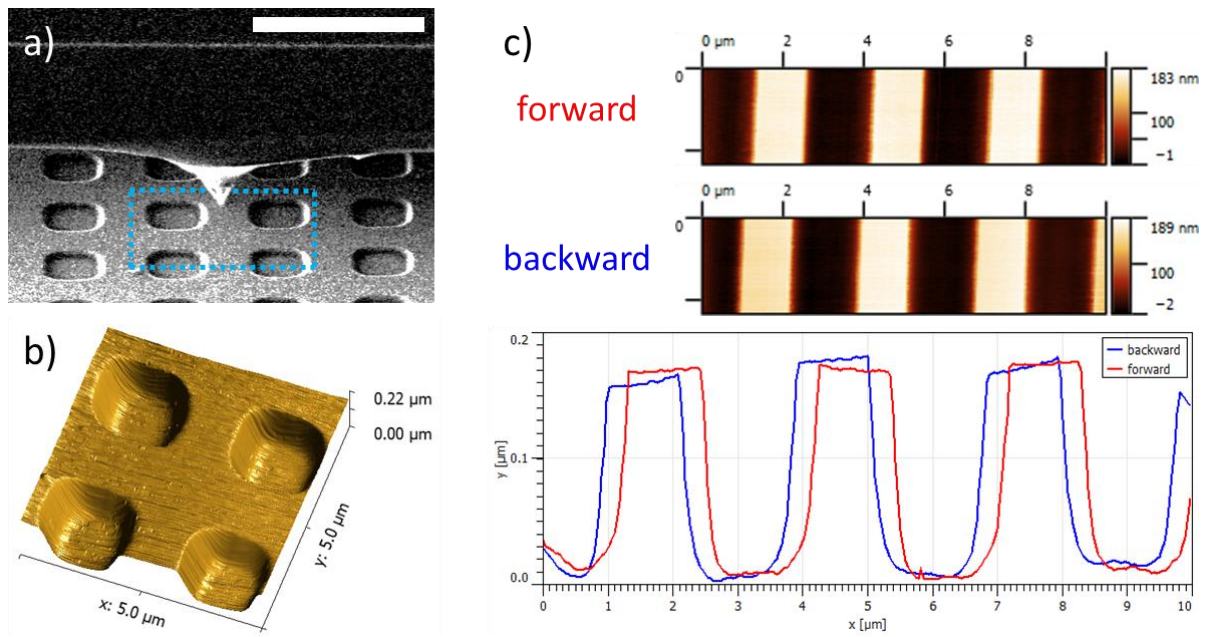


**Figure 62:** (a) a SEM micrograph of the standard test sample, showing rectangular holes with a nominal depth of 180 nm. The scale bar corresponds to 5 μm. (b) a 3D image of the blue dashed scan area in (a) at an ultra-fast scan speed of 200 μm/s showing the principal applicability for such high scan speeds. (c) quantitatively at a scan speed of 20 μm/s a mismatch of forward and backward can be observed.

## 6 Heat Transfer Simulation

Besides the mechanical aspect, we also took a glimpse on the heat transport characteristics. As before we will consider the analytical solution for the simplest case (i.e. a single line), then compare it to a simulation of a bipod. In particular, we focus here on the time until the system reaches a steady state, which is denoted as  $t_{\text{sts}}$  and defined as the time when  $\Delta T/\Delta t < 1 \cdot 10^{-6} \text{ }^\circ\text{C}$ . This is of fundamental interest since this characteristic time will limit the possible scanning speed in the end.

Due to practical reasons the conducted calculations and simulations do not include effects on the nanoscale (inner structure, mean free carrier path), as such simulations become highly complex. Therefore we assume that the actual behavior of structures will differ from these results. However, they still represent a first simple approximation to the problem. Considering only heat conduction, as the predominant conduction mechanism in the considered temperature range and in vacuum, two parameters are of interest, i.e. the specific heat capacity at constant pressure  $c_p$  and the heat conductivity  $k$ . According to literature these parameters for amorphous carbon range from  $c_p=100 \text{ J}/(\text{kg K}) - 1000 \text{ J}/(\text{kg K})$  and  $k=0.2 \text{ W}/(\text{m K}) - 10 \text{ W}/(\text{m K})^{74,75}$ . For bulk Platinum the values are  $c_p= 134 \text{ J}/(\text{kg K})$  and  $k=69.1 \text{ W}/(\text{m K})^{76}$ . Investigations focused on the extreme cases of these values, which are once a high heat capacity and low conductivity (aC) and secondly a low heat capacity and high conductivity (Pt). These two cases are considered since they represent the longest and shortest time until a steady state is attained for a structure connected to different temperatures at its respective ends.

### 6.1 Analytical Solution

The evolution of temperature  $T$  at any point  $x$  at any time  $t$  of a single line (length  $L$ ) connected to different temperatures  $T_1$  and  $T_2$  at its respective ends is given by Equation 15 and has the general solution of Equation 16, at which the coefficients  $B_n$  in the sum are given by Equation 17 with the initial temperature distribution  $f(x)$  and the equilibrium Temperature distribution ( $t \rightarrow \infty$ )  $T_e(x)$ , given in Equation 18. This equation was computed in Matlab for a single line with a length of  $2 \text{ } \mu\text{m}$ , considering summands up to  $n=200$ . The results for Pt and aC are depicted in Figure 63 (a) and (b), respectively, as plots of the temperature  $T$  (colour bar) against the spatial coordinate  $x$  (abscissa) and the time  $t$  (ordinate), at which the initial and boundary conditions were set to  $f(x)=300 \text{ K}$ ,  $T_1=300 \text{ K}$  and  $T_2=400 \text{ K}$ . In the two plots the time to equilibrium  $t_{\text{sts}}$  is visualized as a black dashed line, with a value of  $0.03 \text{ } \mu\text{s}$  and  $60 \text{ } \mu\text{s}$ , for Pt and aC, respectively.

$$\frac{\partial T}{\partial t} = \frac{k}{\rho c_p} \frac{\partial^2 T}{\partial x^2} \quad \text{Equation 15}$$

$$T(x, t) = T_1 + \frac{T_2 - T_1}{L} x + \sum_{n=1}^{\infty} B_n \sin\left(\frac{n\pi x}{L}\right) e^{-k\left(\frac{n\pi}{L}\right)^2 t} \quad \text{Equation 16}$$

$$B_n = \frac{2}{L} \int_0^L (f(x) - T_E(x)) \sin\left(\frac{n\pi x}{L}\right) dx \quad \text{Equation 17}$$

$$f(x) = T(x, 0) \quad \text{and} \quad T_E(x) = T_1 + \frac{T_2 - T_1}{L} x \quad \text{Equation 18}$$

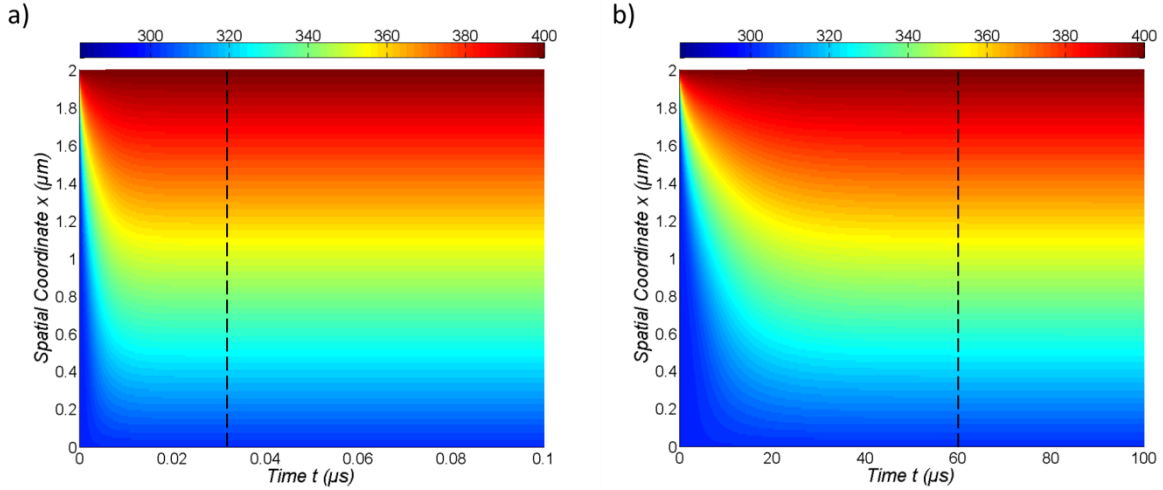


**Figure 63:** computation of the time and space dependent temperature evolution of a single line (2  $\mu\text{m}$ ) with characteristic thermal properties of Pt (a) and aC (b), shows that the time to equilibrium (black dashed line) is well below 70  $\mu\text{s}$ .

## 6.2 Simulations

Thermal simulations were conducted using the *Heat Transfer Branch* of COMSOL. In particular, an ideal bipod with a height of 3  $\mu\text{m}$ , a diameter of 50 nm and opening angle of 60° was assumed, as shown in Figure 64 (a). The top surface of the bipod is connected to a heat source with a constant temperature of 400 K, the bottom of the pillar is connected to a heat sink (Gold, 1  $\mu\text{m}$  x 1  $\mu\text{m}$  x 100 nm) with a constant temperature of 300 K at its surface. At  $t=0$  the temperature in the entire structure is set to 300 K. The results for Pt and aC, with the abovementioned properties are shown in a single plot, Figure 64 (b), for a point with the longest time until equilibrium is reached, indicated by a cross in the inlet in (b). One can see that for the considered thermal properties and geometry a time to steady state  $t_{\text{sts}}$  between 0.01  $\mu\text{s}$  and about 60  $\mu\text{s}$  is obtained, which is in accordance with the calculations undertaken before. Moreover, comparing the results to scanning speeds of AFMs it becomes evident that even for the extreme case of heating from 300 K to 400 K and worst material properties a scan frequency of 27 Hz (512 pixel) would easily be feasible, as this

scan frequency would correspond to a pixel to pixel time interval of about  $70 \mu\text{s}$ ! Therefore the theoretical limit for a practical application as thermal nanoprobe is more than surpassed!

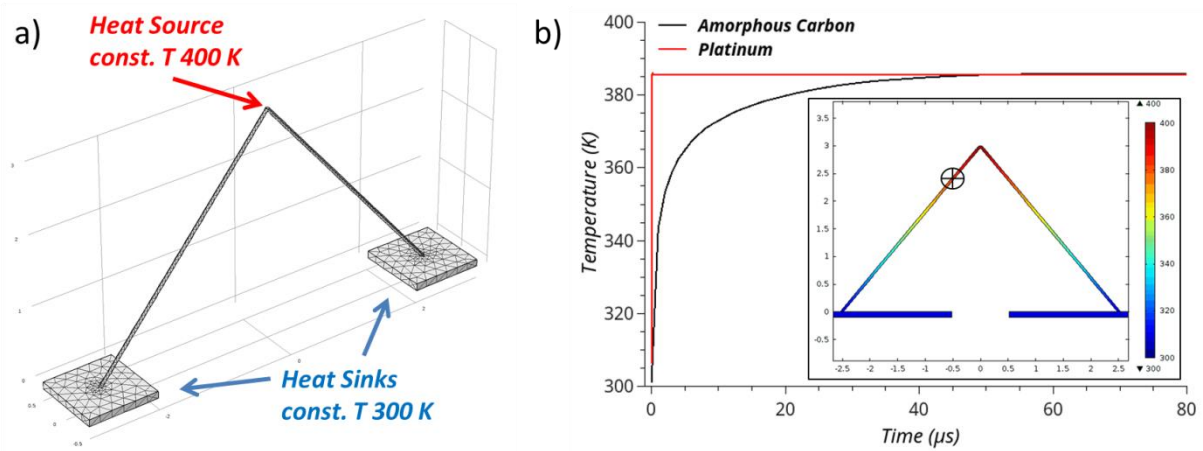


**Figure 64:** (a) the model of a bipod ( $H=3 \mu\text{m}$ ,  $\alpha=60^\circ$ ,  $D=50 \text{ nm}$ ) connected to a heat source at its top of 400 K and Au heat sinks at its bottom with a constant temperature of 300 K, at  $t=0$  the temperature in the whole structure is set to 300 K. (b) the simulated temperature evolution for a single point, indicated by a cross in the inlet, with characteristic properties of Platinum (red) and amorphous Carbon (black) clearly, underlines the theoretical results that the time to equilibrium is well below  $70 \mu\text{s}$ .

## 7 Observations on Shape Change Effects

After deposition of tetrapods, it was observed that in some cases for small opening angles  $\alpha$  and large heights  $H$  the branches do not fully merge together at the apex, although at least two branches respectively fused together, as shown in Figure 65. Hence these structures are similar to two slanted bipods which are in close vicinity at their apex resembling the structure of a tetrapod. For some experiments a full characterization regarding their geometrical parameters was not done immediately after deposition but a certain time after deposition, for which the sample was taken out of the vacuum chamber and kept in a storage box for several days on air. However, during this time the structures bent in a particular way, as shown in Figure 66. The bipods bent upwards as can be seen from a top view (a) and front view (b). Moreover, the bipods bent back to their original as-deposited geometry after longer  $e^-$  beam irradiation of the tetrapod as can be seen in (c). One should notice that due to frequent imaging the gap between bipods became smaller and therefore images (a) – (c) are shown in chronological order.

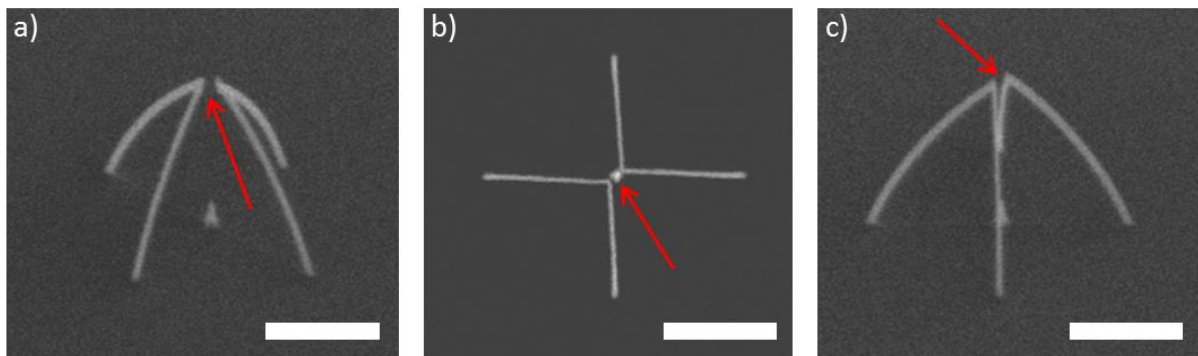


**Figure 65:** imaging of a tetrapod directly after deposition shows that the branches did not merge at its apex, as seen from the side (a), the top (b) and the front (c). The emerging gap at the top of this structure is indicated in each case by a red arrow. Scale bars in each picture correspond to  $1\ \mu\text{m}$ .

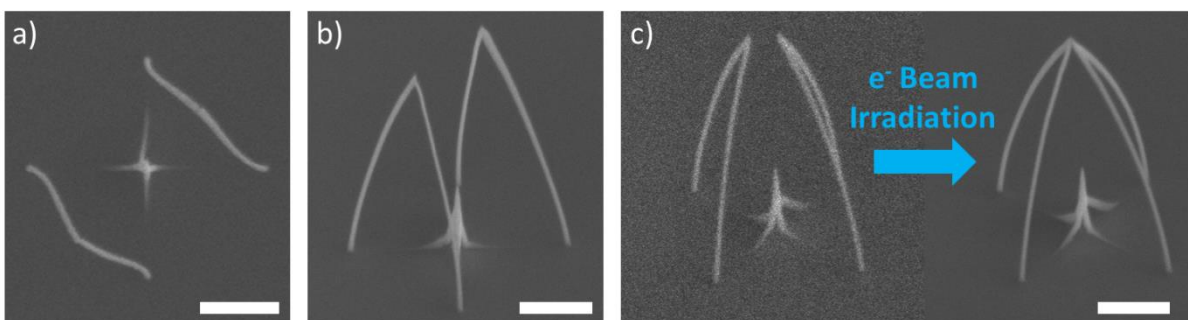


**Figure 66:** an up-bent tetrapod structure in a top view (a), front view (b) and side view (c), also showing a back-bending of the branches after  $e^-$ -beam irradiation. One should consider that due to frequent imaging the gap between bipods became smaller. The images are shown in chronological order. Scale bars in each picture correspond to  $1\ \mu\text{m}$ .

Furthermore, it was observed that a direct irradiation of the tetrapods was not necessary for back-bending to occur, exemplarily shown in Figure 67. In (a) an up-bent tetrapod is shown before electron beam irradiation of the surface with a decreased scan area. In (b) a micrograph of the merged tetrapod is shown, at which the irradiated area becomes evident due to some beam induced contamination, indicated by a blue frame.

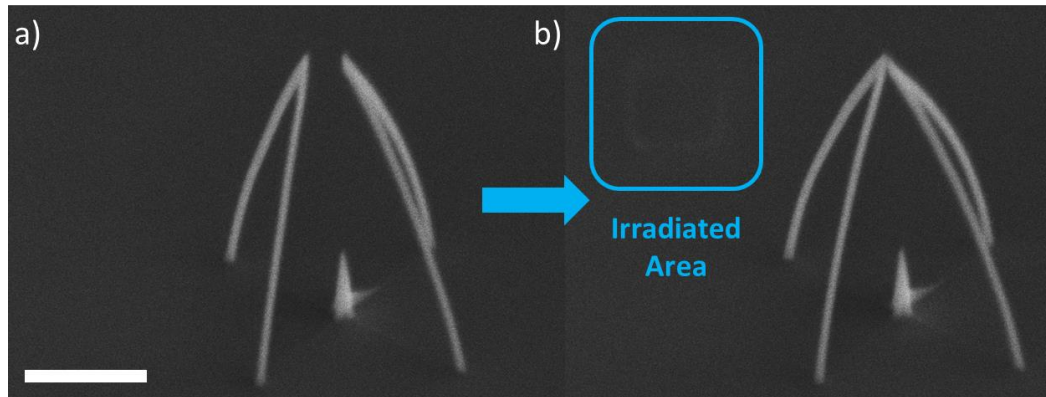


**Figure 67:** (a) an up-bent tetrapod, which bent back (b) to its as-deposited geometry after electron beam irradiation of a small window, evident by faint white blurred lines, indicated by a blue frame. The scale bar at the bottom left corner corresponds to  $1\ \mu\text{m}$ .

In order to understand this effect better, a short investigation was done on lone standing slanted bipods, arranged on 4 corners of a square pointing inwards and outwards, as shown in Figure 68 (a) and (d), respectively. This geometry and arrangement were chosen in order to rule out some kind of mutual attraction between bipods and any possible influence from the scanning direction of the electron beam. Again it was observed that after 1 night out of vacuum, the structures bent upwards, all in the same manner (b) and (d). During irradiation with the electron beam the structures showed the above-described effect of back-bending towards their original shape and above that, the bipods even bent beyond their as-deposited geometry, indicated by a red dotted line in (c) and (f).

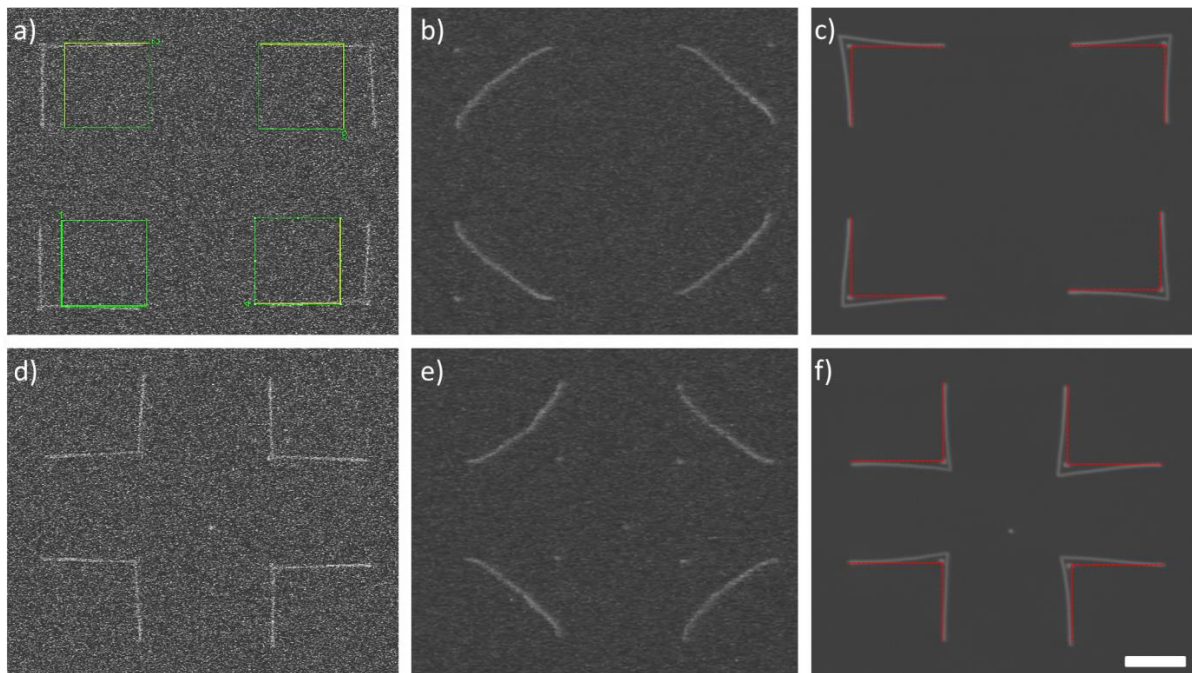


**Figure 68:** slanted bipods deposited on a square pointing outwards and inwards as-deposited, (a) and (d), respectively. (b), (e) after 1 day out of the vacuum chamber the bipods exhibited again up-bending. (c) and (f) after electron beam irradiation of the structures back bending was observed and the geometries even bent further than their initial as-deposited shape, indicated by a red dashed line. The scale bar in (f) corresponds to 1  $\mu\text{m}$  and accounts for all pictures.

At the moment the underlying mechanism behind the up-bending and back-bending effect are not entirely known and due to their complexity require a sophisticated study, which would go beyond the scope of this thesis. However, from the above-seen behavior and general assumptions, we suppose that the following aspects come into play and should be considered.

**The Up-Bending Effect** is assumed to be caused and / or influenced by the following aspects, which should be considered: **1)** a processing induced chemical inhomogeneity, **2)** a change of the structure after deposition.

**1)** a chemical inhomogeneity in the structures, which arises as a result of the electron beam interaction with a free standing structure, as shown in Figure 69 (a). In detail, the incoming PEs will have an inelastic interaction with the bulk atoms, thus sending out SE1, which are assumed to have no preferential direction. Yet the inelastic scattering process leads only to a small change of direction of the PE, hence these are most probably scattered in the forward direction. While SE1 are mostly responsible for the deposition, FSE and PE trigger further dissociation on uncompleted precursor molecules on their way through the deposit. This leads to a different degree of dissociation as a function of the Z coordinate as shown in (b).

**2)** it was observed before that FEBID structures change their volume after being exposed to air, known as swelling<sup>77</sup>. However, at the moment this effect is as well not studied in its details and a topic of ongoing investigations. Yet, assuming a chemical inhomogeneity in the structure (**1**), different amounts of swelling might occur (**2**), which cause one part to expand more than the other, leading to an up-bending of the structure, as shown in (c).

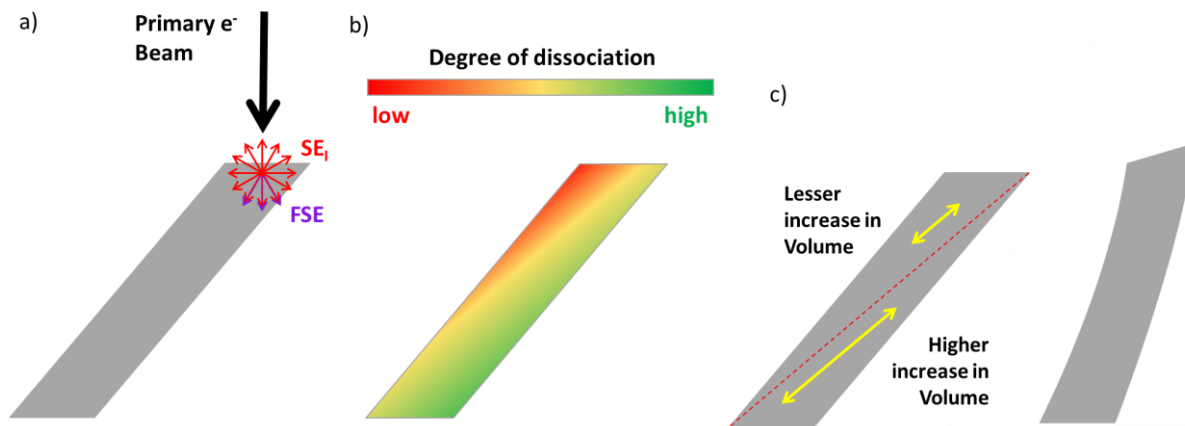


**Figure 69:** (a) due to additional dissociating forward scattered electrons (FSE) lower parts of the bipod might have a higher degree of dissociation (b). Assuming some chemical inhomogeneity during swelling of the structure (c), different parts of the structure might experience different swelling, leading to a different increase in volume for upper and lower levels, resulting in a net shape change of the branch.

**The Back-Bending Effect** is assumed to arise due to or might be influenced by the following effects:  
**1)** an electric field induced by the dot below the branches, **2)** removal of absorbed species, **3)** different curing in the structures.

**1)** an electric field induced force pulling the branches back to their respective position and even further, might be caused by the co-deposited structures on the substrate below the final apex point as shown in Figure 70 (a). This would as well explain why structures can bend even further than their as-deposited geometry.

**2)** based on the assumption that a certain swelling occurs and furthermore suggesting that this effect is in principle the absorption of water into the structure, then, due to a chemical inhomogeneity different amounts in different areas, corresponding to the picture in Figure 69 (b) will be absorbed. Under  $e^-$  - beam irradiation the water molecules are broken up and can subsequently gas out of the deposit, leading to a decrease in volume depending on the amount of absorbed water, as schematically shown in Figure 70 (b).

**3)** based on the assumption of a chemical inhomogeneity, as shown in Figure 69 (b), the branch might be cured differently, which in turn leads to different volume reductions in different zones of the branch, inducing the back bending, in principal the reverse effect as shown in Figure 69 (c).

However, the role of the abovementioned assumptions are merely a good guess and no claim on their trueness can be done at this point, as they are rather far-fetched. Therefore more thoroughly studies considering this effect have to be undertaken, e.g. TEM-EELS characterization to investigate the hypothesized chemical inhomogeneity.

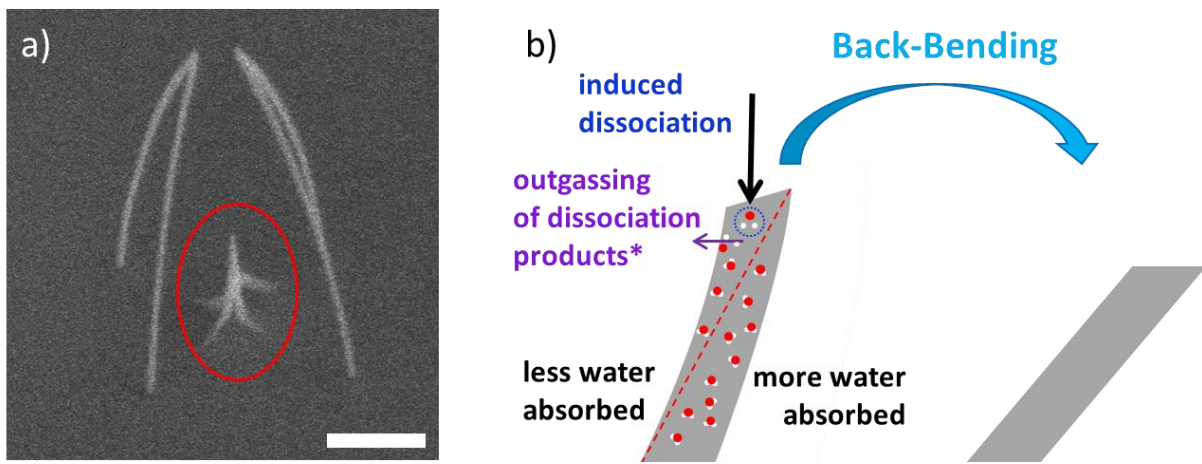


**Figure 70:** (a) the co-deposited structure (encircled red) below the branches could cause an electric field, which leads to a force acting on the branch tip causing the back-bending. The scale bar in the bottom right corner corresponds to 1  $\mu\text{m}$ . (b) assuming that water (Oxygen depicted red, Hydrogen depicted white) is absorbed in the structure (swelling), under  $e^-$  - beam irradiation the water molecules dissociate and subsequently gas out, leading to different volume losses in different areas, based on the assumption that beforehand different amounts of water were absorbed, due to a chemical inhomogeneity. \* Not only atomic oxygen and hydrogen will gas out, but several subsequent reaction products<sup>55</sup>.

## 8 Summary and Upcoming Challenges

The midterm motivation of this thesis was the application of free-standing 3D nanostructures as thermal probes fabricated via Focused Electron Beam Induced Deposition (FEBID) using the organometallic precursor  $\text{MeCpPt}^{\text{IV}}\text{Me}_3$ . The prerequisite on the nanostructures was that they would have to connect two electrodes, the stiffness in all directions should be at least as high as the cantilever itself, and the apex of the structure should be sharp enough to obtain a high lateral resolution during imaging. Following these boundary conditions, this thesis focused on the relationships between overall geometry and its mechanical properties by using a combination of experiments and simulations.

Considering the first demand, three suitable basic types of structures were identified, i.e. a bipod, a tripod and a tetrapod, (Figure 71 (d)), which are free-standing structures with 2, 3 and 4 branches, respectively, merging at the apex. However, the study started with finite elements simulations on single pillars (section 5.1.3), as the stiffness of these simple structures can be easily solved analytically. From this starting point, it was possible to show that the simulated values of axial and radial stiffness would deviate from the analytical solutions by less than 1 %. Simulations on the single pillars gave clear scaling laws and already in this early stage pointed out that the stiffness in the two main directions, i.e. axial and radial, would have a considerable difference. The next investigated architecture was a bipod structure (section 5.1.4), which was dismissed as it would have in the axial plane two different stiffness values, i.e. in the branch direction and perpendicular to this direction. In particular, the high difference in stiffness would be highly problematic as these values would differ by 2 to 3 orders of magnitude. Therefore, not only the scanning with such structures would be limited to the in-branch direction, also the deposition process of the bipod would have to be very accurate in order to deposit it with a certain position. The next investigated structure was a tripod. For this structure, two cases were in principal considered, i.e. either fully axially symmetric in structure but asymmetric with respect to the electrodes or axially asymmetric in their structure, but symmetric with respect to the electrodes. The first case would be favorable considering its mechanical properties, in particular, a fully symmetric stiffness in the radial direction, yet due to its asymmetry with respect to the electrodes was dismissed, as this would lead to a complicated current flow through the different branches. Although for the second case a more symmetric current flow can be expected, the mechanical properties are not as good, as a non-symmetric stiffness in the radial direction would be attained and moreover the fabrication process would be due to the structural inhomogeneity not as reliable as a fully axial symmetric structure. The next investigated basic architecture was the tetrapod (section 5.1.5). In general, this structure would exhibit intrinsically the best properties (Figure 71 (e) and (f)), as it could be deposited symmetrically with respect to the electrodes of the cantilever, thus the current flow through the branches can be assumed to be the same. Moreover, this structure would have high enough stiffness values in all directions (Figure 71 (a) and (b)). And even if a certain aspect ratio would be necessary in order to connect the electrodes, the overall behavior regarding the mechanical properties would be still the best (Figure 71 (c)). Therefore for the following studies, the focus was set on the tetrapod.

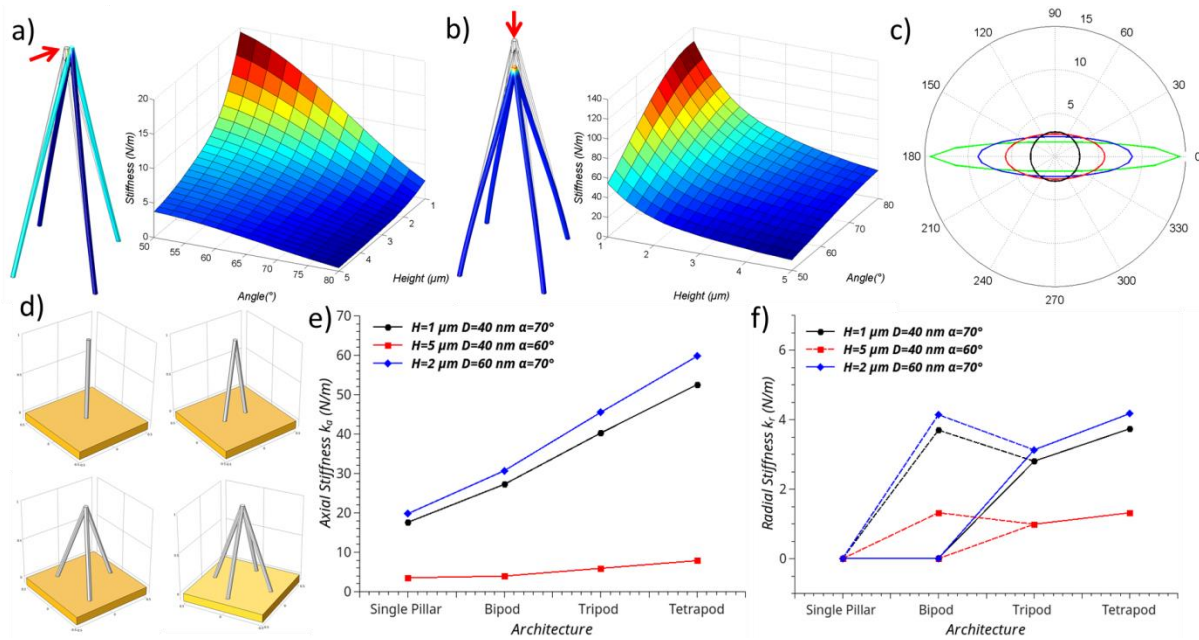


**Figure 71:** a summarizing figure of the findings of the first sections, showing a tetrapods deflection in radial direction (a), in axial direction (b) and their corresponding stiffness in dependence of its geometry. The axial stiffness can be tuned depending on the aspect ratio, depicted as a polar plot (c). Among the considered architectures (d), i.e. single pillar, bipod, tripod and tetrapod the tetrapod showed the overall best properties, as a comparison for stiffness in axial (e) and radial (f) direction shows.

Before testing the mechanical properties of tetrapods experimentally, two issues had to be confronted. First of all the cantilever had to be modified to be suitable for force spectroscopy (section 5.3). In particular the front of the cantilever was cut off via focused ion beam milling, thus allowing imaging of compression experiments. Then the apex of the tip was cut off in order to have a plateau which would be parallel to the structures base, thus compression occurs in a distinct and defined direction. Secondly, the proper design rules of the deposited structure for the used setup had to be found, at which it was shown that considering the position of the deposit relative to the gas injection nozzle an angle of  $45^\circ$  between gas flux vector and the branches of the structure would lead to the best results (section 5.2).

First force spectroscopy experiments considered the qualitative behavior of the branch movement of the tetrapod (section 5.4). In these experiments a certain twist of the branches was observed (Figure 72 (d)), which appeared clockwise and counterclockwise, as well symmetric and asymmetric. However, during simulations beforehand no twisting was observed (Figure 72 (a)). A closer look at the deposited tetrapods revealed that in the merging zone a mismatch in axial and radial direction was present (Figure 72 (c)). By introduction of this mismatch in the merging zone all kinds of twist could be mimicked in the simulation (Figure 72 (b)), hence this particular imperfection in the actual geometry of the tetrapods is regarded to be the cause of the branch twisting movement (section 5.5).

In the following quantitative measurements the basic scaling laws were observed as seen in the simulations, i.e. increased stiffness with larger angles and smaller heights of the structure. Yet certain

aspects of the simulated stiffness map and the experimentally determined were quite different, in particular the scaling with the angle was not as smooth as observed in the simulation and the quantitative values differed by a factor of 2 – 20 (section 5.6).

For this reason the model was refined (section 5.7) to include a certain design property of the deposited structures, i.e. their particular branch shape which has a noticeable curvature (Figure 72 (e)). Adaption of the curvature was done by a 2<sup>nd</sup> order polynomial, characterized by 2 parameters, i.e. the angle close to the substrate, the take-off angle and the average angle of the branch, the effective angle. By including both parameters it was shown that already with a small deviation from a straight branch the axial stiffness would decrease by an order of magnitude (Figure 72 (h)) and therefore this particular feature of the branches is regarded to the quantitative difference between simulation and experiment. Another evidence of importance of the curvature was seen in force-displacement simulations, as with the introduction of the branch curvature a non linear force-displacement was observed (Figure 72 (i)). Moreover by including the effective and take-off angle of all probed structures it was possible to achieve better accordance between measured and simulated stiffness map (Figure 72 (f) and (h)).

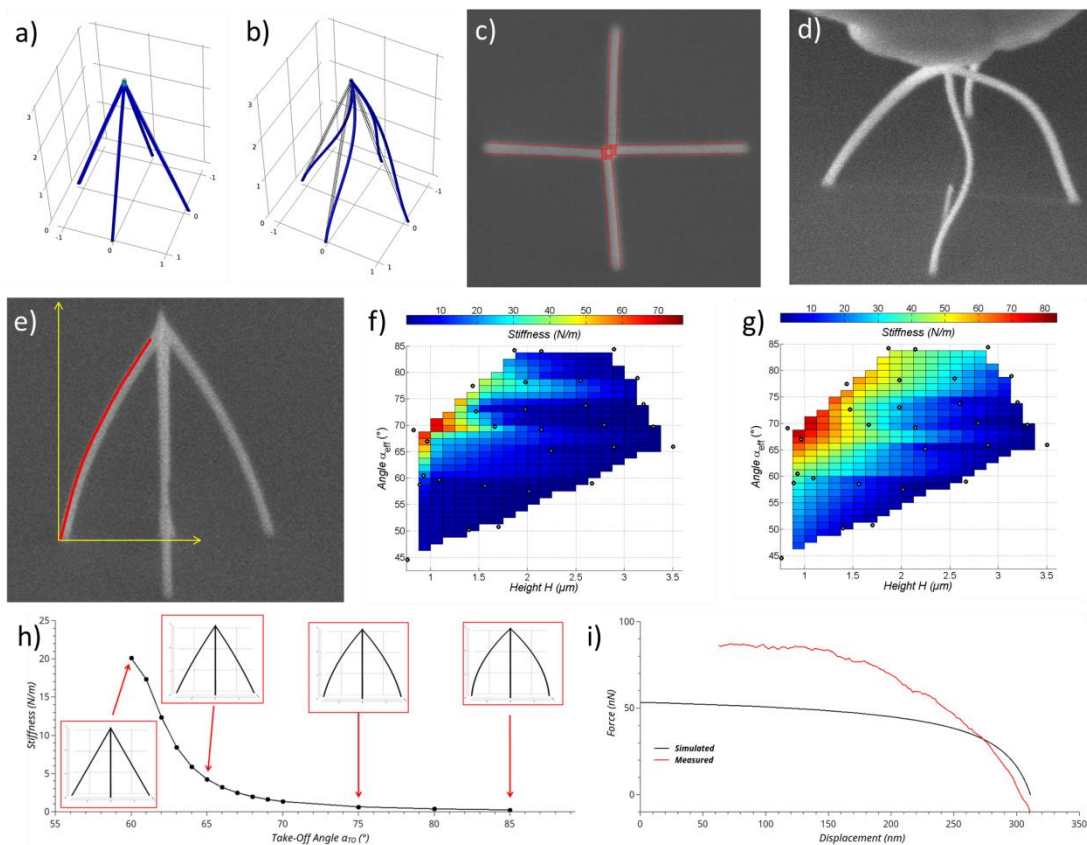


**Figure 72:** a summarizing figure of the findings. (a) the initial simulations did not match the observed behavior (d). Therefore, in the simulation a mismatch was introduced, as observed in reality (c), leading to the occurrence of a twisting motion in the simulation (b). Furthermore e, by the introduction of a certain curvature (e) into the model, it was possible to show that this feature heavily influenced the stiffness (h). Moreover, the simulated and measured force curves show qualitatively the same behavior (i). Thus, measurements (f) and simulations (g) are in good agreement.

The imaging capability (Figure 73 (b) and (c)) of the here considered structures (Figure 73 (a)) was principally shown in investigations (section 5.8) and moreover it was shown that the structures might as well be applicable for *ultra-fast* scan speeds up to 200  $\mu\text{m/s}$ . Thermal simulations and calculations (section 6) as well point out the principal feasibility to use these structures as thermal probes even for such high scan speeds as 27 Hz, as a thermal equilibrium will be attained within 70  $\mu\text{s}$ !

Moreover during deposition of tetrapods (Figure 73 (c)) an intriguing shape change effect was observed for slanted bipods (section 7). Although directly after deposition the geometry would be the same (Figure 73 (e)) as the intended geometry after taking the sample out of the vacuum and putting it back into the chamber we observed an up-bending of the structures (Figure 73 (f)). However, during imaging (irradiation with the electron beam) the structure would bend backwards to its initial geometry and then bend even further (Figure 73 (g)). However, the clear reason for this effect could not be shown. Therefore, to understand this effect and utilize it somehow will be an upcoming challenge in further research.

Overall in this thesis the applicability of tetrapods as thermal nanoprobes was shown based on the understanding and optimization of the design to achieve mechanical stable 3D nanoprobes. The upcoming challenges to be tackled are to bring a higher controllability in the fabrication process regarding the shape of the branches, thus it should become feasible to deposit straight branches and if possible to be able to vary the diameter of the individual branches. Although, theoretically already shown thermal scans were not undertaken yet and the actual thermal characteristics of the nanoprobes will as well be a challenge in future investigations.

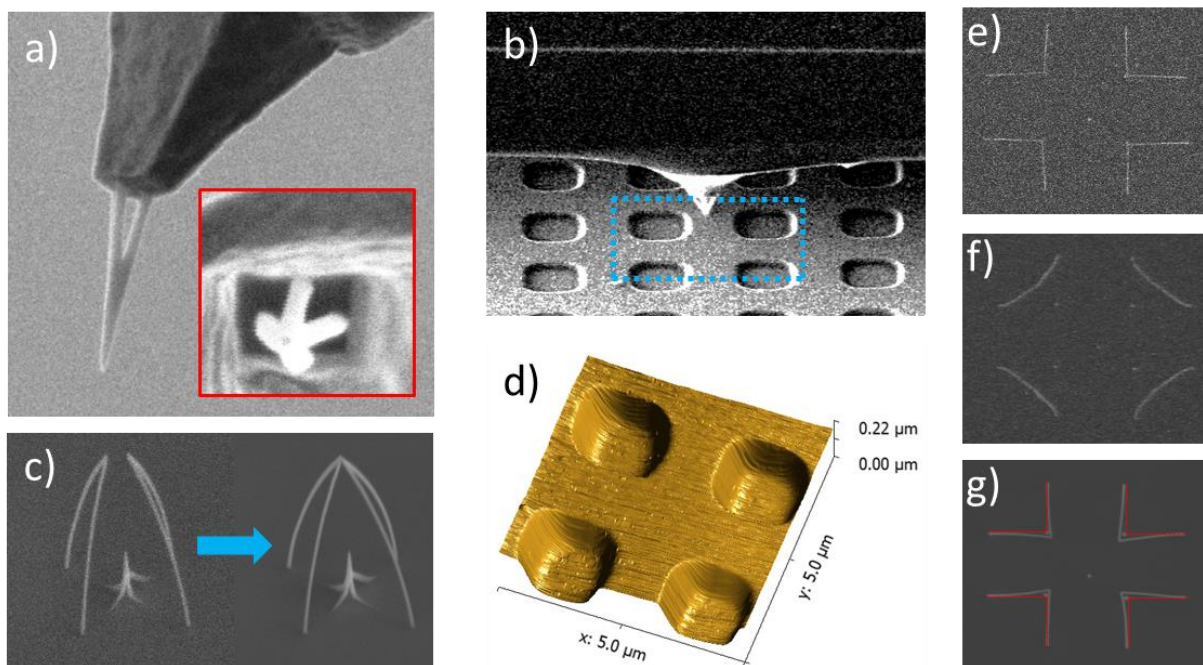


**Figure 73:** deposition of a tetrapod on a cantilever tip (a) and subsequent measurement (b) at very high scan speeds gave already quite good results (d). Furthermore a shape change effect was observed on slanted bipods (c). In particular, the as-deposited geometry will change after exposure to air (f) as the branches bend upwards. Then after electron irradiation the branches undergo back-bending to their initial geometry (g).

## References

---

1. Skoplaki, E., and J. A. Palyvos. "On the temperature dependence of photovoltaic module electrical performance: A review of efficiency/power correlations." *Solar energy* 83.5 (2009): 614-624.
2. Zalba, Belen, et al. "Review on thermal energy storage with phase change: materials, heat transfer analysis and applications." *Applied thermal engineering* 23.3 (2003): 251-283.
3. SCL-Sensor.Tech. Fabrication GmbH, Seestadterstraße 27, 1220 Vienna, Austria
4. GETec Microscopy GmbH, Seestadterstraße 27, 1220 Vienna, Austria
5. Rangelow, I. W., et al. "Thermal nano-probe." *Microelectronic engineering* 57 (2001): 737-748.
6. Binnig, Gerd, et al. "Surface studies by scanning tunneling microscopy." *Physical review letters* 49.1 (1982): 57
7. Binnig, Gerd, Calvin F. Quate, and Ch Gerber. "Atomic force microscope." *Physical review letters* 56.9 (1986): 930.
8. Williamson, J. B. P. "Paper 17: microtopography of surfaces." *Proceedings of the Institution of Mechanical Engineers, Conference Proceedings*. Vol. 182. No. 11. SAGE Publications, 1967.
9. Bhushan, Bharat, and Othmar Marti. *Springer handbook of nanotechnology*. Springer Berlin Heidelberg, 2010. 573-617.
10. Plank H. *Courtesy*
11. Plank, H. Elektrische Modifikation von Self-Sensing Cantileverspitzen mittels FEBID 3D Nanoprinting Zentrum für Elektronenmikroskopie Graz. *Final Rep. Inov. cheque* (2015).
12. jibeard (2006), *Wheatstone bridge*, Wikimedia commons
13. Fantner, Georg E., et al. "DMCMN: In depth characterization and control of AFM cantilevers with integrated sensing and actuation." *Journal of dynamic systems, measurement, and control* 131.6 (2009): 061104.
14. Jones, John Edward. "On the determination of molecular fields. II. From the equation of state of a gas." *Proceedings of the Royal Society of London A: Mathematical, Physical and Engineering Sciences*. Vol. 106. No. 738. The Royal Society, 1924.
15. Majumdar, A., J. P. Carrejo, and J. Lai. "Thermal imaging using the atomic force microscope." *Applied Physics Letters* 62.20 (1993): 2501-2503.
16. Pylkki, Russell J., Patrick J. Moyer, and Paul E. West. "Scanning near-field optical microscopy and scanning thermal microscopy." *Japanese journal of applied physics* 33.6S (1994): 3785.
17. Nakabeppu, O. S. A. M. U., et al. "Scanning thermal imaging microscopy using composite cantilever probes." *Applied physics letters* 66.6 (1995): 694-696.
18. Williams, Clayton C., and H. K. Wickramasinghe. "Scanning thermal profiler." *Applied Physics Letters* 49.23 (1986): 1587-1589.
19. Gomès, Séverine, Ali Assy, and Pierre-Olivier Chapuis. "Scanning thermal microscopy: a review." *physica status solidi (a)* 212.3 (2015): 477-494.
20. Yoann, Joliff. "Finite element analysis of the material's area affected during a micro thermal analysis applied to homogeneous materials." *Journal of Surface Engineered Materials and Advanced Technology* 2011 (2011).
21. Wielgoszewski, Grzegorz, et al. "Standard-based direct calibration method for scanning thermal microscopy nanoprobes." *Sensors and Actuators A: Physical* 214 (2014): 1-6.
22. Butt, Hans-Jürgen, Brunero Cappella, and Michael Kappl. "Force measurements with the atomic force microscope: Technique, interpretation and applications." *Surface science reports* 59.1 (2005): 1-152.
23. Arnold G. Master's Thesis, *Quasi -1D Nano-Resonators for Ultra-Sensitive Gas Sensing Applications*, 2015
24. Schwalb M. Private correspondence, 2016
25. Winkler R. *Courtesy*
26. Utke, Ivo, Patrik Hoffmann, and John Melngailis. "Gas-assisted focused electron beam and ion beam processing and fabrication." *Journal of Vacuum Science & Technology B* 26.4 (2008): 1197-1276.
27. Giannuzzi, L. A., and F. A. Stevie. "A review of focused ion beam milling techniques for TEM specimen preparation." *Micron* 30.3 (1999): 197-204.
28. Toth, Milos. "Advances in gas-mediated electron beam-induced etching and related material processing techniques." *Applied Physics A* 117.4 (2014): 1623-1629.

29. Huth, Michael, et al. "Focused electron beam induced deposition: A perspective." *Beilstein journal of nanotechnology* 3.1 (2012): 597-619.
30. Fröch J. Master's Thesis, Focused Ion Beam assisted Deposition of Metals: Process-Parameters and Functionality Relationships, 2016
31. Swanson, Lyn W., and Gregory A. Schwind. "Handbook of Charged Particle Optics." *edited by J. Orloff*, (CRC, New York, 1997), Chap2 (1997).
32. FEI Company, Achtseweg Noord 5, Bldg, 5651 GG Eindhoven, The Netherlands.
33. Schottky Field Emitter, viewed 18 Dec. 2016, <http://www.tnw.tudelft.nl/index.php?id=33723&>
34. Goldstein, Joseph, et al. *Scanning electron microscopy and X-ray microanalysis: a text for biologists, materials scientists, and geologists*. Springer Science & Business Media, 2012.
35. Drouin, Dominique, et al. "CASINO V2. 42-A fast and easy-to-use modeling tool for scanning electron microscopy and microanalysis users." *Scanning* 29.3 (2007): 92-101.
36. Reimer, Ludwig. "Scanning electron microscopy: physics of image formation and microanalysis." (2000): 1826.
37. Volkert, Cynthia A., and Andrew M. Minor. "Focused ion beam microscopy and micromachining." *MRS bulletin* 32.05 (2007): 389-399.
38. Emmanuel de Chambost (2007), *Détecteur Everhart-Thornley*, Wikimedia commons
39. Utke, I., et al. "High-resolution magnetic Co supertips grown by a focused electron beam." *Applied physics letters* 80.25 (2002): 4792-4794.
40. Matsui, Shinji, and Katsumi Mori. "New selective deposition technology by electron-beam induced surface reaction." *Journal of Vacuum Science & Technology B* 4.1 (1986): 299-304.
41. Perentes, Alexandre, and Patrik Hoffmann. "Focused Electron Beam Induced Deposition of Si-Based Materials From SiOxCy to Stoichiometric SiO2: Chemical Compositions, Chemical-Etch Rates, and Deep Ultraviolet Optical Transmissions." *Chemical Vapor Deposition* 13.4 (2007): 176-184.
42. Botman, Aurelien, et al. "Spontaneous Growth of Gallium-Filled Microcapillaries on Ion-Bombarded GaN." *Physical review letters* 111.13 (2013): 135503.
43. Randolph, Steven J., Aurelien Botman, and Milos Toth. "Deposition of Highly Porous Nanocrystalline Platinum on Functionalized Substrates Through Fluorine-Induced Decomposition of Pt (PF3) 4 Adsorbates." *Particle & Particle Systems Characterization* 30.8 (2013): 672-677.
44. Winkler, Robert, et al. "The nanoscale implications of a molecular gas beam during electron beam induced deposition." *ACS applied materials & interfaces* 6.4 (2014): 2987-2995.
45. Friedli, Vinzenz, et al. "Mass sensor for in situ monitoring of focused ion and electron beam induced processes." *Applied physics letters* 90.5 (2007): 053106.
46. Koops, H. W. P., et al. "High-resolution electron-beam induced deposition." *Journal of Vacuum Science & Technology B* 6.1 (1988): 477-481.
47. Toth, Milos, et al. "Continuum models of focused electron beam induced processing." *Beilstein journal of nanotechnology* 6.1 (2015): 1518-1540.
48. Allen, T. E., R. R. Kunz, and T. M. Mayer. "Monte Carlo calculation of low-energy electron emission from surfaces." *Journal of Vacuum Science & Technology B* 6.6 (1988): 2057-2060.
49. van Dorp, Willem F., et al. "The role of electron-stimulated desorption in focused electron beam induced deposition." *Beilstein journal of nanotechnology* 4.1 (2013): 474-480.
50. Bishop, James, et al. "Role of activated chemisorption in gas-mediated electron beam induced deposition." *Physical review letters* 109.14 (2012): 146103.
51. Van Dorp, W. F., et al. "Electron induced dissociation of trimethyl (methylcyclopentadienyl) platinum (IV): Total cross section as a function of incident electron energy." *Journal of Applied Physics* 106.7 (2009): 074903.
52. Wnuk, J. D., et al. "Electron beam deposition for nanofabrication: insights from surface science." *Surface Science* 605.3 (2011): 257-266.
53. Wnuk, Joshua D., et al. "Electron induced surface reactions of the organometallic precursor trimethyl (methylcyclopentadienyl) platinum (IV)." *The Journal of Physical Chemistry C* 113.6 (2009): 2487-2496.
54. Plank, Harald, et al. "Chemical tuning of PtC nanostructures fabricated via focused electron beam induced deposition." *Nanotechnology* 24.17 (2013): 175305.
55. Geier, Barbara, et al. "Rapid and highly compact purification for focused electron beam induced deposits: a low temperature approach using electron stimulated H2O reactions." *The Journal of Physical Chemistry C* 118.25 (2014): 14009-14016.

- 
56. Winkler, Robert, et al. "Toward ultraflat surface morphologies during focused electron beam induced nanosynthesis: disruption origins and compensation." *ACS applied materials & interfaces* 7.5 (2015): 3289-3297.
  57. Fowlkes, Jason D., et al. "Simulation Guided 3D Nanomanufacturing via Focused Electron Beam Induced Deposition." *ACS nano* (2016).
  58. Porrati, Fabrizio, et al. "Tuning the electrical conductivity of Pt-containing granular metals by postgrowth electron irradiation." *Journal of Applied Physics* 109.6 (2011): 063715.
  59. Plank Harald, et al. "Optimization of postgrowth electron-beam curing for focused electron-beam-induced Pt deposits." *Journal of Vacuum Science & Technology B* 29.5 (2011): 051801.
  60. Huth Michael, Florian Kolb, and Harald Plank. "Dielectric sensing by charging energy modulation in a nano-granular metal." *Applied Physics A* 117.4 (2014): 1689-1696.
  61. Sachser, Roland, et al. "Universal conductance correction in a tunable strongly coupled nanogranular metal." *Physical review letters* 107.20 (2011): 206803.
  62. Schwalb, Christian H., et al. "A tunable strain sensor using nanogranular metals." *Sensors* 10.11 (2010): 9847-9856.
  63. Hughes, Thomas JR. *The finite element method: linear static and dynamic finite element analysis*. Courier Corporation, 2012.
  64. Reddy, Junuthula Narasimha. *An introduction to the finite element method*. Vol. 2. No. 2.2. New York: McGraw-Hill, 1993.
  65. Multiphysics, C. O. M. S. O. L. "4.3 a, 2013." *COMSOL, Burlington, MA*.
  66. Multiphysics, C. O. M. S. O. L. "Comsol multiphysics user guide (version 4.3 a)." *COMSOL, AB* (2012): 39-40.
  67. Poisson's Ratio for Pt Annealed and Cold Worked, viewed on 16. Jan. 2017 <http://www.matweb.com/search/QuickText.aspx?SearchText=platinum>
  68. Poisson's Ratio for diamond Carbon, viewed on 16. Jan. 2017 <http://www.azom.com/properties.aspx?ArticleID=262>
  69. Cho, Sungwoo, et al. "Young's modulus, Poisson's ratio and failure properties of tetrahedral amorphous diamond-like carbon for MEMS devices." *Journal of Micromechanics and Microengineering* 15.4 (2005): 728.
  70. Pastorelli, R., et al. "Elastic constants of ultrathin diamond-like carbon films." *Diamond and Related Materials* 9.3 (2000): 825-830.
  71. Bret, Tristan, Ivo Utke, and Patrik Hoffmann. "Influence of the beam scan direction during focused electron beam induced deposition of 3D nanostructures." *Microelectronic engineering* 78 (2005): 307-313.
  72. Discussion with Harald Plank, Robert Winkler and Jürgen Sattelkow
  73. Kim, Min-Seok, et al. "Accurate determination of spring constant of atomic force microscope cantilevers and comparison with other methods." *Measurement* 43.4 (2010): 520-526.
  74. Silva, S. Ravi P., ed. *Properties of amorphous carbon*. No. 29. 1st, 2003.
  75. Balandin, Alexander A. "Thermal properties of graphene and nanostructured carbon materials." *Nature materials* 10.8 (2011): 569-581.
  76. Thermal properties for Pt Annealed and Cold Worked, viewed on 16. Jan. 2017 <http://www.matweb.com/search/QuickText.aspx?SearchText=platinum>
  77. Winkler, Robert, et al. "Novel Investigation Possibilities on FEBID Deposits by Combining Dual-Beam Capabilities", Poster presented at the 10<sup>th</sup> Workshop on Focused Electron Beam Induced Processing FEBIP – 2016, July 4<sup>th</sup>-8<sup>th</sup> 2016 in Vienna, Austria